

https://dspace.org/

Linear shape memory alloy (Nitinol) actuators in a 3D printed hand prosthesis

Parshotam, D S

2021
https://hdl.handle.net/10539/31874

Downloaded from a DSpace repository. https://dspace.org/

Linear Shape Memory Alloy (Nitinol) Actuators in a 3D Printed Hand Prosthesis

D.S. Parshotam

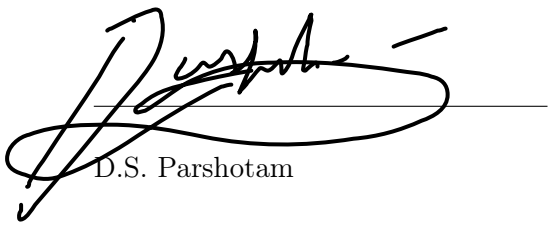
A dissertation submitted to the Faculty of Engineering and the Built Environment, University of the Witwatersrand, Johannesburg, in fulfilment of the requirements for the degree of Master of Science in Engineering.

Johannesburg, January 2021

Declaration

I declare that this dissertation is my own, unaided work, except where otherwise acknowledged. It is being submitted for the degree of Master of Science in Engineering in the University of the Witwatersrand, Johannesburg. It has not been submitted before for any degree or examination at any other university.

Signed this 26th day of January 2021



D.S. Parshotam

Executive Summary

There is a need for affordable prosthetic hands in developing countries. This is due to poor healthcare, substandard infrastructure, poor service delivery, and political instability. 3D printing has enabled NGOs and research institutions to rapidly design and manufacture low-cost prosthetic hands. In 2017, the University of the Witwatersrand (Wits) produced a tendon-driven prosthetic hand, powered by low-cost SG90 servomotors. The hand was deemed partially successful due to the low grip strength of 6 N achieved by the SG90 servomotor-actuation. In this research, linear shape memory alloy (nitinol) actuators were developed to actuate a 3D printed prosthetic hand; using a modified two-link transmission. The purpose of the two-link transmission was to replace the traditional tendon-driven designs, which lead to poor force transference between the actuators and fingers. An analytical model was developed to evaluate the positioning performance (response time and accuracy) of the nitinol-powered design. The analytical results were further supported with experimental data, which concluded that the design outperformed past nitinol-powered hands which utilized tendon-driven systems. A square step signal was used to evaluate the system's response time, while a ramp signal was used to test the path tracking performance. Input voltage and sampling frequency parameters were varied to determine the best combination for positioning performance. A 9 V input with a 500 Hz sampling frequency was concluded to be the best combination, which produced a step-up time constant (heating) of 0.06 s with a max finger speed of 152 $^\circ/s$, and a step-down time constant (cooling) of 0.11 s with a max finger speed of 123.6 $^\circ/s$. Average path tracking errors of 1.134° and 0.651° were obtained for the step and ramp signals, respectively. Another analytical model was developed to track the fingertip force with respect to the proximal interphalangeal joint (PIP) angle. It was found that as the PIP angle increased (finger curls inwards) the fingertip force was reduced. This trend was supported by experimental results. An HBM C9C load cell was used to measure the fingertip forces which ranged between 2.03-2.91 N for a 0° PIP angle, and 1.38-1.96 N for a 30° PIP angle, similar in range to past functional 3D printed hands. The developed nitinol-powered prosthesis generated an average power grip force of 16.6 N, 2.76 times larger than the past Wits SG90-powered hand. The measured tripod and pinch grip strengths were 7.3 N and 4.4 N, respectively. Silicon fingertip pads with an embedded force-sensing resistor were used to increase the contact area and absorb the initial impact with an object. This enabled the hand to manipulate objects as small as a 12 mm diameter marble. The nitinol-driven hand successfully performed the required power, hook, sphere, cylinder grips as well as a tripod grip and pinch. The nitinol actuators performed acceptably, and are deemed suitable to replace low-cost SG90 servomotors.

Contents

Declaration i

Executive Summary ii

Contents iii

List of Figures vi

List of Tables ix

1 Introduction and Literature Survey 1

1.1 Background and Motivation . . . 1

1.2 Literature Survey . . . 2

1.2.1 Anatomy of the Hand . . . 2

1.2.2 Commercially Available Robotic Prosthetic Hands . . . 4

1.2.2.1 Bebiobic Hand . . . 4

1.2.2.2 iLimb Hand . . . 5

1.2.2.3 EMG Pattern Recognition Sampling Frequency . . . 5

1.2.3 Past 3D Printed Robotic Prosthetic Hands . . . 6

1.2.3.1 Dextrus Hand . . . 6

1.2.3.2 Ada Hand . . . 7

1.2.3.3 Wits 3D Printable Hand Prosthesis . . . 8

1.2.3.4 Shortcomings Encountered in 3D Printed Robotic Prosthetic Hands . . . 8

1.2.4 Alternative Actuation Methods . . . 9

1.2.4.1 Pneumatic Actuation . . . 9

1.2.4.2 Shape Memory Alloy Actuation . . . 10

1.2.4.3 Electroactive Polymers Actuation . . . 10

1.2.4.4 Review of Alternative Actuation Methods . . . 10

1.2.5 Principles of Shape Memory Alloy Behaviour . . . 11

1.2.5.1 Stress-Strain-Temperature Relationship of Nitinol Wire . . . 11

1.2.5.2 Temperature Induced Transformation . . . 11

1.2.5.3 Uniaxial Loading . . . 13

1.2.6 Past Nitinol Powered Prosthetic Hands . . . 13

1.2.7 Actuator Response Time . . . 15

1.2.8 Past Shape Memory Alloy Actuators . . . 15

1.2.9 Literature Review Summary and Implications for this Research . . . 16

1.3 Research Questions . . . 17
1.4 Research Objectives . . . 17

2 Prosthetic Hand Design **18**
2.1 Nitinol Actuator Design . . . 18
2.2 Finger Mechanism Design . . . 21
2.3 Leaf Spring Bias . . . 22
2.4 Hand Design . . . 22

3 Analytical Analysis **25**
3.1 Steady-State Fingertip Force Analysis . . . 25
3.1.1 Torsional Bias . . . 25
3.1.2 Link 2 Orientation with Respect to the Finger Base Position . . . 26
3.1.3 Steady-State Fingertip Force Model . . . 28
3.1.4 Fingertip Force vs PIP Angle . . . 30
3.2 Bang-Bang Controlled Finger Trajectory Analysis . . . 31
3.2.1 Nitinol Wire Heat Transfer (Electro-Thermal) Model . . . 31
3.2.2 Finger Angle Displacement Based on Actuator Displacement Model . . . 34
3.2.3 Kinematic Finger Model . . . 36
3.2.4 Bang-Bang Controller Architecture for Nitinol-Driven Finger . . . 38
3.2.5 Step Response Analysis . . . 40

4 Prosthetic Hand Fabrication **45**
4.1 Additive Manufacturing . . . 45
4.2 Control Scheme . . . 47
4.2.1 Force Sensing Finger Pads . . . 47
4.2.2 Sensor Feedback Control Scheme . . . 47
4.3 Electronics . . . 49
4.3.1 Microcontroller . . . 49
4.3.2 Hardware Architecture . . . 50
4.4 Cost Estimation . . . 53

5 Finger Positioning **54**
5.1 Finger Positioning Test . . . 54
5.1.1 Apparatus . . . 54
5.2 Finger Positioning Results and Discussions . . . 56
5.2.1 Response Time Analysis . . . 56
5.2.2 Path Tracking Performance Analysis . . . 60

6 Finger Strength **64**
6.1 Fingertip Force Test . . . 65

6.1.1 Apparatus . . . 65
6.2 Finger Grip Force Test . . . 66
6.2.1 Apparatus . . . 66
6.3 Fingertip and Finger Grip Force Test Results and Discussion . . . 67

7 Mandatory Grips **70**
7.1 Grip Control Test . . . 70
7.2 Grip Control Results and Discussion . . . 71

8 Conclusions **74**

9 Future Work **76**
9.1 Control Recommendations . . . 76
9.2 Electronic Recommendations . . . 76
9.3 Design Recommendations . . . 76

References **78**

A Matlab Code **81**
A.1 Electro-Thermal-Mechanical Model for Step Input . . . 81

B Arduino Code **88**
B.1 Step Signal Code . . . 88
B.2 Ramp Signal Code . . . 91
B.3 Finger Strength Code . . . 95
B.4 Hand PWM Control Code . . . 96

C Detailed Analytical Derivations **98**
C.1 Kinematic Finger Model . . . 98
C.2 MPU6050 Sensor Uncertainty Analysis . . . 101

D Prosthetic Hand Circuit Connections **103**

List of Figures

1.1 Hand Gestures . . . 1
1.2 Hand Anatomy . . . 2
1.3 Bebionic Hand . . . 4
1.4 iLimb Hand . . . 5
1.5 Body-Powered Prosthetic Hand . . . 6
1.6 Dextrus Hand . . . 7
1.7 Ada Hand . . . 7
1.8 Wits prosthetic hand (Tact model) . . . 8
1.9 Stress-Strain-Temperature Curve . . . 12
1.10 Temperature Dependence of the Isothermal Forward and Reverse Transformation Plateau Stresses (k_f and k_r are constants with values 6.56 MPa/°C and 7.09 MPa/°C, respectively) . . . 12
1.11 Past Nitinol Powered Prosthetic Hands . . . 13
1.12 University of Waikato SMA Finger Response to Step Input . . . 14
1.13 University of Marmara SMA Finger Response to Step Input . . . 14
1.14 Tsuyama National College SMA Artificial Muscles . . . 15

2.1 Nitinol Actuator Concept . . . 18
2.2 Nitinol Actuator Kinematic Diagram . . . 19
2.3 Nitinol Actuator Schematic (Mark Gummin, Miga Motor Company, personal communication, May 12, 2019) . . . 20
2.4 Nitinol Actuator Prototype . . . 20
2.5 Modified Nitinol Actuator Layout . . . 21
2.6 Two-Link Finger Mechanism . . . 22
2.7 Two-link Finger Mechanism Assembly . . . 23
2.8 Prosthetic Hand Assembly . . . 23
2.9 Actuation Scheme Configuration . . . 24
2.10 Hairspring Bias . . . 24

3.1 Free Body Diagram of Finger Mechanism . . . 25
3.2 Link 2 Orientation with respect to the Finger Base Position Diagram . . . 27
3.3 Detailed Free Body Diagrams of Finger Mechanism . . . 28
3.4 Fingertip Force vs PIP angle for Middle Prosthetic Finger . . . 30
3.5 Dominant Energy Contributions . . . 31
3.6 Input Current Signal with a 980 Hz PWM Frequency . . . 32
3.7 Crank-Slider Mechanism . . . 35

3.8 Simplified Link Diagram of Finger Mechanism . . . 36
3.9 Matlab Code Architecture for Bang-Bang Controlled Nitinol-Driven Finger . 39
3.10 Step Signal with 6 V Input Voltage . . . 40
3.11 Step Signal with 7 V Input Voltage . . . 41
3.12 Step Signal with 8 V Input Voltage . . . 41
3.13 Step Signal with 9 V Input Voltage . . . 42
3.14 Step Signal with 10 V Input Voltage . . . 42
3.15 Step Signal with 11 V Input Voltage . . . 42
3.16 Step Signal with 12 V Input Voltage . . . 43
3.17 Step Signal with 13 V Input Voltage . . . 43
3.18 Time Constant (Heating) vs. Input Voltage . . . 44
3.19 Time Constant (Cooling) vs. Input Voltage . . . 44

4.1 Sliced 3D Model for 3D Printing . . . 45
4.2 Hand Assembly Prototype . . . 46
4.3 Finger Assembly Prototype . . . 46
4.4 Hand Tactile Sensor . . . 47
4.5 Prosthetic Hand Outfitted with Finger Pad Sensors . . . 48
4.6 Adaptive Grip Control Loop . . . 48
4.7 Duty Cycle . . . 49
4.8 Arduino UNO Board . . . 50
4.9 Prosthetic Hand Circuit . . . 51
4.10 Arduino UNO Close Up View from the Prosthetic Hand Circuit . . . 52

5.1 MPU6050 Sensor . . . 54
5.2 Finger Positioning Test Apparatus . . . 55
5.3 Finger Positioning Test Circuit . . . 56
5.4 7 V Step Signal . . . 57
5.5 9 V Step Signal . . . 57
5.6 11 V Step Signal . . . 58
5.7 7 V Ramp Signal . . . 60
5.8 7 V Ramp Signal Error . . . 61
5.9 9 V Ramp Signal . . . 61
5.10 9 V Ramp Signal Error . . . 61
5.11 11 V Ramp Signal . . . 62
5.12 11 V Ramp Signal Error . . . 62

6.1 Labelled Prosthetic Fingers . . . 64
6.2 Fingertip Strength Test Rig . . . 65
6.3 Finger Grip Strength Test Rig . . . 66

6.4 Fingertip Contact Force with a PIP Angle of 0° 68
6.5 Fingertip Contact Force with a PIP Angle of 30° 68

7.1 Hand gestures 70
7.2 Objects to Test Hand Grip Performance 71
7.3 Five-fingered Grips 72
7.4 Three-fingered Grips 72
7.5 Two-fingered Grip 73
7.6 Hand Gripping Irregularly Shaped Objects 73

9.1 Modified Nitinol Actuator Layout 77

C.1 Simplified Link Diagram of Finger Mechanism 98

List of Tables

1.1 Average Grip Strength 3
1.2 Grip Strengths of Prosthetic Hands 9
1.3 Nitinol Wire Properties 11

2.1 Nitinol Actuator Mechanical Specifications 19

3.1 Bias Spring Parameters 26
3.2 Middle Finger Parameters 40

4.1 PLA Printing Parameters for Prosthetic Hand Parts 45
4.2 Cost Estimation 53

5.1 Results for Step Signal Positioning Test 59
5.2 Average Path Tracking Error 63

6.1 Finger Grip Strength Results 69

C.1 MPU6050 Sensor Uncertainties 101

D.1 Prosthetic Hand Circuit Connections 103

Nomenclature

Roman Symbols

Variable/Parameter	**Symbol**	**Units**
Austenite finish temperature	A_f	°C
Austenite start temperature	A_s	°C
MCP joint to Link 1 joint displacement	b	mm
Nitinol specific heat capacity	c	J/°C kg
Nitinol contraction force	F_{wire}	N
Gravitational acceleration	g	m/s^2
Convective heat transfer coefficient	h	W/m^2 K
Nitinol latent heat	Δ H	J/kg
Current supply to actuator	I	A
Bias leaf spring constant	k	N/mm
Finger base length	L_1	mm
Finger segment length	L_2	mm
Link 2 length	L_3	mm
Nitinol wire length	L_{wire}	mm
Nitinol wire mass	m	kg
Finger base mass	m_1	kg
Finger segment mass	m_2	kg
Martensite finish temperature	M_f	°C
Martensite start temperature	M_s	°C
Fingertip force	N	N
Nitinol wire surface area	S	mm^2
Nitinol wire temperature	T	°C
Cooling period time constant	t_c	s
Torsional bias	T_f	Nmm
Heating period time constant	t_h	s
Actuation torque	T_p	Nmm
Ambient temperature	T_∞	°C

Greek Symbols

Variable/Parameter	**Symbol**	**Units**
Bias leaf spring deflection	δ	mm
Nitinol wire strain	ϵ	mm
Finger angle (MCP angle)	θ_1	$^\circ$
PIP angle	θ_2	$^\circ$
Nitinol density	ρ	g/mm^3
Nitinol wire stress	σ	Pa
Torque load on MCP joint caused by finger's momentum	τ_1	Nm
Martensite fraction	ξ	-

1 Introduction and Literature Survey

1.1 Background and Motivation

It is estimated that there are more than 350 000 people in South Africa living with disabilities caused by amputations [1]. In developed countries, it is approximated that 65% of amputations arise from diseases such as diabetes, vascular complications or tumours. Of these amputations only 35% are caused by a traumatic injury which can occur during an accident, work or war. In undeveloped nations such as the countries in Sub-Saharan Africa, the majority of amputations are a result of traumatic injury. This is due to the poor infrastructure and political instability found in these countries. Amputees in Sub-Saharan Africa are likely to experience negative effects on their physical, social, and psychological well-being [2]. These negative effects can be reduced by using prostheses which return some functionality lost by the missing limb.

Prostheses such as a robotic hands often cost upwards of $11 000 [3]. This is unaffordable for most South African citizens. Furthermore, due to poor service delivery and a lack of highly skilled staff, it is more difficult to obtain a prosthesis through state-run organizations in developing countries than in developed countries [4]. This leads to the mishandling of patients in many cases. Many amputees do not receive proper prostheses because of insufficient resources in underdeveloped nations. Easily accessible, low-cost, highly functional prostheses are required to improve the quality of life for amputees in developing countries.

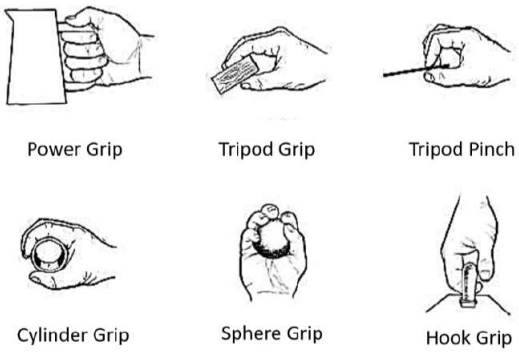


Figure 1.1: Hand Gestures [5]

The University of the Witwatersrand (Wits) designed and developed a 3D printed upper limb prosthetic. The hand was designed to perform the hand gestures shown in Figure 1.1, to be classified suitable for everyday use. Due to the use of low-cost servomotors the prototype lacked sufficient grip strength and mechanical durability. But since implementing better servomotors would significantly increase the cost of the prosthetic, it was recommended that a new actuation system should be designed [6].

1.2 Literature Survey

1.2.1 Anatomy of the Hand

The hand is made up of different bones, muscles, and ligaments that provide a wide range of motion (ROM) and dexterity. Multiple muscles and tendons form the actuation mechanism of the hand. The muscles are the structures that contract when activated, acting as the actuators within the hand, while the tendons connect the muscles to the bone, transferring the actuation movement. There are 3 types of bones within the hand [7]:

- **Phalanges**. The 14 bones that form the fingers of each hand. Each finger has 3 phalanges (the distal, middle, and proximal); the thumb only has 2.
- **Metacarpal bones**. The 5 bones that compose the palm of the hand.
- **Carpal bones**. The 8 bones that make up the wrist.

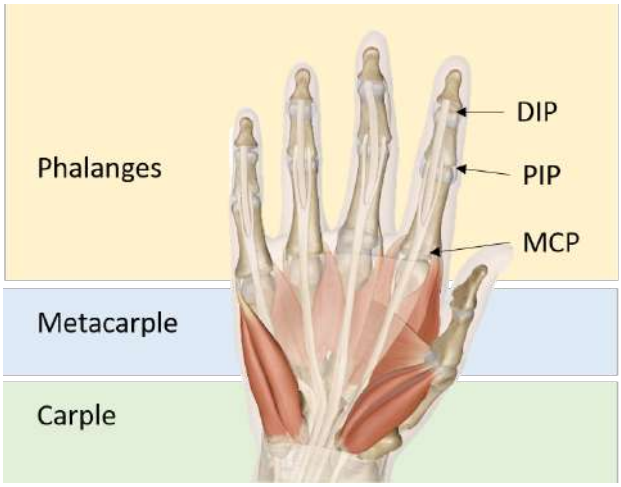


Figure 1.2: Hand Anatomy [8]

The metacarpophalangeal joint (MCP) is a synovial saddle joint, which connects the proximal phalanges to the metacarpal bones. The joint can perform flexion-extension, abduction-adduction and opposition movements. The proximal interphalangeal joint (PIP) and distal interphalangeal joint (DIP) are hinge joints, which connect the different phalanges within the finger together. These joints can perform flexion-extension movements [8]. All the different joint movements within the hand, excluding the wrist joint, enable 21 degrees of freedom (DOF).

When the muscles, tendons and phalanges work in tandem with one another, it enables the hand to manipulate objects and perform different types of grasps. Depending on the nature of the action, a certain force threshold is required. For example, using a light switch requires the fingertip to exert sufficient force to push the switch down, whereas holding a cup requires all the fingers to impart a grip force onto the cup to hold it. Therefore, it is difficult to

classify the grip force and fingertip force required by a prosthetic hand to fulfill the needs of an anthropomorphic hand based on the gestures and grips the hand performs, due to the countless actions and objects a hand may encounter.

In Table 1.1, it can be seen that the average grip strength varies depending on age and sex. Hence, human grip strengths also do not present a consistent standard for a prosthetic hand to achieve. It is difficult to classify women with lower grip strengths as being hindered in their everyday life compared to men, or that children (ages between 10-15) struggle to use their hands with their lower grip strengths. However, it also cannot be said that a grown man could adequately cope with their everyday activities with the grip strength of a child, since the grip strength required by an adult may vary from a child.

Therefore, other commercially available and 3D printed prosthetic hands should be used as a standard for grip and fingertip strength for the prosthetic hand being developed. Since, the hand grip and fingertip strengths remain constant and have been proven to work and perform the necessary actions of a prosthetic hand.

Table 1.1: Average Grip Strength [9]

	Male			**Female**		
Age (Years)	**Weak (kg)**	**Normal (kg)**	**Strong (kg)**	**Weak (kg)**	**Normal (kg)**	**Strong (kg)**
10-11	<12.6	12.6-22.4	>22.4	<11.8	11.8-21.6	>21.6
12-13	<19.4	19.4-31.2	>31.2	<14.6	14.6-24.4	>24.4
14-15	<28.5	28.5-44.3	>44.3	<15.5	15.5-27.3	>27.3
16-17	<32.6	32.6-52.4	>52.4	<17.2	17.2-29.0	>29.0
18-19	<35.7	35.7-55.5	>55.5	<19.2	19.2-31.0	>31.0
20-24	<36.8	36.8-56.6	>56.6	<21.5	21.5-35.3	>35.3
25-29	<37.7	37.7-57.5	>57.5	<25.6	25.6-41.4	>41.4
30-34	<36.0	36.0-55.8	>55.8	<21.5	21.5-35.3	>35.3
35-39	<35.8	35.8-55.6	>55.6	<20.3	20.3-34.1	>34.1
40-44	<35.5	35.5-55.3	>55.3	<18.9	18.9-32.7	>32.7
45-49	<34.7	34.7-54.5	>54.5	<18.6	18.6-32.4	>32.4
50-54	<32.9	32.9-50.7	>50.7	<18.1	18.1-31.9	>31.9
55-59	<30.7	30.7-48.5	>48.5	<17.7	17.7-31.5	>31.5
60-64	<30.2	30.2-48.0	>48.0	<17.2	17.2-31.0	>31.0
65-69	<28.2	28.2-44.0	>44.0	<15.4	15.4-27.2	>27.2
70-99	<21.3	21.3-35.1	>35.1	<14.7	14.7-24.5	>24.5

1.2.2 Commercially Available Robotic Prosthetic Hands

Replicating the functionality of the human hand using a bionic device is a significant challenge. The bionic hand's control must be easy, quick and reliable for it to be more advantageous than the fixed grip alternative.

Achieving the complex set of movements necessary to replicate the motor control of the human hand requires an integration with a digital control method. These methods can be as simple as placing a control unit into the user's shoe, or as complex as myoelectric control that interprets electrical activity in the neuromusculature of the limb stump to activate the prosthesis [10].

With rapid developments in technology, bionic hands are getting closer to fully mimicking the human hand. These hands are designed to have the same degrees of freedom as a human hand, by articulating all the finger joints with specialised miniature motors. However, these bionic hands are expensive to develop and often too costly for the typical user in developing countries.

1.2.2.1 Bebiobic Hand

The Bebiobic hand is a commercially available prosthesis that retails for $30 000 [11]. The bionic hand gained popularity due to the 14 achievable grips which could be attained, enhancing the dexterity and user experience of the hand. The range of grips are possible due to each finger joint being independently actuated as well as the passive rotation incorporated in the thumb [12].



Figure 1.3: Bebionic Hand [12]

1.2.2.2 iLimb Hand

The iLimb hand is a myoelectric powered prosthesis which retails between $60 000 and $120 000, depending on the model's specifications. Similar to the Bebonic hand, each finger joint is fully articulated. The thumb has a fused MCP joint and passively rotates at its base, which allows it to oppose the tip or side of the index finger. This is beneficial for tasks which require precision [13].

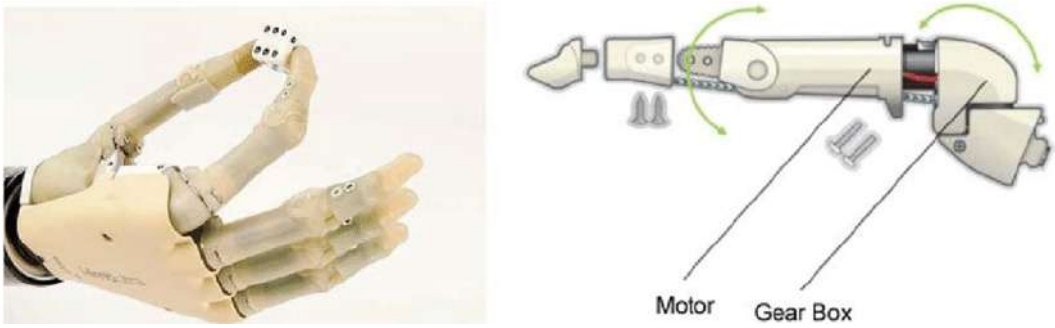


Figure 1.4: iLimb Hand [13]

1.2.2.3 EMG Pattern Recognition Sampling Frequency

For the prosthetic to perform reliably a stable connection between the user and device needs to be established. The monitoring of electromyography (EMG) signals can be used to link the user to the prosthesis. When muscles contract, EMG signals are propagated through the surrounding tissue. These signals can then be detected at the skin's surface using EMG sensors [14]. Currently, this technology is used in commercial prosthetic hands as a means for the user to communicate with the prosthesis. Therefore, EMG sensors will be used to control the SMA actuators in the 3D printed hand.

However, after amputation, there is rarely sufficient muscle left to intuitively control a robotic prosthesis. A method for dealing with this drawback is to implement EMG pattern recognition. This works on the assumption that EMG patterns capture information about the desired movements from the residual muscles. The effectiveness of the pattern recognition is dependent on the sampling frequency, which determines the refresh rate of the EMG signals. The sampling frequency needs to be high enough to effectively capture real-time data and prevent a slow response.

A 1 kHz sampling frequency is typically used for EMG pattern recognition. The high sampling frequency captures ample myoelectric signals but adds more processing and computational complexity to the controller of a prosthesis. However, it was found that a sampling frequency of 500 Hz resulted in a 2.2% loss in pattern recognition accuracy [14]. This was deemed acceptable as it would still allow for proficient grip control while lowering the computational requirements of the controller.

1.2.3 Past 3D Printed Robotic Prosthetic Hands

The most basic, controllable prosthetic hand designs rely on cable systems fixed to a harness that a user wears. The motion of the residual limb relative to the user's body triggers the movement of the prosthesis. These designs are cheap to produce and are relatively easy to use, so they can be a suitable option for people with low demands. An example of such a design is shown in Figure 1.5.

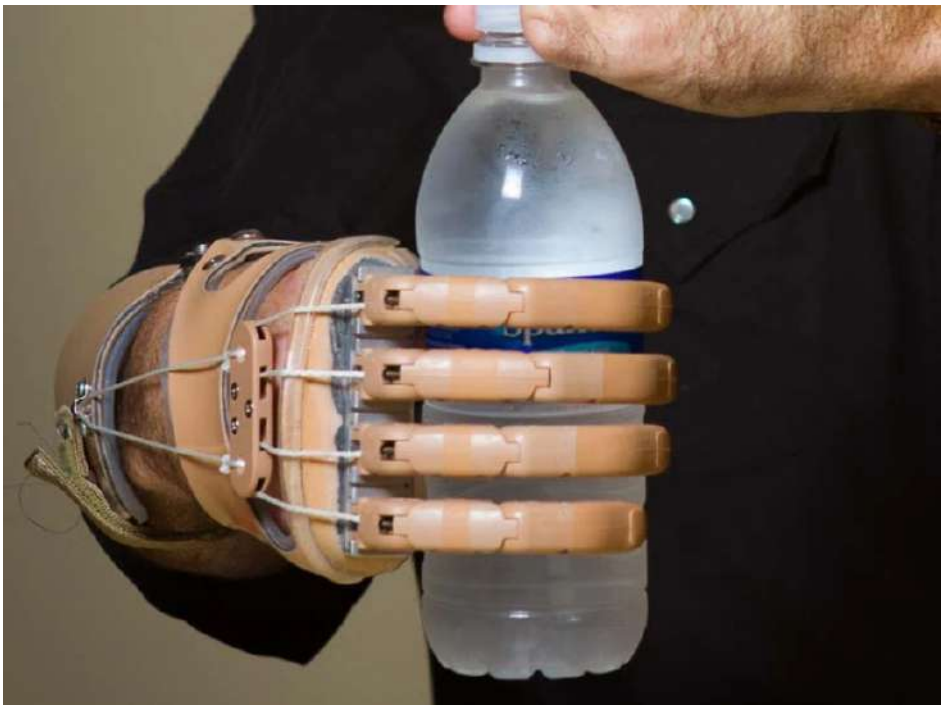


Figure 1.5: Body-Powered Prosthetic Hand [15]

However, these limbs require the user to have sufficient strength to operate them and are restricted to a small set of basic movements, reducing the overall utility of the prosthesis. The body-powered hands lack the dexterity and precision achievable with actuator-driven hands, such as the iLimb and Bebionic hands. 3D printing coupled with open source platforms has lead to the rapid development of more affordable prosthetic hands with similar motor control performance to commercially available options.

1.2.3.1 Dextrus Hand

As shown in Figure 1.6, the tendon driven hand was developed by The Open Hand Project. All of the motors and electronics are fitted inside the hand's palm, accommodating for a range of different amputees.

The hand is designed to connect to an existing fitted prosthesis using standard connectors, meaning it can be used without a custom fitting. An intuitive and simple control system is implemented using two EMG sensors attached to the residual arm [16].



Figure 1.6: Dextrus Hand [16]

1.2.3.2 Ada Hand

The Ada Hand is a robotic hand developed by Open Bionics. It is sold as a pre-manufactured easy to assemble kit. The fully articulated hand has five degrees of freedom and is controlled via computer with a USB connection. Outfitted with a custom PCB designed around the ATMEGA 2560 microcontroller, the hand itself stores all of the actuators to move the fingers and can be programmed using the Arduino programming language. Similar to other bionic hands, the control of the device can be integrated with the user using EMG sensors to track the muscle contractions in the residual limb [17]. The non-invasive implementation makes this more popular than both invasive methods, such as medical implants, and less subtle equipment such as neural implants.



Figure 1.7: Ada Hand [17]

1.2.3.3 Wits 3D Printable Hand Prosthesis

The Wits 3D printed prosthetic hand designed by Irfaan Mohamed is based on the open-source Tact hand. The Tact design is a myoelectric 3D printed hand developed to solve the need for prostheses in developing countries [18]. A prototype of the Tact hand is shown in Figure 1.8.

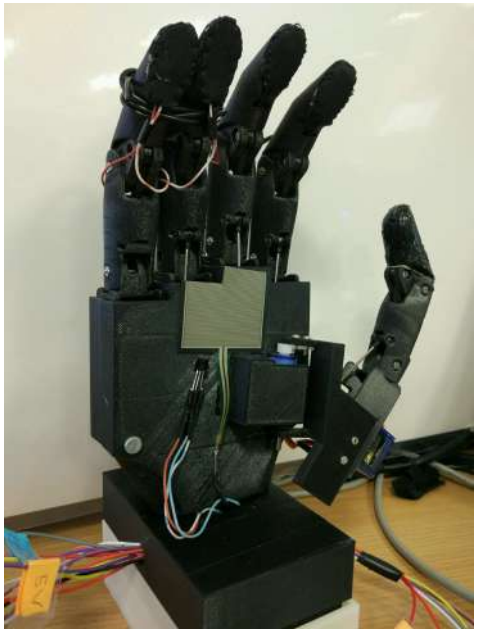


Figure 1.8: Wits prosthetic hand (Tact model) [6]

The Tact design was chosen as it offers the same functionality as commercial hand prostheses and improved performance over other open-source designs. Polylactide (PLA) was selected as the material because of the higher printing quality achieved compared to acrylonitrile butadiene styrene (ABS). The system makes use of SG90 servo motors since they offer the best functionality for the price constraint of R3 000. The motors are controlled using an Arduino UNO microcontroller board which is fed sensor data from electromyography (EMG) sensors attached to the residual arm [6].

The 2017 prototype of the Tact hand included a haptic feedback system which allowed the user to judge the grip strength of the hand. The prototype was able to perform all five of the hand movements required for daily use: tripod pinch, power grip, cylinder grip, sphere grip and hook grip [5], and achieved a maximum power grip strength of 6 N.

1.2.3.4 Shortcomings Encountered in 3D Printed Robotic Prosthetic Hands

3D printing is gaining popularity as an inexpensive manufacturing method as well as a means for rapid prototyping. This trend has led to the creation of platforms which connect various professionals to collaborate in open source projects, such as the Tact hand. Most open-source prosthetic hands utilise tendon-driven systems to actuate the prosthesis. This decreases the number of degrees of freedom, simplifies the control and reduces the overall

cost. Tendon-driven systems employ underactuation and utilise motors, to linearly actuate cables connected through the finger segments. The cables are fixed to the fingertips and curl the fingers inwards when pulled. Various open-source projects like the Open Hand Project (Dextrus) and Open Bionics (Ada Hand) have successfully implemented tendon-driven systems.

The major drawback encountered with the systems is the lack of achievable grip strength that the motors can attain [18, 19, 20]. Actuation is not direct but through tendons; and thus energy is dissipated, and grip strength is reduced. The Wits hand achieved a power grip force of 6 N [21]. Commercially available hands such as the Bebionic and iLimb produce forces significantly larger than the Wits hand [22]. These forces are presented in Table 1.2.

The Bebiobic and iLimb hands make use of linear drivers to actuate their fingers. While this improves the positioning and finger strength performance, it is considerably more expensive than tendon-driven systems. Consequently, there exists a need to develop an actuation mechanism that addresses both the poor grip strength performance of tendon-driven servomotor systems, as well as the high cost of the linear drivers used in commercially available hands.

Table 1.2: Grip Strengths of Prosthetic Hands [21, 22]

	Power Grip (N)	**Precision Grip (N)**	**Fingertip Force (N)**
Bebionic	75	34	12.47
iLimb	-	10.8	5.39
Wits Hand	6	-	-

1.2.4 Alternative Actuation Methods

Traditionally, low-cost electric motors are too big to be placed within the prosthetic hand and have to be used remotely, ahead of the wrist joint. This increases the overall complexity of the mechanical design and incurs large force transfer inefficiencies since tendons passed through the wrist joint are used to drive the fingers, as discussed in Section 1.2.3.4. Due to these constraints, most low-cost 3D printed hands have failed to provide sufficient grasping functionality. Therefore alternative actuation methods such as pneumatic, shape memory alloys and electroactive polymers are considered.

1.2.4.1 Pneumatic Actuation

Pneumatic actuators use pressurised gas to flow into an actuation chamber to provide an actuation force. When the pressure differential between the chamber and the atmosphere is large enough, it results in the controlled kinetic movement of a device such as a piston or gear. An example of a pneumatic actuator which could be suitable for prosthetic applications

is the McKibben Artificial Muscle [23]. Its properties are found to be similar to real muscle with regards to its physical flexibility and light weight.

1.2.4.2 Shape Memory Alloy Actuation

Shape memory alloys (SMAs) are a specialised subgroup of metals which exhibit sensing and actuating capabilities when in contact with an electrical or thermal catalyst. Nitinol is an SMA which has a nickel-titanium composition. It can bend and deform mechanically while recovering its original shape when exposed to a suitable stimulus. This is due to Nitinol being able to exist in two crystal phases, austenite (higher temperature) and martensite (lower temperature). Therefore, Nitinol achieves a shape-memory effect through a thermal cycle which involves a crystallographic transition between low and high-temperature phases [24, 25]. This property enables Nitinol wires to be linear actuators which contract when heated ohmically, generating a linear displacement.

1.2.4.3 Electroactive Polymers Actuation

Electroactive polymers actuation (EAP) materials are polymers that change size or shape in response to electric stimulation. Through research, EAPs have been shown to demonstrate strains as high as 300% when stimulated. EAPs are utilised as linear actuators in arrangements known as 'spring rolls', where several layers of dielectric EAP sheets are wrapped around a helical spring. The spring supports the circumferential prestrain while the lengthwise prestrain holds the spring compressed. When a voltage is applied, the EAP sheets compress in thickness and expand in length, causing the device to extend and generate a linear stroke [26].

1.2.4.4 Review of Alternative Actuation Methods

Pneumatic artificial muscles used in bionic hands such as the robotic hand have shown promising grasp strength performance results, achieving a strength to weight ratio of 400:1 for the device [27]. However, pneumatic actuators require a circulatory system for the pressurized gas. Furthermore, the muscles tend to be too big to fit into the hand structure. Forcing the actuation scheme to act remotely similar to low-cost electric motors. Hence, pneumatic systems are not suited for prosthetic applications.

Unlike pneumatic actuators and low-cost motors, EAP and SMA actuators don't rely on gears, bearings, valves and circulatory systems. The material itself acts as the actuation mechanism. The small, lightweight, direct-driven actuators mobilise prosthetic hands without adding mechanical complexity. However, EAPs have low actuation forces and mechanical energy density, and require high voltages to operate, making them impractical to use in prosthetic limbs. Therefore, the high strength to weight ratio, small activation voltage and compact size of SMA actuators make them the practical choice to use in a prosthetic hand [28].

1.2.5 Principles of Shape Memory Alloy Behaviour

Nitinol wire actuators use the pulling force generated when the wire contracts during heating. This contraction is usually 2-10% of the total length of the wire [29]. The mechanical properties of Nitinol wire during contraction are presented in Table 1.3.

Table 1.3: Nitinol Wire Properties [29]

Wire Diameter (mm)	**Resistance (Ohms/mm)**	**Maximum Pulling Force (g)**	**Contraction Time (s)**
0.254	0.021	930	1
0.305	0.013	1250	1
0.381	0.008	2000	1

1.2.5.1 Stress-Strain-Temperature Relationship of Nitinol Wire

Nitinol can recover from strains as large as 10% of its total length, as illustrated in Figure 1.9. Assuming the material begins in the detwinned martensite state (1'), the material must be heated to the transformation temperature to transform the Nitinol from detwinned martensite to austenite (2). The shape memory effect activates through a stress-driven isothermal process. The isothermal process converts the austenite structure to martensite (3). After the process, strains up to 10% can be created. Once, the stress is removed, the full strain is recovered as the Nitinol returns to the austenite state. It can be seen that the removed stress path differs from the applied stress path, forming a hysteric process. The difference is due to the additional energy required to convert austenite to martensite, which is unnecessary for the reverse [30]. Using experimental data from [30], the tri-axis stress strain temperature curve can be reduced to Figure 1.10.

1.2.5.2 Temperature Induced Transformation

As illustrated in Figure 1.9, processes (1)-(2) and (2)-(4) are dependent on temperature. Hence, the Nitinol's transition from martensite to austenite and vice versa can be expressed in terms of temperature by Equations 1.1 and 1.2, where ξ represents the martensitic fraction during the transition phase [30]:

For detwinned martensite to austenite

$$\xi_h = \frac{1}{2}\left[1 - \cos\left(\pi \frac{T - A_s}{A_f - A_s}\right)\right] \tag{1.1}$$

For austenite to martensite

$$\xi_c = \frac{1}{2}\left[1 + \cos\left(\pi \frac{T - M_f}{M_s - M_f}\right)\right] \tag{1.2}$$

Where A_s and M_s are the transformation temperatures for austenite and martensite, respectively, A_f and M_f are the temperatures at which the crystal structure is fully transformed into austenite and martensite, respectively.

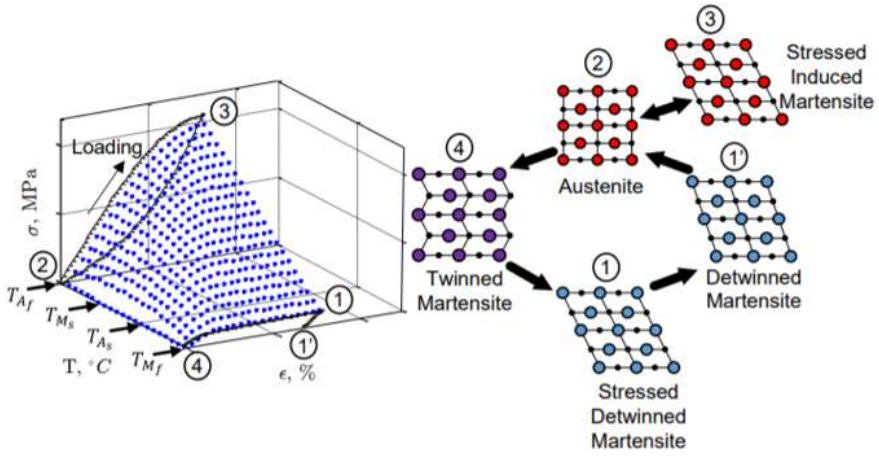


Figure 1.9: Stress-Strain-Temperature Curve [30]

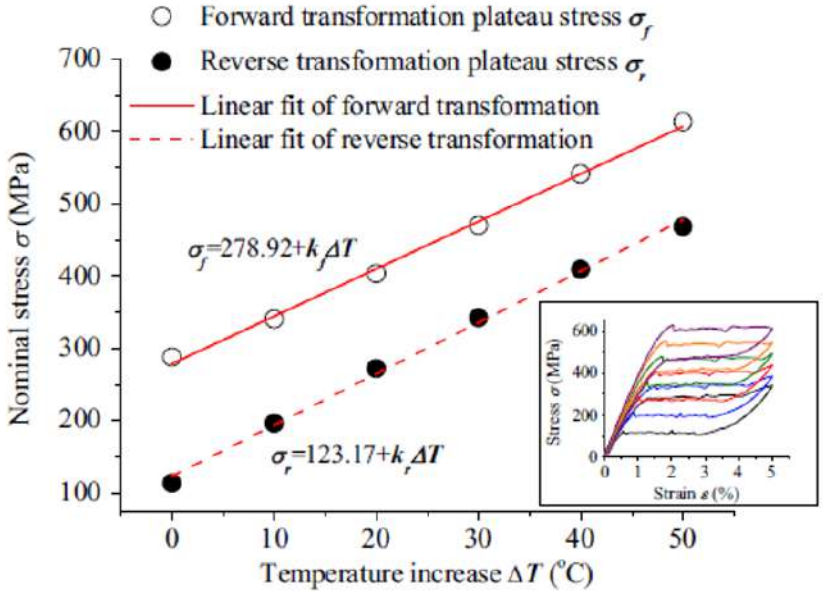


Figure 1.10: Temperature Dependence of the Isothermal Forward and Reverse Transformation Plateau Stresses (k_f and k_r are constants with values 6.56 MPa/°C and 7.09 MPa/°C, respectively) [31]

The energy generated or released during the Nitinol's state shift is classified as the wire's latent heat, E_{stored}, and is calculated using Equation 1.3 [30]:

$$E_{stored} = mc\frac{dT}{dt} - m\Delta H\frac{d\xi}{dt} \tag{1.3}$$

Where m is the mass and c is the specific heat capacity of the wire, and ΔH is the latent heat of the transformation.

1.2.5.3 Uniaxial Loading

Energy is also introduced into the system when the wire is uniaxially loaded. This increases the strain rate of the wire, which is dependent on a stress-driven isothermal process [32]. A tension loaded wire will therefore strain quicker than an unloaded wire. The applied load can be expressed as energy imparted on the system as follows [30]:

$$E_{in} = \dot{W}_{mech} = \frac{1}{\rho}\sigma\Delta\varepsilon_{tr} \tag{1.4}$$

Where, ρ is the Nitinol's density, σ is the uniaxial stress load on the wire, and $\Delta\varepsilon_{tr}$ is the change in transformation strain.

1.2.6 Past Nitinol Powered Prosthetic Hands

Previous research studies have utilised Nitinol as an actuator in prosthetic hands. The Nitinol wires are used to mimic the function of muscle fibres and are fixed to the fingertips and threaded along with the finger [33, 34, 35, 36, 37]. From Figure 1.11, it can be seen that the majority of Nitinol powered hands utilise tendon-driven systems where the Nitinol wires act as tendons. This actuation solution is popular due to the simplification of the system, by eliminating the need for actuators to pull the tendons since the Nitinol tendons are the actuators.

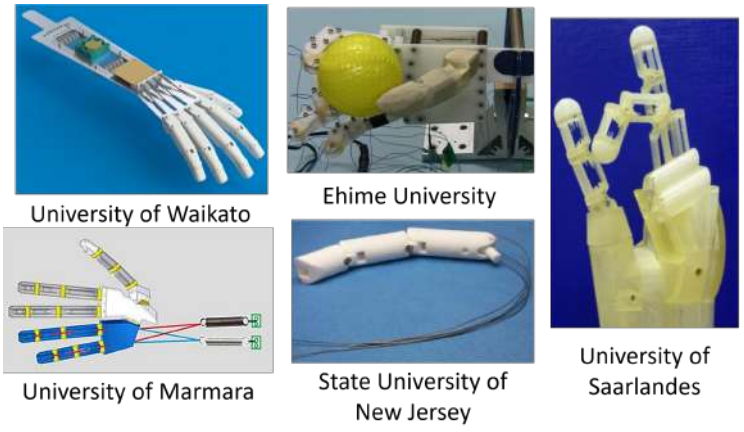


Figure 1.11: Past Nitinol Powered Prosthetic Hands [33, 34, 35, 36, 37]

These past Nitinol powered hands achieved moderate success compared to commercially available prosthetic hands. This was largely due to the slow response time associated with Nitinol wire. The prosthetic hands displayed sluggish positioning capabilities during the Nitinol cooling phase, as illustrated in Figures 1.12 and 1.13. The time constants during

the cooling phase can be graphically deduced and were found to be approximately 3.7 s and 1 s for the Waikato hand and Marmara hand, respectively. However, the Waikato hand also implemented forced cooling, which significantly improved the response time during the cooling phase; yielding a time constant of 0.8 s. However, the addition of the cooling mechanism increases the size, complexity and cost of the prosthesis.

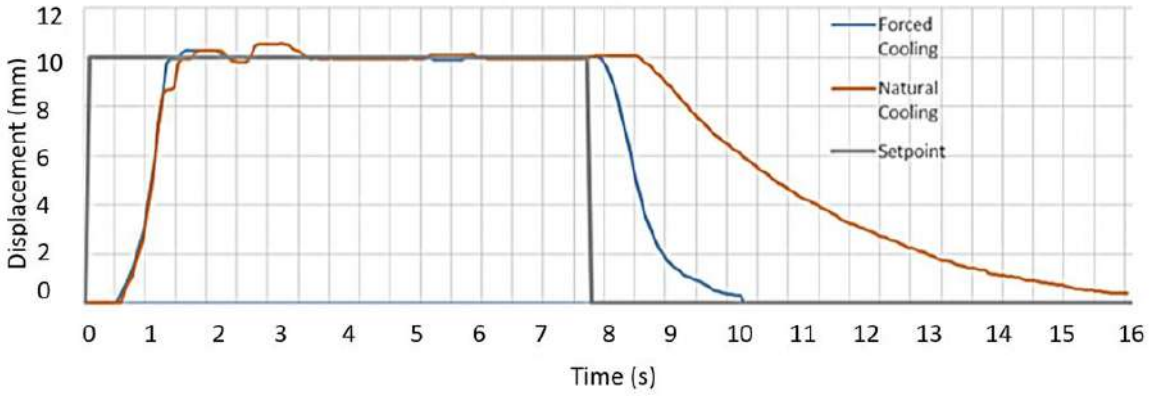


Figure 1.12: University of Waikato SMA Finger Response to Step Input [33]

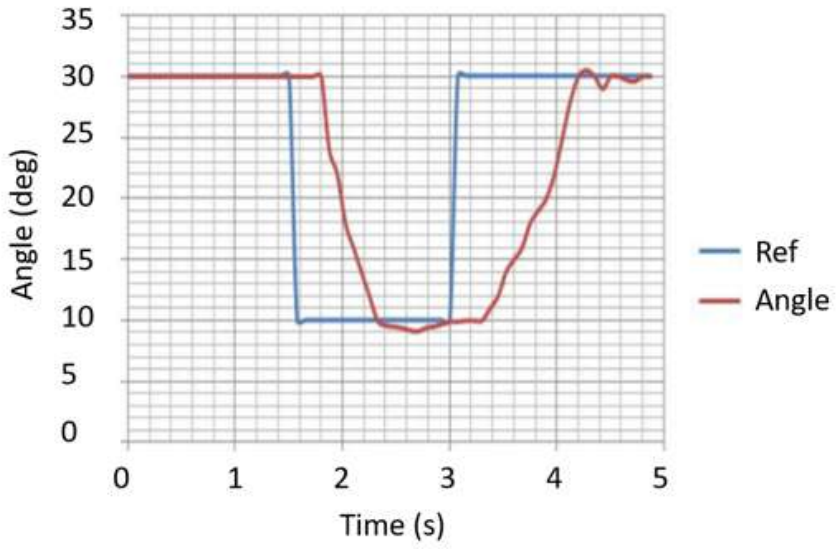


Figure 1.13: University of Marmara SMA Finger Response to Step Input [36]

Another drawback of using Nitinol wires as tendons is that the generated grip force is dependent on the wire length. As discussed in Section 1.2.3.4, tendon-driven systems are inefficient. Therefore, long Nitinol wires are required to actuate the prosthetic fingers to generate a sufficient grip force. This not only leads to a more bulky hand design but also requires a larger power supply to heat the longer wires; reducing the practicality of Nitinol powered prosthetic hands. This suggests that a tendon-driven mechanism is not the solution for high grip strength in a hand prosthesis; using Nitinol wires as linear actuators should be investigated.

1.2.7 Actuator Response Time

An adequate response time is necessary for the functionality of a prosthetic hand. Slow response may lead to ineffective grips for the user due to the hand feeling awkward and unnatural. Consequently, emphasis is often put on the average speeds (°/s) of the prosthetic fingers when designing the hand prosthesis. Typical finger speeds for models such as the Dexterous and Ada Hand are 175.4 °/s and 249.8 °/s, respectively [18]. However, this may prove difficult for SMA actuators, since they are known to have slow response times, as discussed in Section 1.2.8. Further research into the shortcomings of the SMA response time on the prosthetic hand's positioning capabilities is needed.

1.2.8 Past Shape Memory Alloy Actuators

Early dynamic applications of SMAs were based on ambient temperature-controlled devices such as valves and thermostats. Over time, the inclusion of control schemes allowed for more complex applications, where the shape could be manipulated for the desired response. Advantages of SMAs over other actuating systems include their low-space requirement, minimal noise and low cost. Drawbacks of SMAs include their low efficiency, control complexity and slow response time [24].

The feasibility of utilising Nitinol wires in hand prostheses was discussed in Section 1.2.6. However, the researchers used the wires like tendons instead of linear actuators; similar to the actuation mechanisms of past 3D printed hands, as discussed in Section 1.2.3.4. This directs the Nitinol pulling force inefficiently, reducing the overall grip strength achieved. Employing Nitinol wires inside of linear actuators would allow for configurations which better utilise the wires, generating larger forces and displacements.

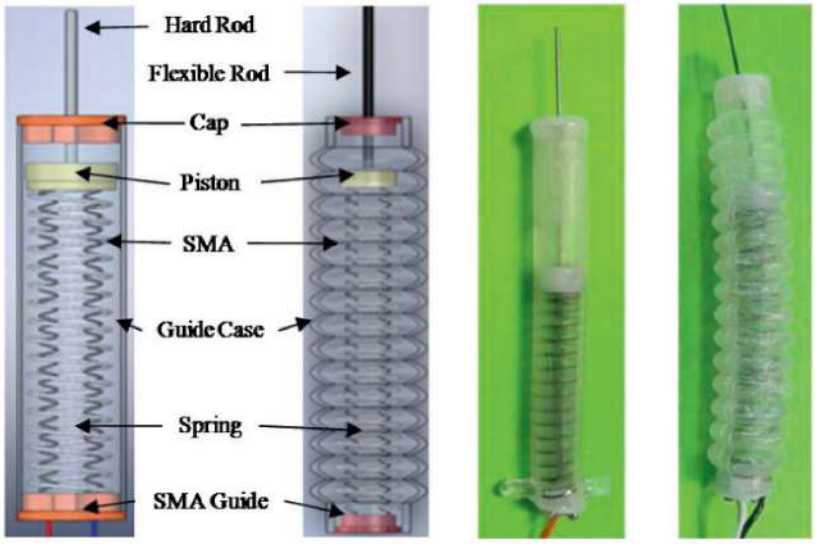


Figure 1.14: Tsuyama National College SMA Artificial Muscles [38]

The Tsuyama National College of Technology in Japan successfully implemented SMA wires with a linear actuator. The artificial muscle is shown in Figure 1.14 and consists of two coiled SMA wires, a piston made of resin, an SMA guide, a cap, a guide case made from silicone, a helical compression spring and a rod made from SMA or high-speed steel. The contraction of the SMA artificial muscles are controlled by modulating the applied heat. When the coiled SMA wires are heated, they contract to the memorised shape and pull the piston rod downwards. When the heating element is switched off, the SMA springs naturally cool down and extend back up, driving the piston rod upwards as well. Therefore, the positioning of the piston is effectively controlled by the current flowing through the heating element of the SMA artificial muscles [38].

1.2.9 Literature Review Summary and Implications for this Research

The 2017 Wits hand prototype is only considered partially successful due to the insufficient maximum grip strength of 6 N [6]. This is lower than the peak grip strengths of commercial devices such as the Bebionic, which achieves a 75 N power grip [22]. The poor grip strength is due to the tendon actuation mechanism as well as the use of low-cost servomotors. Better servomotors are expensive and would increase the cost of the prosthesis significantly. Therefore, it is recommended that an artificial muscle actuation scheme be developed to replace the servomotors.

SMAs are proposed as artificial muscles to actuate a prosthetic hand, due to the high strength to weight ratio. Nitinol wires produce a large contraction force when heated, which increase with wire length. Their versatility, low space requirements, minimal noise and relatively low cost compared to electric motors and pneumatic cylinders make SMAs a feasible solution worth evaluation.

This proposed solution is justified by past designs which utilised Nitinol instead of motors to actuate prosthetic hands using tendon-driven systems. A tendon-driven system reduces the degrees of freedom; simplifying the design.

The inefficient force transmission in tendon-driven systems requires a large pulling force. For Nitinol wires, the pulling force is dependent on the wire length. Therefore, past Nitinol powered prosthetic hands required long Nitinol wires, reducing the practicality of the hands because of the overall length of the prosthesis. This suggests that a tendon-driven system is inadequate for generating a sufficient grip force in low-cost prosthetic hands. A new force transmission scheme which utilises the Nitinol wires in linear actuators and not as tendons needs to be developed and evaluated.

A Nitinol powered prosthesis needs to perform six mandatory grips: power grip, cylinder grip, sphere grip, hook grip and tripod pinch and grip. A common drawback associated with Nitinol actuation is the sluggish response time during the cooling phase. Past Nitinol powered

hands recorded time constants between 1 s and 3.7 s during the cooling phase of the Nitinol wire. This is problematic since commercial prosthetic hands have finger speeds of 175.4 °/s and 249.8 °/s [18]. The sluggish nature of the Nitinol wire actuation needs to be accounted for in the design, for the hand to obtain the dexterity to perform the fine motor skills required.

1.3 Research Questions

The following research questions pertain to the Nitinol-driven 3D printed prosthetic hand with a modified link based transmission system designed in this dissertation.

1. What are the positioning capabilities of a Nitinol-driven 3D printed prosthetic hand?
2. What is the maximum grip and holding strength that can be attained with a Nitinol-driven actuation scheme in a 3D printed prosthetic hand?
3. Does the Nitinol-driven prosthetic hand provide sufficient functionality and dexterity to be useful for daily tasks?

1.4 Research Objectives

The focus of this study is to determine the feasibility of utilising Nitinol actuators to actuate a prosthetic hand. The performance of the Nitinol actuated prosthetic hand is compared to servomotor-actuated hands where such data is available in the literature. This task is translated into the following objectives:

1. Determine the response time, positioning accuracy and strength of a single Nitinol-driven prosthetic finger.
2. Determine the grip strength of the Nitinol-driven prosthetic hand performing both power and precision grasps.
3. Determine the effectiveness of a Nitinol-driven prosthetic hand to conduct the following hand gestures or grips: power grip, tripod grip, tripod pinch, cylinder grip, sphere grip and hook grip.

2 Prosthetic Hand Design

2.1 Nitinol Actuator Design

The proposed solution is a micro electric actuator powered with a Nitinol wire similar to the Tsuyama National College artificial muscles, which were discussed in Section 1.2.8. Only a single Nitinol wire is used instead of two Nitinol coils; reducing the cost and complexity of the actuator. The wire is wrapped around a pulley joint which is free to move linearly, as depicted in Figure 2.1. The operating principle of the actuator is based on the Nitinol wire forming a resistive electrical circuit. An input current is used to ohmically heat the wire element which contracts once a threshold temperature of 75 °C is reached. Due to the wire fixtures, the pulley joint moves linearly when the Nitinol contracts. The actuator is mounted onto the circuit board used to activate the Nitinol. A composite leaf spring is used as a bias to reset the stroke position when the actuator is deactivated, as illustrated in the Figure 2.3. Therefore, the actuator operates using a heating and cooling cycle, contracting when heated and extending when cooled.

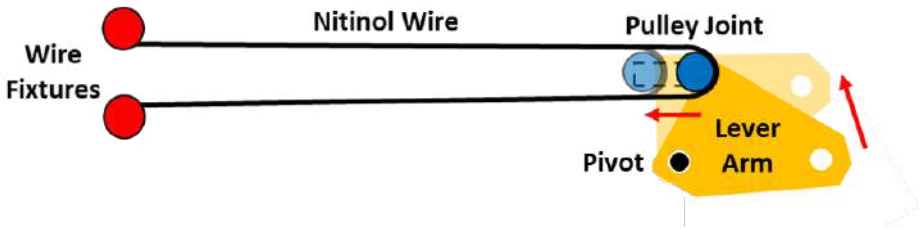


Figure 2.1: Nitinol Actuator Concept

The generated displacement during Nitinol contraction is predictable. Nitinol wire contracts between 2-5% when activated, as discussed in Section 1.2.5. The Nitinol displacement is therefore dependent of the wire length. This displacement is increased further with a lever arm to create a larger stroke. However, increasing the lever arm decreases the pulling force of the actuator. This is established when examining the kinematic relationships of the actuator. The bias force of the composite spring is assumed to have negligible effects on the actuation force. This is because the contraction force of the Nitinol when heated, is much larger than the composite spring bias force.

From Figure 2.2, the actuator mechanics can be analysed.

$$\Sigma M_{pivot} = 0 \tag{2.1}$$

$$F_{pull} L_2 - 2F_{wire} L_1 = 0 \tag{2.2}$$

$$F_{pull} = \frac{2F_{wire} L_1}{L_2} \tag{2.3}$$

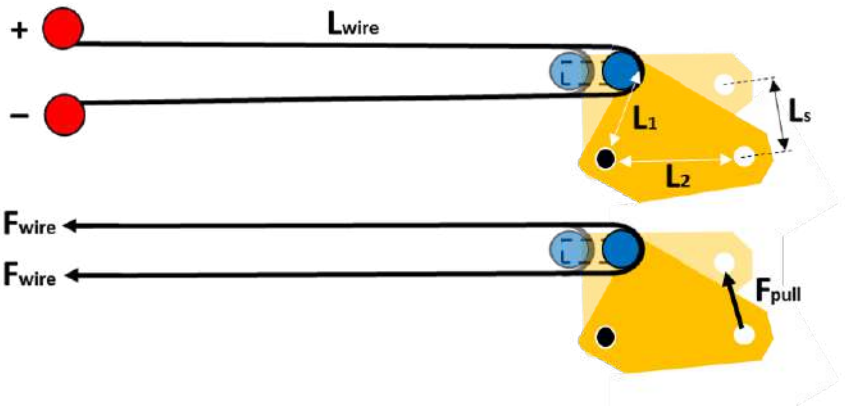


Figure 2.2: Nitinol Actuator Kinematic Diagram

Where F_{wire}, is the pulling force generated by the contraction of the Nitinol wire. The stroke of the actuator is dependent on the wire contraction. It is assumed that the wire will contract 3.5% of the total wire length. The relationship between the stroke and wire length is:

$$L_s = \frac{L_2}{L_1} 0.035 L_{wire} \tag{2.4}$$

For a desired L_s of 9 mm and assuming L_1 and L_2 are 10 mm and 25 mm, respectively. L_{wire} can be calculated using Equation 2.5:

$$L_{wire} = 102.86 \simeq 105 \ mm \tag{2.5}$$

The actuation forces for the corresponding wire diameters can be calculated using Equation 2.3 and the material properties presented in Table 1.3. These results are tabulated in Table 2.1.

Table 2.1: Nitinol Actuator Mechanical Specifications

Wire Diameter (mm)	**Actuator Force (N)**	**Contraction Time (s)**
0.254	7.3	1
0.305	9.8	1
0.381	15.7	1

The actuator prototypes are manufactured by the Miga Motors Company. It is recommended that a MOSFET Miga Analog Driver v5 be used in conjunction with the actuator to regulate the voltage [39]. Signals from a microcontroller can be sent to the MOSFET to activate the actuator. Current ohmically heats the Nitinol, initiating the wire contraction and linear displacement. The displacement length is extended with a lever arm to increase the total stroke to 9 mm. Once the power is removed the wire cools down, returning the actuator

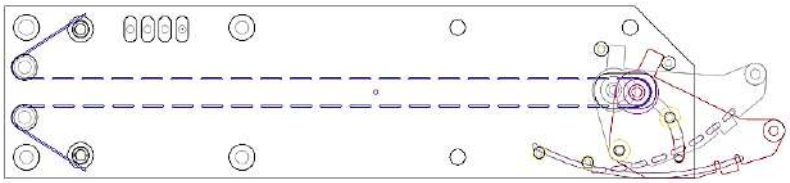


Figure 2.3: Nitinol Actuator Schematic (Mark Gummin, Miga Motor Company, personal communication, May 12, 2019)

to the original position. However, the actuator does not have to fully return to the original position to actuate again. Any position along the stroke can be maintained when coupled with a pulse control scheme. The final actuator prototype is shown in Figure 2.4. The specifications of the actuator prototype are as follows (Mark Gummin, Miga Motor Company, personal communication, May 12, 2019):

- Stroke: 9 mm
- Output Force: range 11 N to 23 N
- Actuation Speed: up to 200 mm/s
- Weight: 18 g
- Dimensions: 115 mm x 25 mm x 2.5 mm



Figure 2.4: Nitinol Actuator Prototype

Although the prototypes are relatively long compared to the electric motors that are currently found in commercial prosthetic hands, the design can be compressed as illustrated in Figure 2.5.

A simplified form of the actuator is used to make the fitting and exchanging of the Nitinol wires easier.

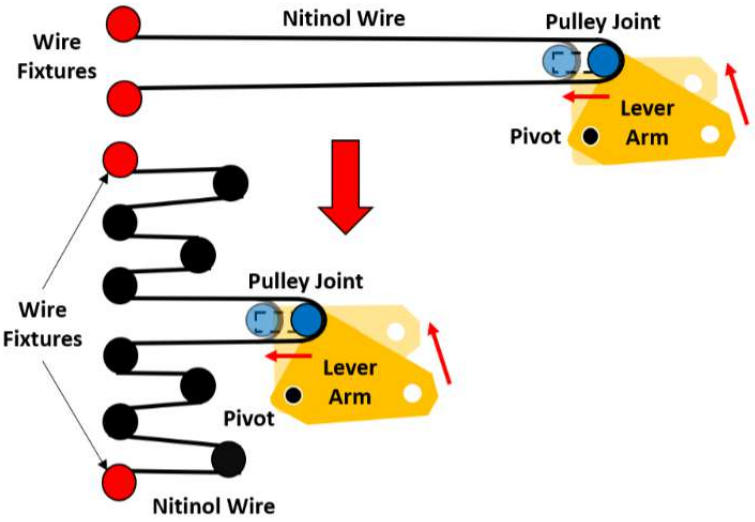


Figure 2.5: Modified Nitinol Actuator Layout

2.2 Finger Mechanism Design

Underactuation is often used in prosthetic hands to simplify design and control. This concept is referred to as mechanical intelligence since part of the mechanical functionality is embedded in the system. A tendon driven system is often used to mobilise the fingers of 3D printed prosthetic hands.

This does, however, lead to a reduction in the overall grip strength due to the ineffective force transmission associated with these mechanisms. This is caused by unwanted friction which is unavoidably introduced into the system [20]. A two-pronged link system coupled with a Nitinol actuator is used to actuate the finger, as shown in Figure 2.6.

There are several prosthetic finger designs in literature which include three phalanges per finger. Using three phalanges per finger follows naturally from anthropomorphism which ensures that the prosthetic can adapt to the shape of arbitrary objects. However, the contact force tends to drop substantially from one phalanx to the next. This is due to the unavoidable friction in the transmission as well as the need to maintain the stability of the finger. The range of motion of the final phalanx (fingertip) is limited. Therefore, reducing the phalanges to two increases the overall grip strength of the finger

To compensate for the loss of mobility in the fingertip, the middle phalanx needs to be extended, and an angle of bend between the finger tip and the middle phalanx needs to be added. According to literature, 20° is a suitable angle of bend between the middle and tip

of the finger for gripping most objects [40]. The two-pronged link mechanism, as well as the bi-segmented finger design, is applied to all five appendages of the hand.

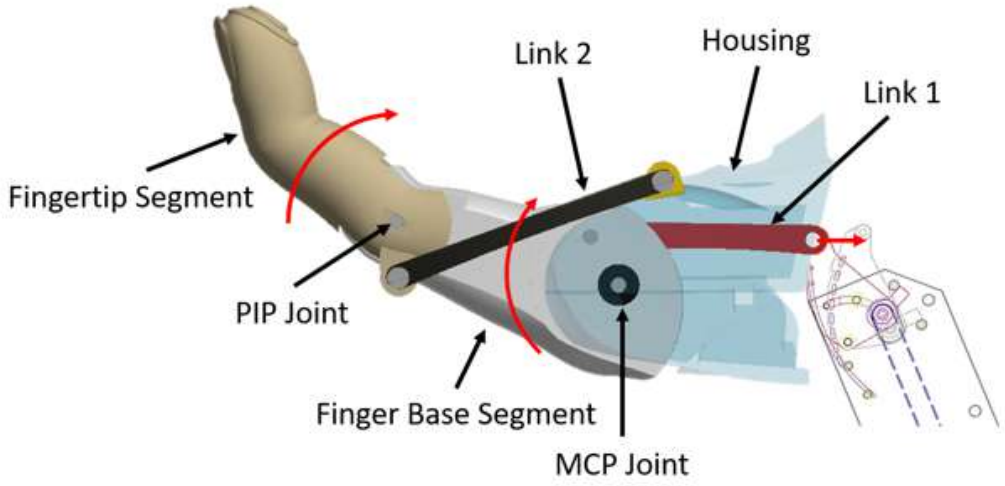


Figure 2.6: Two-Link Finger Mechanism

2.3 Leaf Spring Bias

A major disadvantage of Nitinol actuators is their reaction time. This is dependent on the cool-down period of the Nitinol when the actuator is returning to its original position. The Nitinol actuator accounts for the slower actuation speed during cool down using a composite leaf spring to act as a bias force. However, the composite spring was not sufficient to overcome the additional friction in the two-link finger mechanism. Therefore, a steel leaf spring was fitted to the finger base and housing to produce a secondary bias to reduce the effect of friction, as depicted in Figure 2.7.

SAE-AISI 1070 steel was chosen as the material for the leaf spring. The leaf spring was 0.22 mm thick and 5 mm wide. The length of the spring was determined by the length of the finger mechanism.

2.4 Hand Design

The full hand layout is depicted in Figure 2.8. The spacing of the fingers was designed to ensure all six necessary grips could be executed. The index and middle fingers were spaced closer together to enhance the tripod pinch and grip performance. The tip of the thumb was also widened to improve dexterity and grasping of irregularly shaped objects.

The finger's range of motion is dependent on the length of Link 1 and the placement of the link support, as illustrated in Figure 2.9. However, the orientation of the thumb was purposely

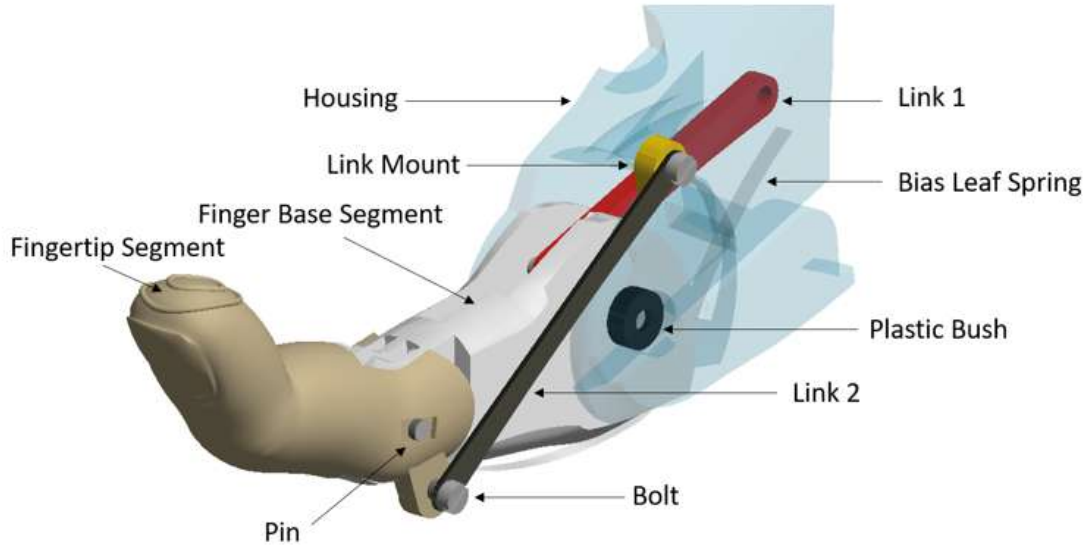


Figure 2.7: Two-link Finger Mechanism Assembly

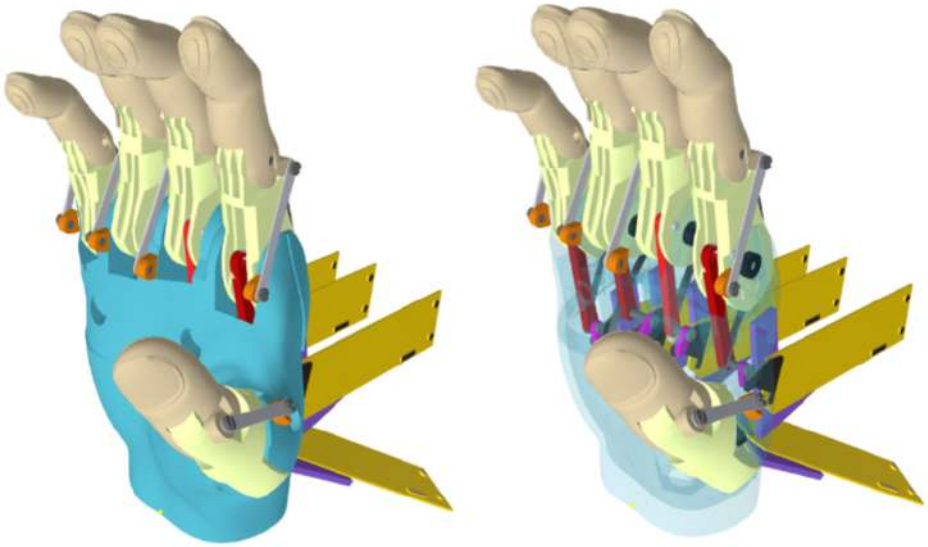


Figure 2.8: Prosthetic Hand Assembly

designed to be semi-closed, limiting its range of motion. This was done to simplify the hand design since replicating the degrees of freedom of the thumb joint is complex. By setting the prosthetic thumb in a semi-closed grip, all six necessary grasps can be performed utilising only one degree of freedom mechanisms.

Bias leaf springs were threaded from the finger bases into the hand housing and held in place by the deflections of the springs. Since this approach was not possible for the prosthetic thumb due to space constraints, a steel hairspring, as shown in Figure 2.10, was used instead. One end of the hairspring was connected to the hand housing while the other was connected

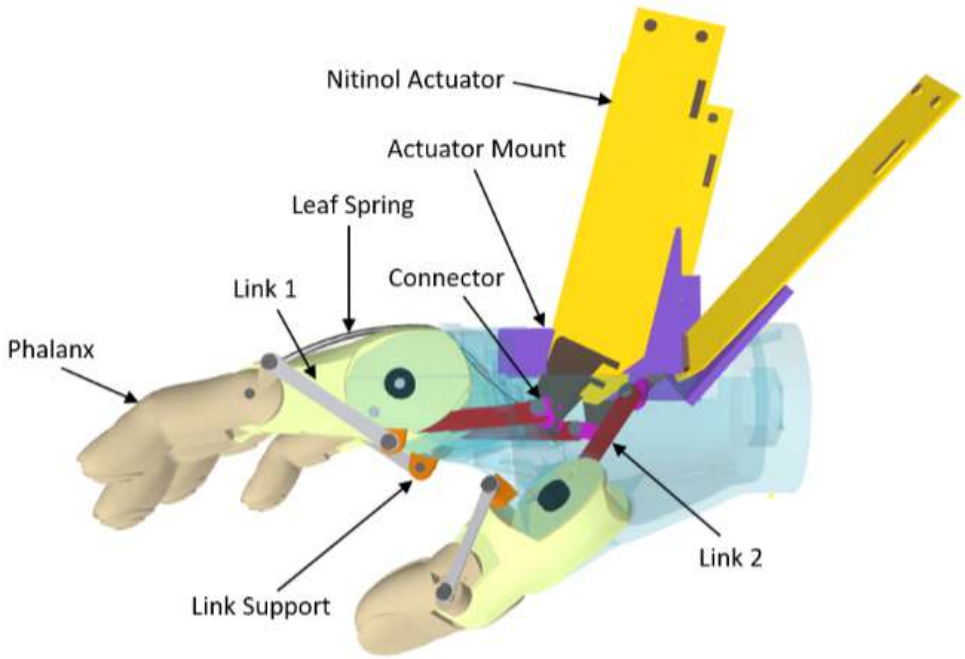


Figure 2.9: Actuation Scheme Configuration

to the prosthetic thumb. When the thumb is pulled inwards, the spring is loaded, providing the necessary bias force to reset the actuator when deactivated.

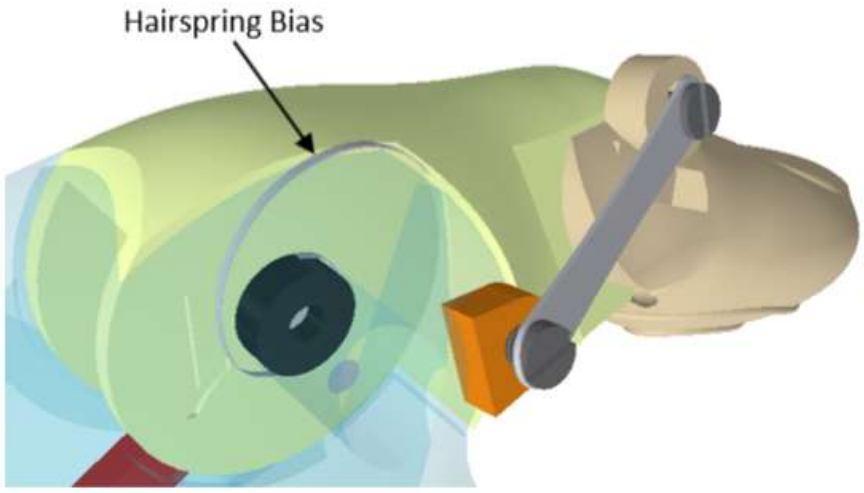


Figure 2.10: Hairspring Bias

3 Analytical Analysis

3.1 Steady-State Fingertip Force Analysis

Link 1 is connected to the finger segment, forming a crank-slider mechanism that translates the linear actuator stroke into a rotation of the finger segment about the MCP joint, as shown in Figure 3.1. The finger segment's angle of rotation about the MCP joint is referred to as the finger angle, depicted as θ_1. Link 2 is connected to the casing and fingertip segment, and is used to constrain the fingertip segment's rotation, resulting in the dependence of the PIP joint's rotation on the MCP joint's rotation. This negates the need for a second actuator to control the PIP rotation, resulting in a mechanism with 1 DOF. The term T_f, represents the bias torque generated by the steel leaf spring, used for assisting the finger return to resting position when the actuator is deactivated.

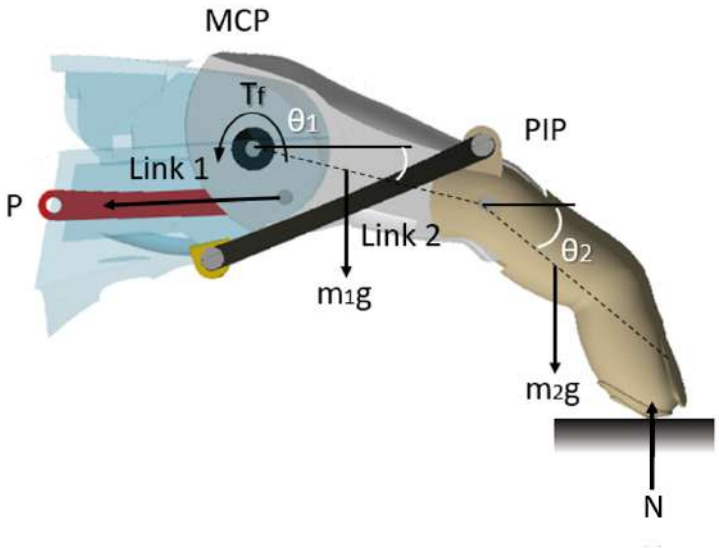


Figure 3.1: Free Body Diagram of Finger Mechanism

The geometric relation between θ_1 and θ_2 was determined within Autodesk Inventor, using constraints to relate the finger geometries. The relationship is expressed by Equation 3.1:

$$\theta_2 = 0.0498\theta_1^2 - 0.1427\theta_1 + 3.1472 \tag{3.1}$$

3.1.1 Torsional Bias

A steel leaf spring is used to impart a torsional bias onto the MCP joint to improve the positioning response during the Nitinol cooling phase. The spring is fixed to the finger

segment's base, a radius, R, away from the MCP joint. As the finger curls inwards, the leaf spring is deflected. As its fixed point is rotated about the MCP joint, the torsional bias about the MCP joint is generated. The bias dampens the system and reduces overshoot, thus minimizing positional oscillation between changing grasps. SAE-AISI 1070 steel was chosen as the material for the leaf spring. The leaf spring was 0.22 mm thick and 5 mm wide.

Table 3.1: Bias Spring Parameters

Parameter	**Symbol**	**Value**
Young's Modulus	E	200 GPa
length	l	105 mm
width	w	5 mm
thickness	t	0.22 mm

The spring is assumed to act as a quarter-elliptic.The stiffness can be calculated by substituting the parameters from Table 3.1 into Equation 3.2 [41]:

$$k = \frac{8Ewt^3}{6l^3} \tag{3.2}$$

$$k = \frac{8(200 \times 10^9)(5)(0.22^3)}{6(105)^3} \tag{3.3}$$

$$k = 1229\ N/mm \tag{3.4}$$

The bias torque can the calculated in terms of the spring deflection, δ:

$$T_f = k\delta R \tag{3.5}$$

Where R is the distance between the leaf spring attachment point and the finger base's point of rotation, the MCP joint.

To relate the bias torque to the finger angle, an equation which relates the spring deflection to the finger angle is used. The following equation was derived using the geometries of the parts in Autodesk Inventor.

$$\delta = 0.0195\theta_1 - 0.39 \tag{3.6}$$

3.1.2 Link 2 Orientation with Respect to the Finger Base Position

Link 2 constrains the rotation of the finger tip to the rotation of the finger base. Therefore, there is a physical relationship between the orientations of the finger base, finger tip and Link 2. As shown in Figure 3.2, the geometric relationship is represented by two triangles. It is assumed that triangles ABC and CDE remain classified as similar, while the finger curls

inwards. Where A is the connection point between Link 2 and the casing, B is the MCP joint, D is the PIP joint, E is the connection point between Link 2 and the fingertip segment, and C is the intersection point between Link 2 and the finger segment's center line. The side lengths S_1 and S_3 can be calculated using lengths L_1 and L_3, and percentage ratio c:c+w, as follows:

$$S_1 = \frac{c}{c+w} L_1 \tag{3.7}$$

$$S_3 = \frac{c}{c+w} L_3 \tag{3.8}$$

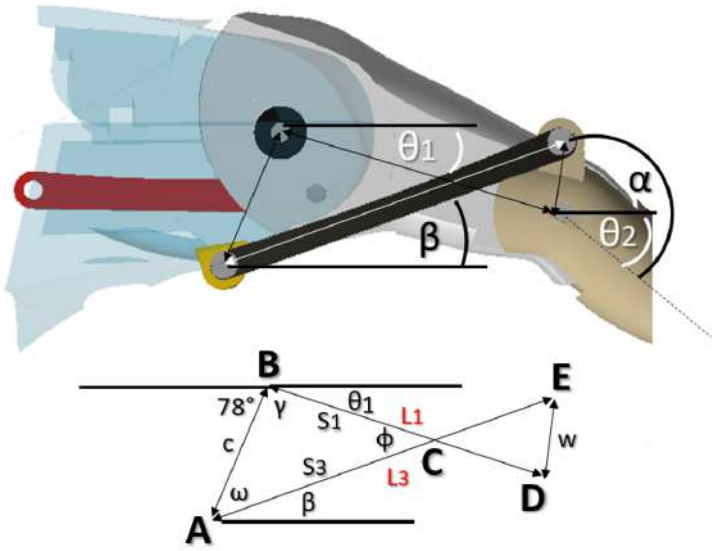


Figure 3.2: Link 2 Orientation with respect to the Finger Base Position Diagram

Once the side lengths are known angle β can be calculated as follows:

$$78 + \gamma + \theta_1 = 180 \tag{3.9}$$

$$\gamma = 102 - \theta_1 \tag{3.10}$$

Using sine rule:

$$\frac{S_3}{\sin\gamma} = \frac{c}{\sin\phi} \tag{3.11}$$

$$\sin\phi = \frac{c}{S_3}\sin\gamma \tag{3.12}$$

It can be deduced that:

$$\phi = \theta_1 + \beta \tag{3.13}$$

Therefore, β can be expressed in terms of θ_1.

$$\sin(\theta_1 + \beta) = \frac{c}{S_3} \sin\gamma \tag{3.14}$$

$$\beta = \arcsin\left(\frac{c}{S_3} \sin(102 - \theta_1)\right) - \theta_1 \tag{3.15}$$

This relates the orientation of Link 2 to the finger angle, θ_1. This is vital for developing the model which calculates the fingertip force exerted onto a flat surface in Section 3.1.3.

3.1.3 Steady-State Fingertip Force Model

To analyze the fingertip strength of the finger during the early design phase, a model which predicts the generated fingertip force was derived. The two-link finger mechanism was simplified into a two dimensional analysis; the finger is constrained to only act in one plane.

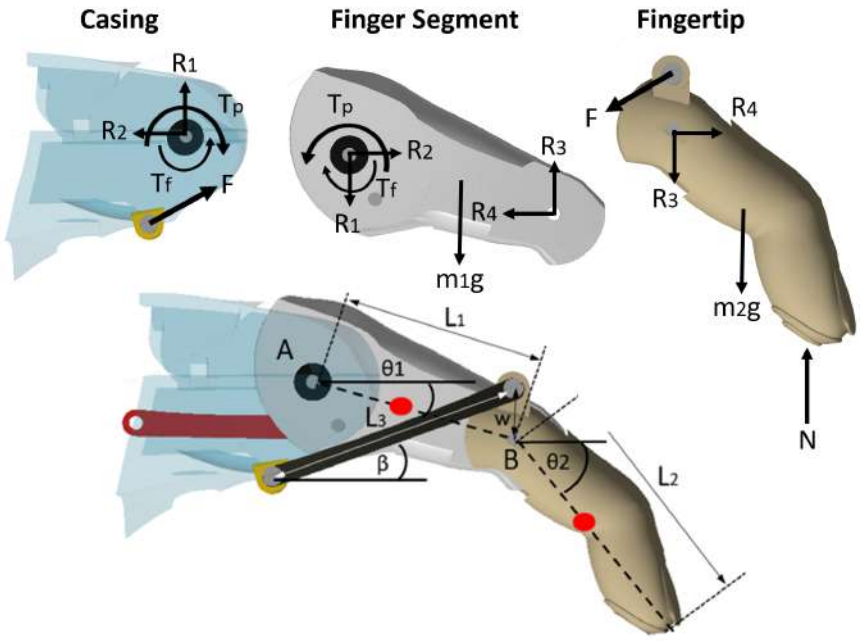


Figure 3.3: Detailed Free Body Diagrams of Finger Mechanism

Frictionless pin joints are assumed to connect the finger mechanism. This assumption is reasonable due to the small surface area of the joints as well as the added lubrication. The actuation force can be simplified into an applied torque on the MCP joint. Similarly, the bias leaf spring force is assumed to impart a torsional load on the MCP joint as the finger curls inwards, the derivation of the bias torque is described in Section 3.1.1.

From the prosthetic casing:

$$\sum F_y = 0$$

$$R_1 = F \sin \beta \tag{3.16}$$

$$\sum F_x = 0$$

$$R_2 = -F \cos \beta \tag{3.17}$$

From the finger segment:

$$\sum F_y = 0$$

$$R_1 = m_1 g + R_3 \tag{3.18}$$

$$\sum F_x = 0$$

$$R_2 + R_4 = 0 \tag{3.19}$$

$$\sum M_A = 0$$

$$T_p - T_f + m_1 g 0.327 L \cos \theta_1 + R_3 L \cos \theta_1 + R_4 L \sin \theta_1 = 0 \tag{3.20}$$

From the fingertip segment:

$$\sum F_y = 0$$

$$R_3 = N + F \sin \beta - m_2 g \tag{3.21}$$

$$\sum F_x = 0$$

$$R_4 = F \cos \beta \tag{3.22}$$

$$\sum M_B = 0$$

$$N L_2 \cos \theta_2 - m_2 g 0.473 L_2 - F \cos \beta w \sin(\alpha - \theta_2) + F \sin \beta w \cos(\alpha - \theta_2) = 0 \tag{3.23}$$

$$N L_2 \cos \theta_2 - m_2 g 0.473 L_2 - F[\cos \beta w \sin(\alpha - \theta_2) - \sin \beta w \cos(\alpha - \theta_2)] = 0 \tag{3.24}$$

$$F = \frac{N L_2 \cos \theta_2 - m_2 g 0.473 L_2}{\cos \beta w \sin(\alpha - \theta_2) - \sin \beta w \cos(\alpha - \theta_2)} \tag{3.25}$$

Which simplifies to:

$$F = \frac{N L_2 \cos \theta_2 - m_2 g 0.473 L_2}{w \sin(\alpha - \theta_2 + \beta)} \tag{3.26}$$

Let:

$$D = \frac{1}{w \sin(\alpha - \theta_2 + \beta)} \tag{3.27}$$

$$E = m_2 g 0.473 L_2 \tag{3.28}$$

$$F = DEL_2 \cos\theta_2 - AB \tag{3.29}$$

Substitute Equations 3.21 and 3.22 into Equation 3.20:

$$T_p - T_f + m_1 g 0.327L \cos\theta_1 + (N + F\sin\beta - m_2 g)L_1 \cos\theta_1 + (F\cos\beta)L_1 \sin\theta_1 = 0 \tag{3.30}$$

$$T_p - T_f + m_1 g 0.327L \cos\theta_1 + (N - m_2 g)L_1 \cos\theta_1 + FL_1 \sin(\beta + \theta_1) = 0 \tag{3.31}$$

Let:

$$C = m_1 g 0.327L \cos\theta_1 - m_2 g L_1 \cos\theta_1 \tag{3.32}$$

Substitute Equations 3.29 and 3.32 into Equation 3.31:

$$T_p - T_f + C + NL_1 \cos\theta_1 + (DNL_2 \cos\theta_2 - DE)L_1 \sin(\beta + \theta_1) = 0 \tag{3.33}$$

$$T_p - T_f + C + N(L_1 \cos\theta_1 + AL_2 \cos\theta_2 L_1 \sin(\beta + \theta_1)) - DEL_1 \sin(\beta + \theta_1) = 0 \tag{3.34}$$

Therefore:

$$N = \frac{DEL_1 \sin(\beta + \theta_1) + T_f - T_p - C}{L_1 \cos\theta_1 + DL_2 \cos\theta_2 L_1 \sin(\beta + \theta_1)} \tag{3.35}$$

3.1.4 Fingertip Force vs PIP Angle

The following analysis examines the effect of the PIP joint's orientation on the fingertip force. This is vital to determine the prosthetic finger's ability to manipulate objects and perform tasks which require fine motor skills. The middle finger was chosen and its dimensions used in the analytical model developed in Section 3.1.3. The analytical results are illustrated in Figure 3.4.

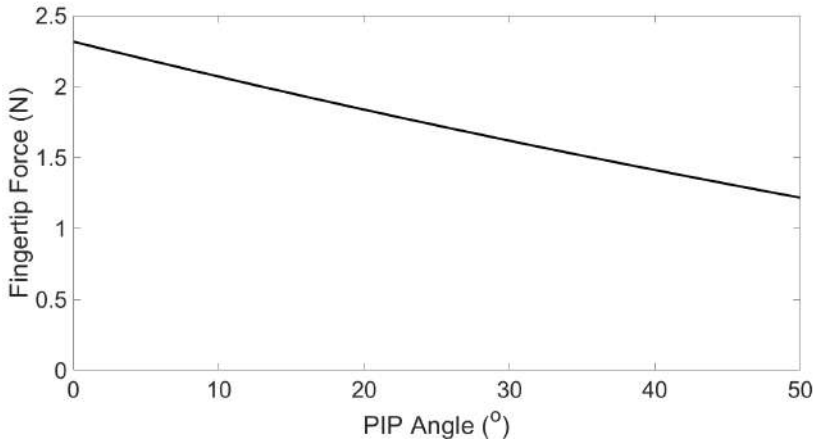


Figure 3.4: Fingertip Force vs PIP angle for Middle Prosthetic Finger

It can be seen that as the PIP angle increases (finger curls inwards) the fingertip force decreases. This is due to the bias moment generated by the leaf spring, which increases as the finger curls inwards. The analysis predicts a fingertip force range of 1.27-2.46 N. These values are comparable to past low-cost 3D printed hands which performed dexterous tasks such as playing the violin with an operational fingertip force range of 1.1-2.8 N [42].

3.2 Bang-Bang Controlled Finger Trajectory Analysis

3.2.1 Nitinol Wire Heat Transfer (Electro-Thermal) Model

The following transient model determines the wire temperature based on the electrical power input. The transient heat transfer model assumes that the diameter length of the wire is small compared to its total length; therefore the temperature distribution is uniform throughout the wire cross-section, and the wire length is infinitely long. The dominant energy contributions in the heat transfer model are illustrated in Figure 3.5.

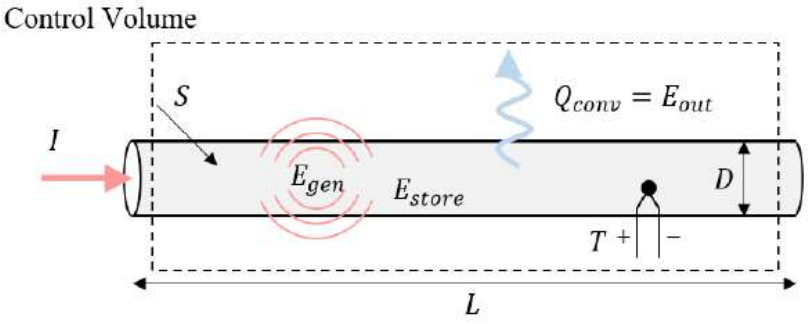


Figure 3.5: Dominant Energy Contributions [43]

The energy balance of the control volume can be mathematically represented by the following equation [43]:

$$E_{in} + E_{gen} = E_{out} + E_{stored} \tag{3.36}$$

Where, E_{in} represents the energy imparted to the system due to the axial loading, given by the following equation and discussed in Section 1.2.5.3.

$$E_{in} = \dot{W}_{mech} = \frac{1}{\rho}\sigma\Delta\varepsilon_{tr} \tag{3.37}$$

Where, σ is the axial stress load on the wire:

$$\sigma = \frac{(T_f - \tau_1)}{bA_{wire}} \tag{3.38}$$

Where T_f and τ_1 are described in Sections 3.1.1 and 3.2.3, respectively. While A_{wire} is the wire's cross-sectional area, and b is the displacement between the MCP joint and Link 1 joint to the finger base.

E_{gen} represents the heat generated by the ohmically heating of the Nitinol wire:

$$E_{gen} = IV \tag{3.39}$$

Where, I and V represent the input current and voltage, respectively. Since PWM is used to prevent wire overheating, the current is not constant. A *cos* function is used to represent the PWM signal since it is assumed that at a high frequency (Fc), a *cos* function adequately simulates the shape of a PWM input.

$$I = cos(2\pi Fct) + 1 \tag{3.40}$$

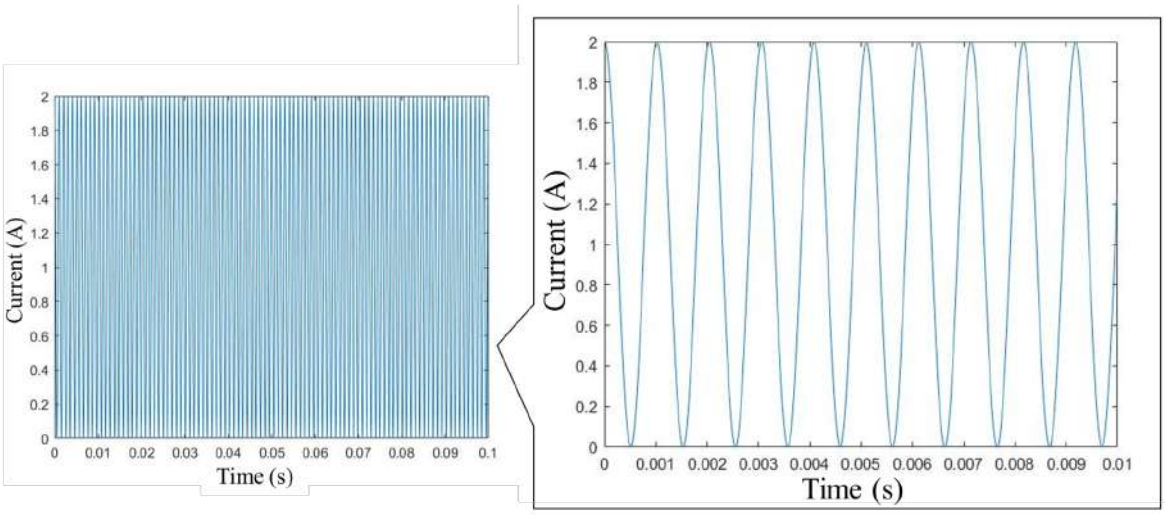


Figure 3.6: Input Current Signal with a 980 Hz PWM Frequency

E_{out} is the heat lost due to natural convection given by Equation 3.41:

$$E_{out} = hS(T_\infty - T) + \cancelto{0}{\dot{Q}_{cond}} + \cancelto{0}{\dot{Q}_{rad}} \tag{3.41}$$

Where, T is the wire's temperature, $T\infty$ is the ambient temperature, h is the convective coefficient, and S is the surface area of the wire.

E_{stored} is equal to the latent heat of the Nitinol wire and the heat generated due the Nitinol phase shifting, as shown in Equation 3.42:

$$E_{stored} = mc\frac{dT}{dt} - m\Delta H\frac{d\xi}{dt} \tag{3.42}$$

Where $\frac{d\xi}{dt}$ represents the rate of change in the martensite fraction. As discussed in Section 1.2.5.2, there are two different equations used to determine ξ for the heating and cooling phases:

$$\xi_h = \frac{1}{2}\left[1 - \cos\left(\pi \frac{T - A_s}{A_f - A_s}\right)\right] \tag{3.43}$$

$$\xi_c = \frac{1}{2}\left[1 + \cos\left(\pi \frac{T - M_f}{M_s - M_f}\right)\right] \tag{3.44}$$

$$\frac{d\xi_h}{dt} = \frac{\pi}{2(A_f - A_s)}\left[\sin\left(\pi \frac{T - A_s}{A_f - A_s}\right)\right]\frac{dT}{dt}, A_s < T < A_f \tag{3.45}$$

$$\frac{d\xi_c}{dt} = \frac{\pi}{2(M_s - M_f)}\left[\sin\left(\pi \frac{T - M_f}{M_s - M_f}\right)\right]\frac{dT}{dt}, M_f < T < M_s \tag{3.46}$$

When temperature, T, falls out of the transition zone temperatures, $\frac{d\xi}{dt} = 0$. Therefore, Equation 3.36 becomes:

$$\dot{W}_{mech} + IV = hS(T_\infty - T) + mc\frac{dT}{dt} - m\Delta H\frac{d\xi}{dt} \tag{3.47}$$

For heating, A_s<T<A_f:

$$\dot{W}_{mech} + IV = hS(T_\infty - T) + mc\frac{dT}{dt} - m\Delta H\frac{d\xi_h}{dt} \tag{3.48}$$

$$\dot{W}_{mech} + IV = hS(T_\infty - T) + mc\frac{dT}{dt} - m\Delta H\frac{\pi}{2(A_f - A_s)}\left[\sin\left(\pi \frac{T - A_s}{A_f - A_s}\right)\right]\frac{dT}{dt} \tag{3.49}$$

$$\dot{W}_{mech} + IV - hS(T_\infty - T) = \left(mc - m\Delta H\frac{\pi}{2(A_f - A_s)}\left[\sin\left(\pi \frac{T - A_s}{A_f - A_s}\right)\right]\right)\frac{dT}{dt} \tag{3.50}$$

$$\frac{dT}{dt} = \frac{\dot{W}_{mech} + IV - hS(T_\infty - T)}{\left(mc - m\Delta H\frac{\pi}{2(A_f - A_s)}\left[\sin\left(\pi \frac{T - A_s}{A_f - A_s}\right)\right]\right)} \tag{3.51}$$

For heating, A_s>T and T<A_f:

$$\frac{dT}{dt} = \frac{\dot{W}_{mech} + IV - hS(T_\infty - T)}{mc} \tag{3.52}$$

For cooling, M_f<T<M_s:

$$\dot{W}_{mech} + \cancelto{0}{\dot{W}} = hS(T_\infty - T) + mc\frac{dT}{dt} - m\Delta H\frac{d\xi_c}{dt} \tag{3.53}$$

$$\dot{W}_{mech} = hS(T_\infty - T) + mc\frac{dT}{dt} - m\Delta H\frac{\pi}{2(M_s - M_f)}\left[\sin\left(\pi\frac{T - M_f}{M_s - M_f}\right)\right]\frac{dT}{dt} \tag{3.54}$$

$$\dot{W}_{mech} - hS(T_\infty - T) = \left(mc - m\Delta H\frac{\pi}{2(M_s - M_f)}\left[\sin\left(\pi\frac{T - M_f}{M_s - M_f}\right)\right]\right)\frac{dT}{dt} \tag{3.55}$$

$$\frac{dT}{dt} = \frac{\dot{W}_{mech} - hS(T_\infty - T)}{\left(mc - m\Delta H\frac{\pi}{2(M_s - M_f)}\left[\sin\left(\pi\frac{T - M_f}{M_s - M_f}\right)\right]\right)} \tag{3.56}$$

For cooling, M_f>T and T>M_s:

$$\frac{dT}{dt} = \frac{\dot{W}_{mech} - hS(T_\infty - T)}{mc} \tag{3.57}$$

3.2.2 Finger Angle Displacement Based on Actuator Displacement Model

The following model predicts the actuator displacement based on the temperature of the Nitinol wire. The actuator displacement is then transformed geometrically into the finger angle. The actuator displacement is dependent on the strain of the Nitinol wire caused by the change in wire temperature, which was modelled in Section 3.2.1. As discussed in Section 1.2.5.1, the strain can be expressed in terms of temperature change for both the heating and cooling phases with Equations 3.58 and 3.59, where k_f and k_r are constants with values 6.56 MPa/°C and 7.09 MPa/°C, respectively:

For heating:

$$\varepsilon = \frac{278.92 + k_f(T - T_0)}{E} \tag{3.58}$$

For cooling:

$$\varepsilon = \frac{123.17 + k_r(T - T_0)}{E} \tag{3.59}$$

Where, ε is the wire's strain, T_0 is the previous wire temperature, and E is the Young's Modulus of the Nitinol wire.

Young's Modulus, E, for the wire is dependent on martensite fraction:

$$E = \frac{1}{2}(E_A + \xi(E_M - E_A)) \tag{3.60}$$

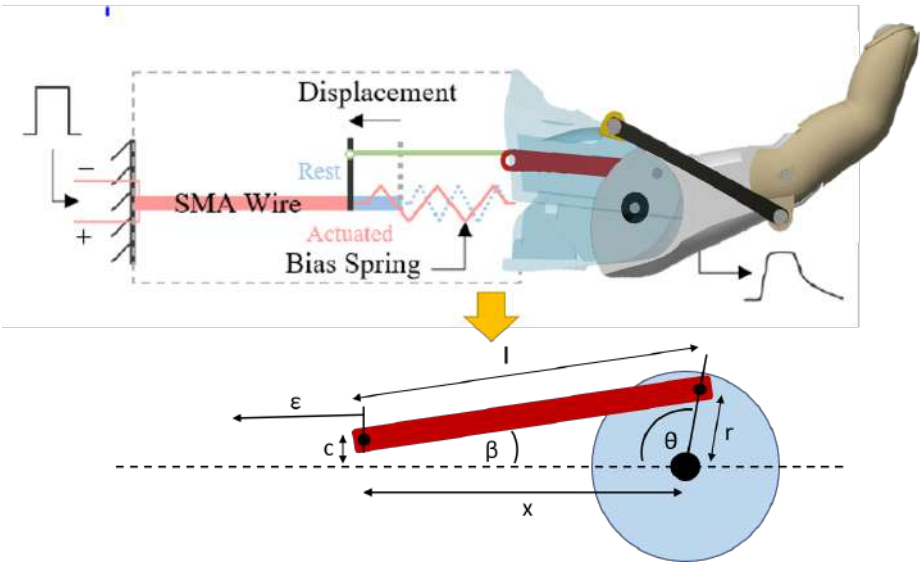


Figure 3.7: Crank-Slider Mechanism [43]

Where, E_A is the Young's Modulus for the austenite phase, and E_M is the Young's Modulus for the martensite phase.

The strain of the wire is what drives the finger in a crank-slider mechanism, which transforms the linear displacement into an angular one, as illustrated in Figure 3.7.

$$\varepsilon + x = r\cos\theta - l\cos\beta \tag{3.61}$$

Where,

$$\beta = \pi - \arcsin\left(\frac{r\sin\theta - c}{l}\right) \tag{3.62}$$

This relation can be simplified further due to length c being less than 10 times lengths l and x. Using the side-angle-side triangle rule the equation becomes:

$$(\varepsilon + x)^2 = l^2 + r^2 + 2r(\varepsilon + x)\cos\theta \tag{3.63}$$

$$\theta = \arccos\left(\frac{(\varepsilon + x)^2 - l^2 - r^2}{2r(\varepsilon + x)}\right) \tag{3.64}$$

3.2.3 Kinematic Finger Model

The Lagrangian method is used to derive the dynamic modelling of the finger. The finger mechanism can be simplified into a linkage system with 1 degree of freedom, since θ_2 is dependent on θ_1. The finger links are simplified into two rods of lengths l_1 and l_2 which are joined together by a pin, as shown in Figure 3.8. An actuation torque, τ_1, generated by a Nitinol actuator acts on link 1 in an anticlockwise direction. A detailed derivation is shown in Appendix C.1.

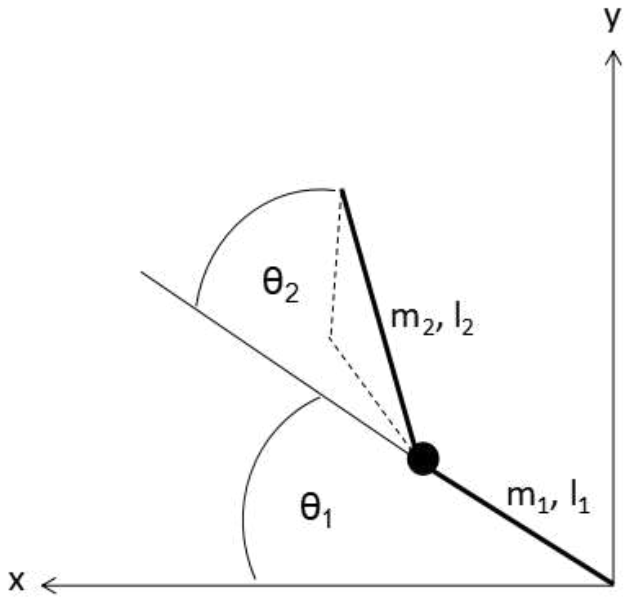


Figure 3.8: Simplified Link Diagram of Finger Mechanism

The angular displacement θ_2 is dependent on the finger angle defined as θ_1 due to Link 2. An equation that expresses θ_2 in terms of θ_1 was derived using geometric models in Autodesk Inventor.

$$\theta_2 = 0.0498\theta_1^2 - 0.1427\theta_1 + 3.1472 \tag{3.65}$$

Therefore:

$$\dot{\theta}_2 = 0.0996\theta_1\dot{\theta}_1 - 0.1427\dot{\theta}_1 \tag{3.66}$$

$$\ddot{\theta}_2 = 0.0996\dot{\theta}_1^2 + 0.0996\theta_1\ddot{\theta}_1 - 0.1427\ddot{\theta}_1 \tag{3.67}$$

By using the trigonometric method and Euler Lagrange formula, the linear velocity of mass center of the finger:

$$\dot{x_1} = -\frac{1}{2} l_1 \sin\theta_1 \dot{\theta_1} \tag{3.68}$$

$$\dot{y_1} = \frac{1}{2} l_1 \cos\theta_1 \dot{\theta_1} \tag{3.69}$$

$$\dot{x_2} = -l_1 \sin\theta_1 \dot{\theta_1} - \frac{1}{2} l_2 \sin(\theta_1 + \theta_2)(\dot{\theta_1} + \dot{\theta_2}) \tag{3.70}$$

$$\dot{y_2} = l_1 \cos\theta_1 \dot{\theta_1} + \frac{1}{2} l_2 \cos(\theta_1 + \theta_2)(\dot{\theta_1} + \dot{\theta_2}) \tag{3.71}$$

The equations for the linear velocities are the square and sum of the Equations 3.68, 3.69, 3.70 and 3.71 to find v_1 and v_2:

$$v^2 = \dot{x}^2 + \dot{y}^2 \tag{3.72}$$

$$v_1^2 = \dot{x}_1^2 + \dot{y}_1^2 \tag{3.73}$$

$$v_1^2 = (\frac{1}{2} l_1 \cos\theta_1 \dot{\theta_1})^2 + (-\frac{1}{2} l_1 \sin\theta_1 \dot{\theta_1})^2 \tag{3.74}$$

$$v_1^2 = \frac{1}{4} l_1^2 \dot{\theta_1}^2 \tag{3.75}$$

$$v_2^2 = \dot{x}_2^2 + \dot{y}_2^2 \tag{3.76}$$

$$\begin{aligned} v_2^2 = \dot{(} l_1 \cos\theta_1 \dot{\theta_1} + \frac{1}{2} l_2 \cos(\theta_1 + \theta_2)(\dot{\theta_1} + \dot{\theta_2}))^2 \\ +(-l_1 \sin\theta_1 \dot{\theta_1} - \frac{1}{2} l_2 \sin(\theta_1 + \theta_2)(\dot{\theta_1} + \dot{\theta_2}))^2 \end{aligned} \tag{3.77}$$

$$v_2^2 = l_1^2 \dot{\theta_1}^2 + \frac{1}{4}(\dot{\theta_1^2} + 2\dot{\theta_1}\dot{\theta_2} + \dot{\theta_2^2}) + l_1 l_2 cos(\theta_2)(\dot{\theta_1^2} + \dot{\theta_1}\dot{\theta_2}) \tag{3.78}$$

The lagrangian is calculated as:

$$L = T - V \tag{3.79}$$

Therefore:

$$\begin{aligned} L = \frac{1}{2}(\frac{1}{4} m_1 + m_2)(l_1^2 \dot{\theta_1}^2) + \frac{1}{2} m_2 (\frac{1}{4}(\dot{\theta_1^2} + 2\dot{\theta_1}\dot{\theta_2} + \dot{\theta_2^2}) + l_1 l_2 cos(\theta_2)(\dot{\theta_1^2} + \dot{\theta_1}\dot{\theta_2})) \\ -(\frac{1}{2} m_1 + m_2)(g l_1 \sin\theta_1) - m_2(\frac{1}{2} g l_2 \sin(\theta_1 + \theta_2)) \end{aligned} \tag{3.80}$$

The equations of motion are derived from the lagrangian as follows:

$$\frac{d}{dt}(\frac{\partial L}{\partial \dot{\theta}}) - \frac{\partial L}{\partial \theta} = \tau \tag{3.81}$$

For θ_1 (finger angle),

$$\frac{d}{dt}(\frac{\partial L}{\partial \dot{\theta_1}}) - \frac{\partial L}{\partial \theta_1} = \tau_1 \tag{3.82}$$

$$\frac{\partial L}{\partial \theta_1} = -(\frac{1}{2} m_1 + m_2)(g l_1 \cos(\theta_1)) - m_2(\frac{1}{2} g l_2 \cos(\theta_1 + \theta_2)) \tag{3.83}$$

$$\frac{\partial L}{\partial \dot{\theta}_1} = (\frac{1}{4}m_1 + m_2)(l_1^2\dot{\theta}) + \frac{1}{2}m_2\left[\frac{1}{4}(2\dot{\theta}_1 + 2\dot{\theta}_2) + l_1 l_2\cos(\theta_2)(2\dot{\theta}_1 + \dot{\theta}_2)\right] \tag{3.84}$$

$$\frac{d}{dt}(\frac{\partial L}{\partial \dot{\theta}_1}) = (\frac{1}{4}m_1 + m_2)(l_1^2\ddot{\theta}) + \frac{1}{2}m_2\left[\frac{1}{4}(2\ddot{\theta}_1 + 2\ddot{\theta}_2) + l_1 l_2\cos(\theta_2)(2\ddot{\theta}_1 + \ddot{\theta}_2) - l_1 l_2\sin(\theta_2)(2\dot{\theta}_1 + \dot{\theta}_2)\right] \tag{3.85}$$

Therefore:

$$(\frac{1}{4}m_1 + m_2)(l_1^2\ddot{\theta}) + \frac{1}{2}m_2\left[\frac{1}{4}(2\ddot{\theta}_1 + 2\ddot{\theta}_2) + l_1 l_2\cos(\theta_2)(2\ddot{\theta}_1 + \ddot{\theta}_2) - l_1 l_2\sin(\theta_2)(2\dot{\theta}_1 + \dot{\theta}_2)\right] + (\frac{1}{2}m_1 + m_2)(g l_1\cos(\theta_1)) + m_2(\frac{1}{2}g l_2\cos(\theta_1 + \theta_2)) = \tau_1 \tag{3.86}$$

3.2.4 Bang-Bang Controller Architecture for Nitinol-Driven Finger

Bang-bang control is used to control the trajectory of the finger to fit the desired path. When the finger angle is less than the desired angle, the actuator is activated, and the Nitinol wire is heated. Conversely, when the finger angle is greater than the desired angle, the actuator is deactivated, and the Nitinol wire cools down.

A detailed flowchart of the Matlab code used to simulate the controller and trajectory model is illustrated in Figure 3.9. The Matlab code for the bang-bang controlled Nitinol-driven finger with a step input desired path is presented in Appendix A.1.

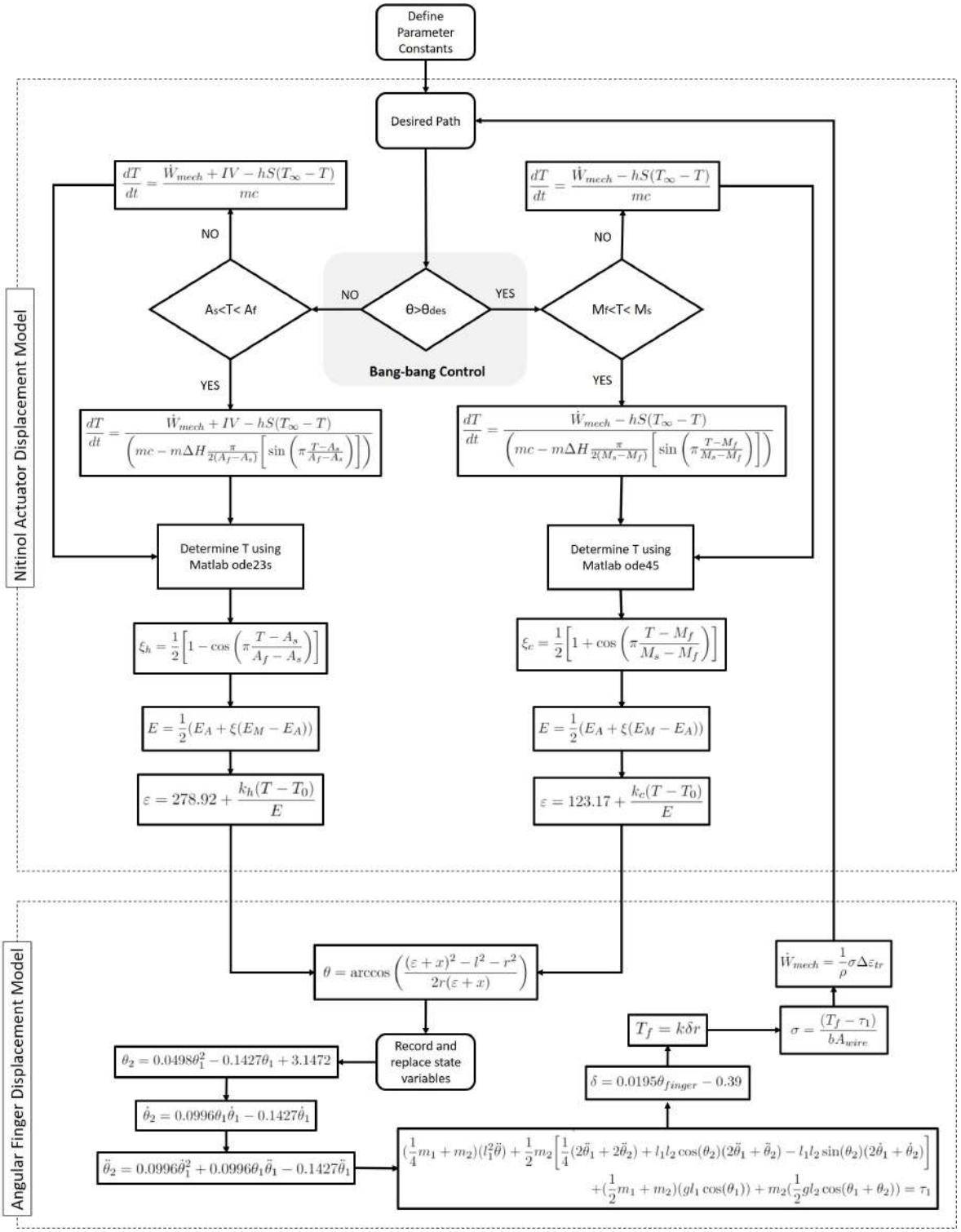


Figure 3.9: Matlab Code Architecture for Bang-Bang Controlled Nitinol-Driven Finger

3.2.5 Step Response Analysis

A square step signal was used to examine the system's response time for both the heating and cooling periods of the Nitinol actuated finger. The middle finger was chosen, and its parameters used in the model developed in Section 3.2.2. The finger's mechanical parameters are shown in Table 3.2. According to the CAD model, the range of motion of the finger base angle was found to be between 20° and 60°. Therefore, the step signal excites the system from a starting position of 30° to an amplitude of 50°, before dropping back down to 30°. This is the same step signal used to test the Nitinol powered hand created by the University of Marmara, which will allow for a direct comparison.

Table 3.2: Middle Finger Parameters

Parameter	**Symbol**	**Value**
Finger Base Length	L_1	0.083 m
Finger Base Mass	m_1	0.018 kg
Finger Segment Length	L_2	0.079 m
Finger Segment Mass	m_2	0.0084 kg
Initial Finger Base Angle	θ_1	20°
Initial PIP Angle	θ_2	$0.0498\theta_1^2$-$0.1427\theta_1$+3.1472

Input voltages between 6 V and 13 V were tested to determine its effect on the system's response time. The sampling frequency was also varied between 20 Hz and 500 Hz to examine its effect on the system's response time and the effective heating of the Nitinol wire. The square step responses are shown in Figures 3.10-3.17.

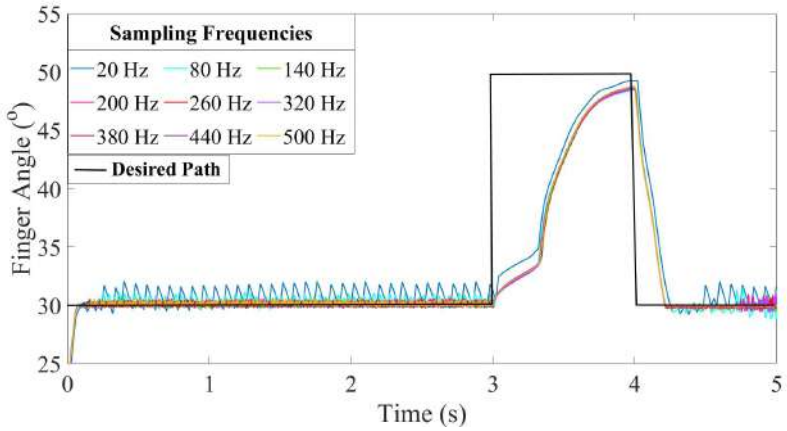


Figure 3.10: Step Signal with 6 V Input Voltage

It was deduced that an input voltage less than 9 V generated a sluggish heating period response. The sluggish response is due to input voltage not overcoming the environmental factor of convective cooling, which is amplified due to PWM. Compared to a continuous input

signal without PWM, the input voltage is pulsed to prevent overheating. This decreases the effective heating of the wire since less energy is supplied to the system compared to a continuous voltage. As illustrated in Figures 3.13 to 3.17, this problem is reduced for larger input voltages.

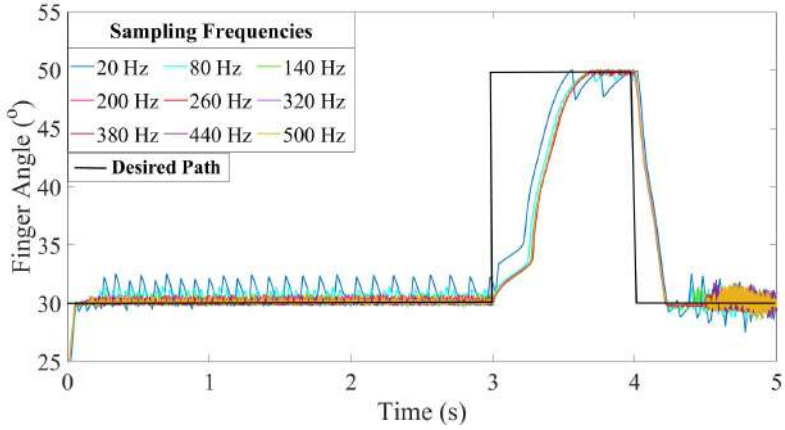


Figure 3.11: Step Signal with 7 V Input Voltage

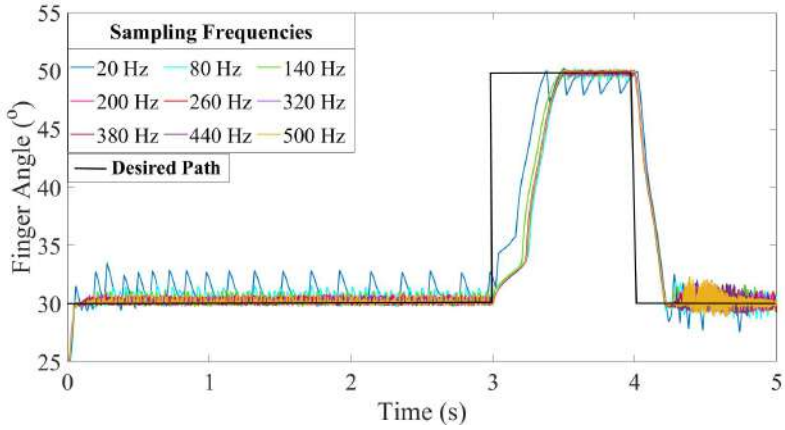


Figure 3.12: Step Signal with 8 V Input Voltage

The two factors which determined the path tracking the performance of the prosthetic finger are the input voltage and sampling frequency. The input voltage determines the activation time (response time) of the Nitinol wire, and the sampling frequency determines the system's positional awareness.

A higher sampling frequency increases the controller's resolution of the finger orientation, increasing the sensitivity to positional change. This is demonstrated by the smallest sampling frequency of 20 Hz, which resulted in the largest overshoot for all cases. An increase in sampling frequency improved the system's response to overshoot, dampening the system by decreasing the heating periods. The full effect of increasing the sampling frequency is

illustrated in Figure 3.18 (The results for a 6 V input voltage were not included due to the system failing to complete the step-up signal).

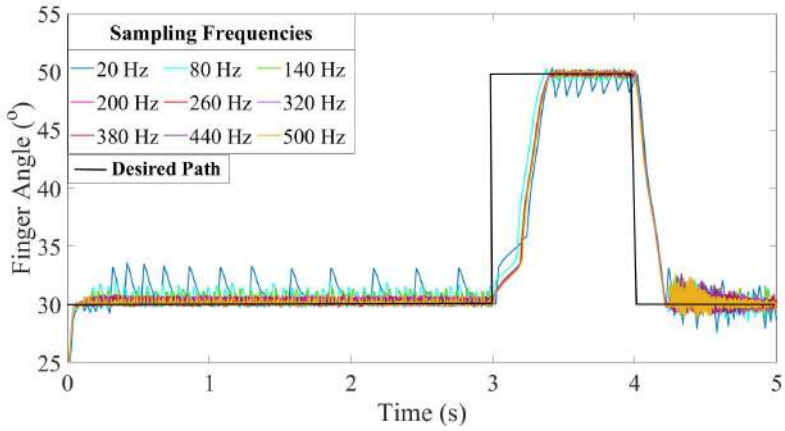


Figure 3.13: Step Signal with 9 V Input Voltage

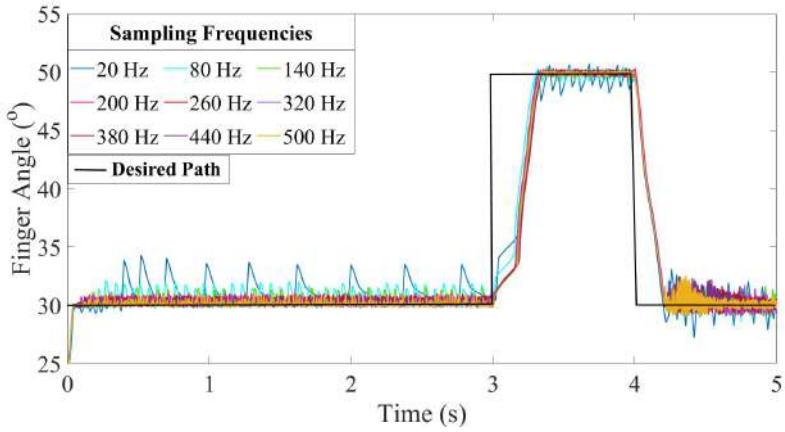


Figure 3.14: Step Signal with 10 V Input Voltage

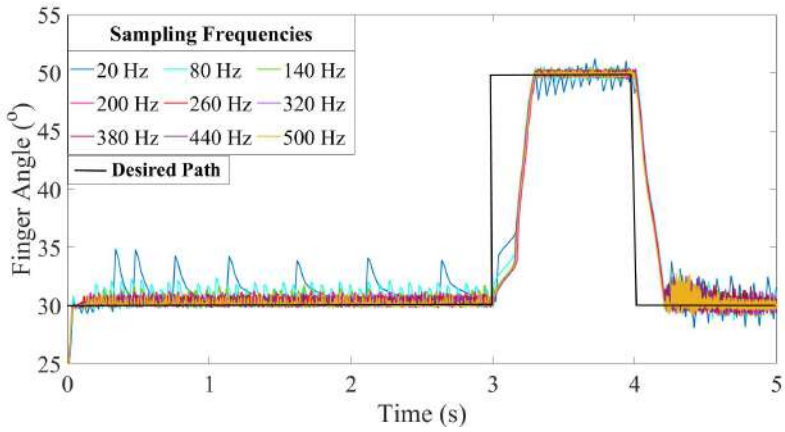


Figure 3.15: Step Signal with 11 V Input Voltage

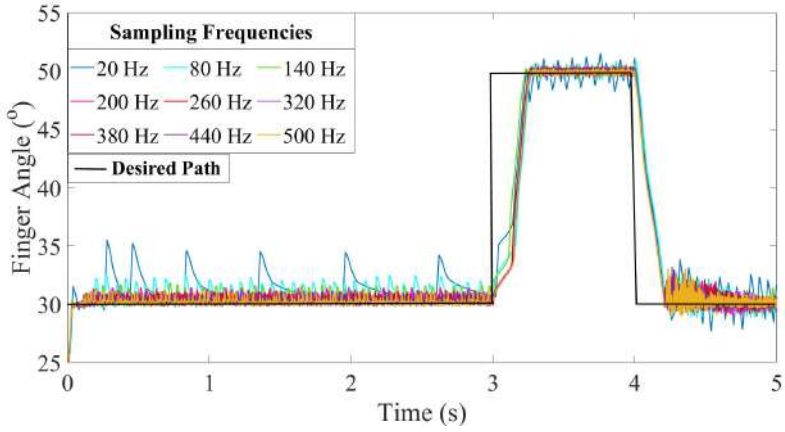


Figure 3.16: Step Signal with 12 V Input Voltage

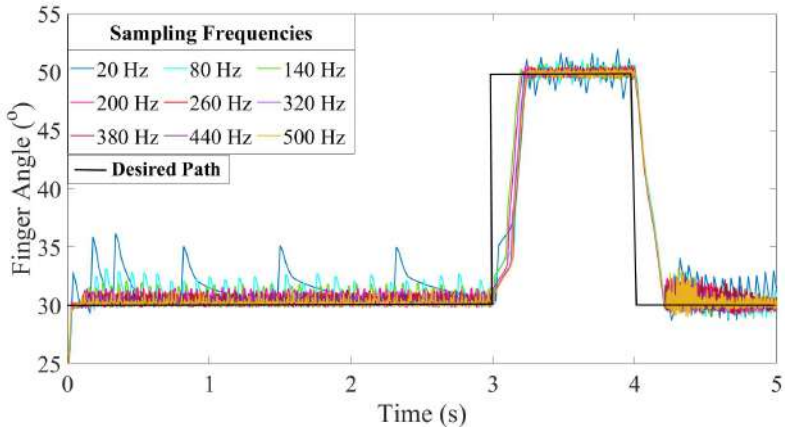


Figure 3.17: Step Signal with 13 V Input Voltage

For smaller input voltages, the change in sampling frequencies has a greater effect on T_h values, since the smaller input voltages require larger heating periods due to having slower activation times. As the input voltage increases, the effect diminishes due to faster activation times requiring smaller heating periods. At 9 V, the input voltage is high enough to compensate for the shorter heating periods with a 200 Hz sampling frequency, while this point is reached at 11 V for a 500 Hz sampling frequency.

The input voltage and sampling frequency does not affect the step-down response, as illustrated in Figure 3.19, since a different actuation method is working. The minor variance in T_c values is caused by response overshoots before the step-down signal, resulting in slightly different starting positions at 4 s. During the step-down response, the wire cools to decrease the finger angle, as the finger uncurls, and the actuator deactivates during the step-down response. Thus, the step-down response is dependent on the convective cooling rate of the Nitinol wire and the bias force generated by the leaf spring, which is the same for all cases.

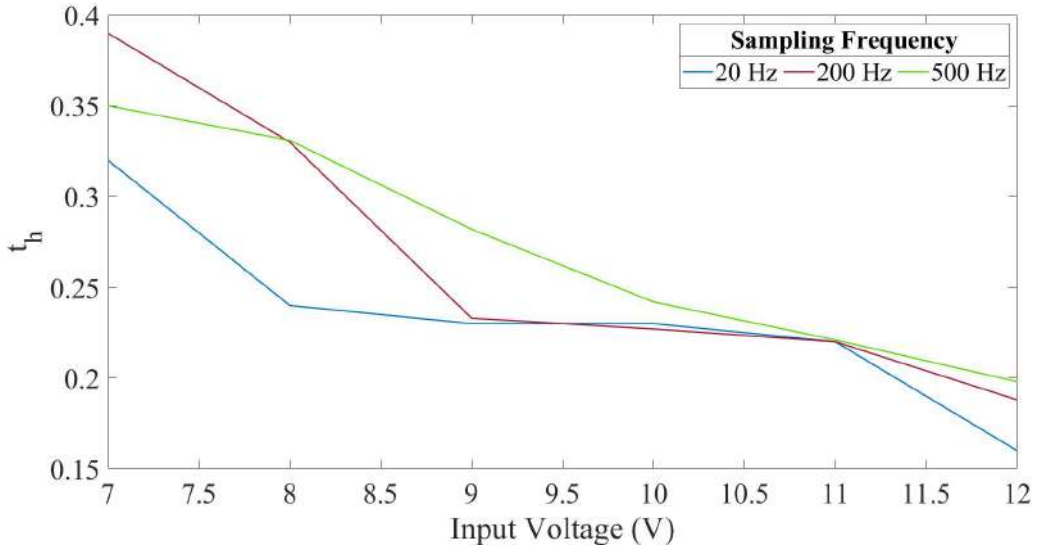


Figure 3.18: Time Constant (Heating) vs. Input Voltage

The analytical results yielded T_h values between 0.17 s and 0.39 s and T_c values between 0.14 s and 0.13 s. This outperformed the past Nitinol powered hand created by the University of Marmara, which utilised a tendon-driven system and yielded a T_h of 0.4 s and a T_c of 1 s for the same step up and step down signals. It can therefore be seen that the proposed link-based Nitinol actuator arrangement has better response time performance compared to the traditional tendon-driven arrangement.

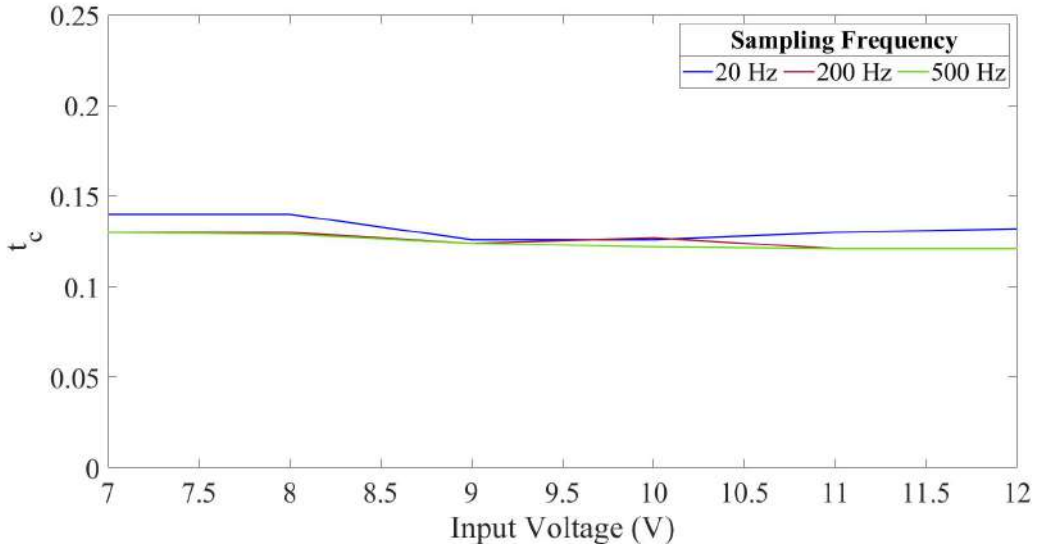


Figure 3.19: Time Constant (Cooling) vs. Input Voltage

4 Prosthetic Hand Fabrication

4.1 Additive Manufacturing

Additive manufacturing, also known as 3D printing, is defined as the process of joining material (usually in layers) to form an object from 3D model data. The object begins to form as consecutive layers are laid on the build plate. These layers are cross-sections of the 3D model that form geometric paths for the 3D printer to follow. The trajectory of the printer nozzle is generated with specialised software such as Cura which translates the desired coordinates into g-code for the nozzle to follow. This process is known as slicing and is shown in Figure 4.1.

Within the software, other variables such as the density (infill percentage), printing temperature, printing speed, layer height and support structures can be controlled. Depending on these variables, the quality and strength of the printed object can largely vary. PLA is the material of choice due to its low cost and minimal warping during printing. The printing parameters for the hand parts are tabulated in Table 4.1.

Table 4.1: PLA Printing Parameters for Prosthetic Hand Parts

Parameter	**Specification**
Layer Height	0.15 mm
Infill Density	35%
Printing Temperature	215 °C
Build Plate Temperature	55 °C
Printing Speed	50 m/s
Plate Adhesion	brim or raft

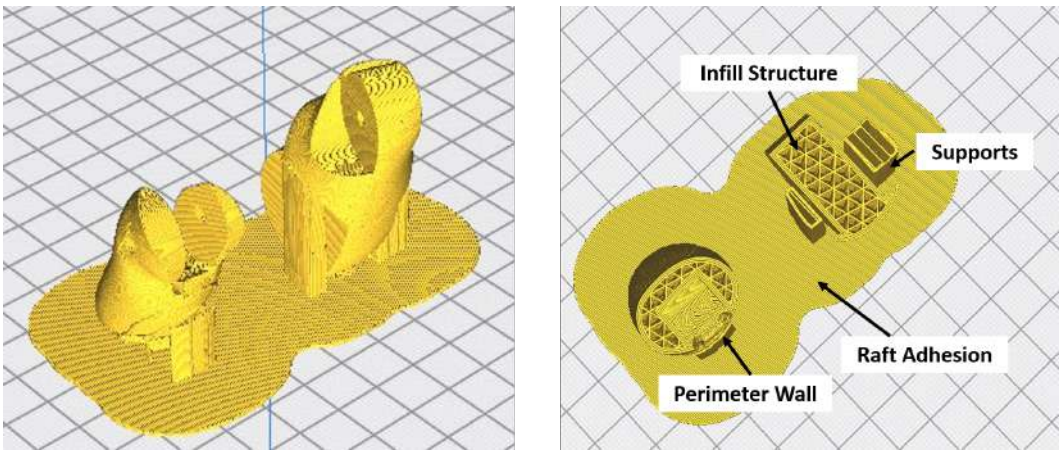


Figure 4.1: Sliced 3D Model for 3D Printing

The major advantage of using 3D printing is rapid prototyping, which allows for quicker progression during the design phase. The final prototype of the prosthetic hand is displayed in Figure 4.2. As can be seen, the 3D printed parts are suitable for the assembly of the prototype.



Figure 4.2: Hand Assembly Prototype

Figure 4.3 depicts a close up of the finger assembly from the hand prototype. A cable tie secured with an epoxy agent is used to fix the leaf spring to the finger base. This is suitable since the cable tie holds the spring in place while the epoxy reinforcement prevents any slippage of the spring.

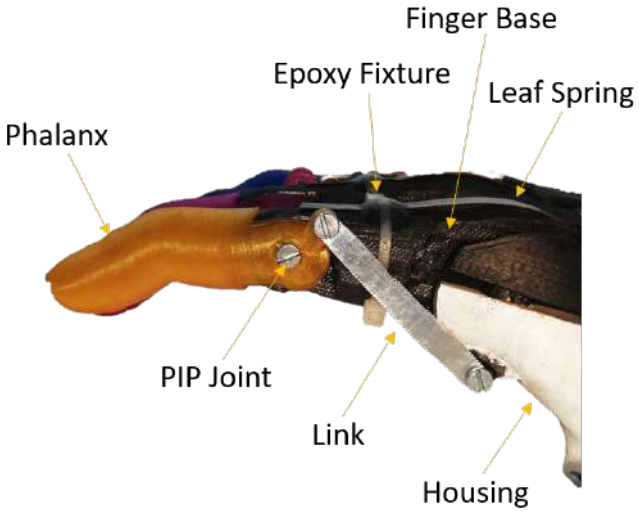


Figure 4.3: Finger Assembly Prototype

4.2 Control Scheme

4.2.1 Force Sensing Finger Pads

Force sensing resistors (FSRs) are sensors which are sensitive to touch. The resistance of the sensor varies depending on the force applied to it. This enables the system to use sensors to detect physical pressure, squeezing and weight. While their low cost makes them suitable for a cost-effective design.

These sensors are known to have poor accuracy. However, since the only requirement of the sensor is that it act as a limit switch for when contact is made, its ability to accurately measure the contact force is irrelevant. As long as proper calibration is ensured, these sensors will be suitable for this application.



(a) Force Sensitive Resistor

(b) Touch Sensitive Finger Pad

Figure 4.4: Hand Tactile Sensor

The FSR sensors are embedded in silicon to form touch-sensitive pads, as depicted in Figure 4.4b. These pads are then fixed to the fingers and assist the hand with grasping and interacting with objects. The soft surface of the pads dampens the initial contact between the fingers and object while also partially deforming, increasing the contact surface.

However, the pad's main function is to deliver force sensory feedback of the fingers to the controller. This is vital for grip control, enabling the hand to conform to the shape of the object. Force feedback allows for correction when the grip force is too low or high, preventing an overly loose or tight grip around the object.

4.2.2 Sensor Feedback Control Scheme

The adaptive grip is vital to provide the user with the fine motor skills required in everyday life. For the prosthetic hand to be able to perform adaptive grip, finger pad sensors are equipped to the fingertips to transmit feedback to a controller, as shown in Figure 4.5. A control system is designed utilising the touch-sensitive pads, as illustrated in Figure 4.6. The control scheme monitors the force the fingers apply onto an object being gripped, and enables

the hand to hold the object securely without damaging it. Bang-bang control is used, where the actuator is activated if the sensor pad registers a force reading below the set limit, and deactivated when the set limit is exceeded. However, activating the actuator continuously before the set limit is reached could result in the Nitinol wires burning out due to overheating from the continuous current, leading to the actuator's stroke being reduced due to the shape memory of the wires resetting.

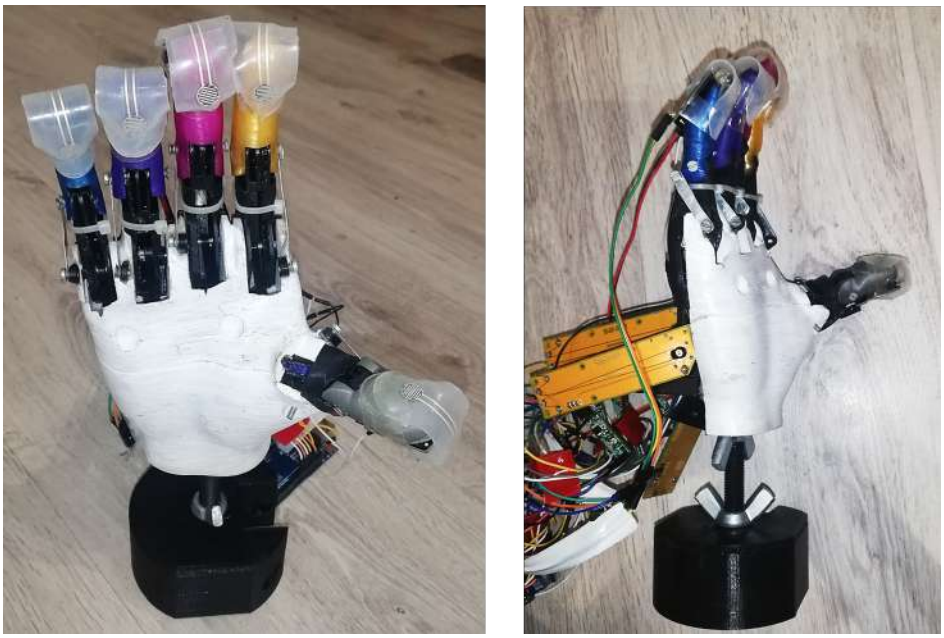


Figure 4.5: Prosthetic Hand Outfitted with Finger Pad Sensors

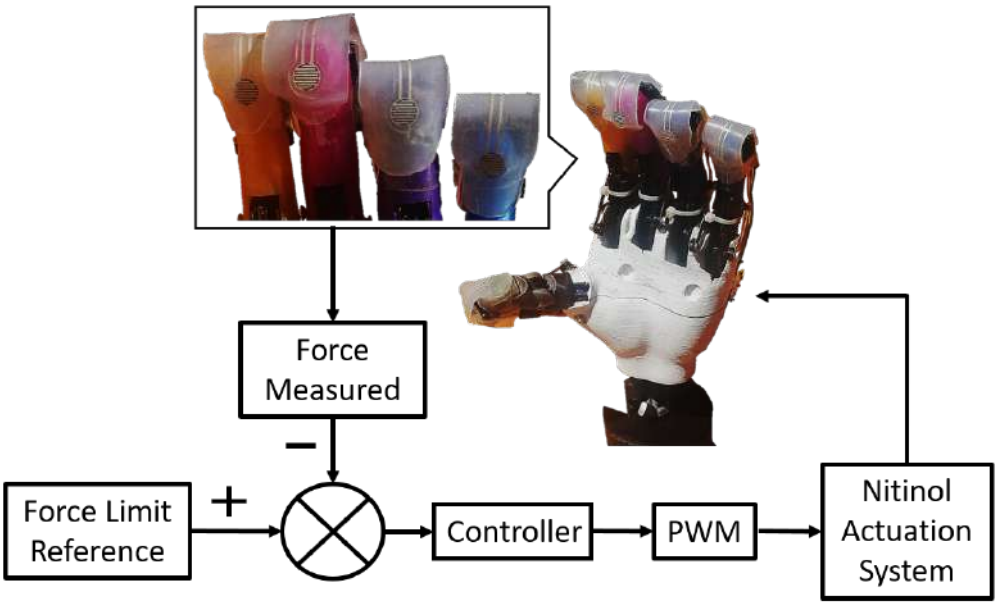


Figure 4.6: Adaptive Grip Control Loop

PWM is incorporated into the control loop to prevent the Nitinol wires from overheating. The PWM pulses the current to the actuators instead of sending a continuous flow. This is

achieved through a duty cycle, which describes the percentage of time the current flows, as shown in Figure 4.7.

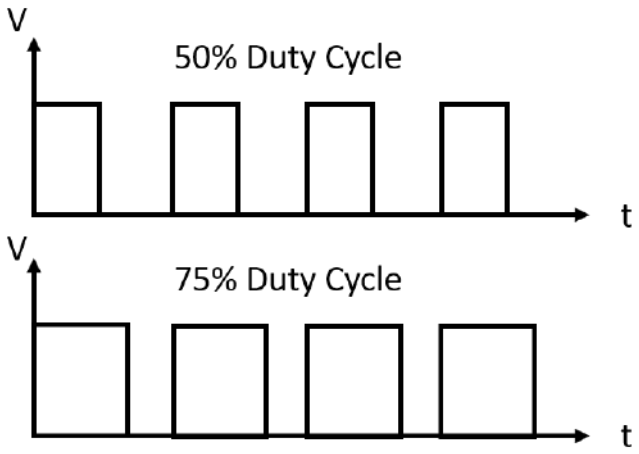


Figure 4.7: Duty Cycle

By correctly adjusting the span of the pulse width, the Nitinol wire is given sufficient cooling time, thus preventing burnout. However, if the pulse width is too small, the heating time will be insufficient for activating the Nitinol wire. Conversely, if the pulse width is too large, the wire will still overheat. Through experimentation, it was determined that the optimum duty cycle ranges from 50-91% [44].

4.3 Electronics

4.3.1 Microcontroller

The microcontroller is an important electronic component responsible for processing sensory data and initiating commands to control the prosthetic hand. A specific number of pins are required to receive the feedback signals from the FSRs as well as issue the resulting commands to the Nitinol actuators. Factors such as the data processing speed, memory storage, programming platform, size and cost were also taken into account during the selection process. The Arduino UNO was deemed the most appropriate choice.

As shown in Figure 4.8, the microcontroller possesses the required five digital pins for the Nitinol actuators and five analogue pins for the finger pad sensors. The board can supply 5 V to power the FSR sensors during operation. The ATmega328P chip installed into the board grants the Arduino UNO a CPU speed of 16 MHz; sufficient to process sampling speeds as high as 500 Hz. Which is within the frequency limits for EMG mapping, as discussed in Section 1.2.2.3. Although the board only has 2 KB of SRAM, the cache memory is sufficient for the prototype's operation [45].

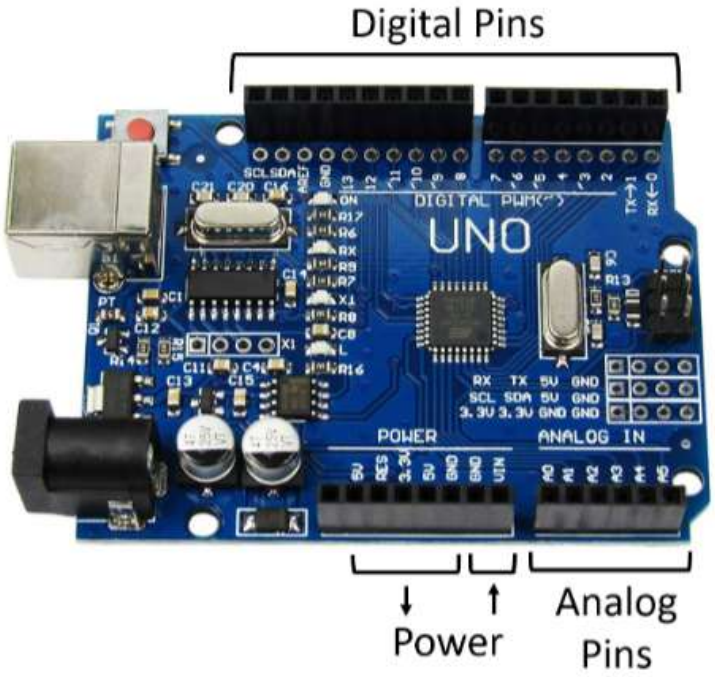


Figure 4.8: Arduino UNO Board

4.3.2 Hardware Architecture

The circuitry layout of the hand is depicted in Figure 4.9. Five 9 V batteries are used to power the Nitinol actuators individually, with a sixth 9 V battery powering the Arduino board.

MOSFETs were used to regulate the current to the Nitinol actuators. The MOSFETs receives signals from the digital pins of the Arduino to control the actuators. Similarly, the voltage sensors attached to the FSRs, are connected to the analogue pins of the board. The pin connections are depicted in Figure 4.10.

The board is used to power the finger pads (FSRs) with a 5 V power supply. The finger pads are connected in parallel with the 5 V power source. The connection paths of each component are tabulated in Table D.1.

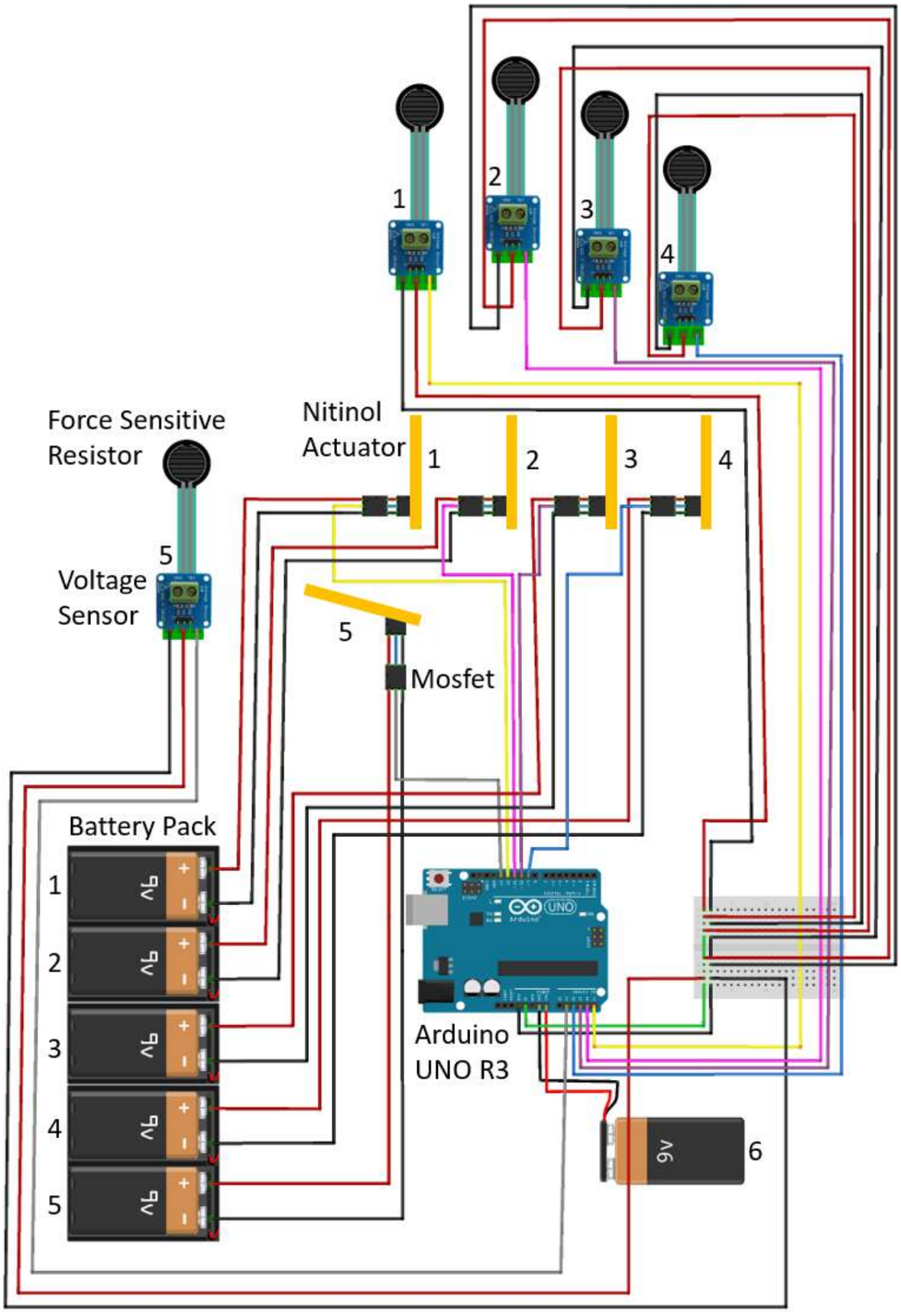


Figure 4.9: Prosthetic Hand Circuit

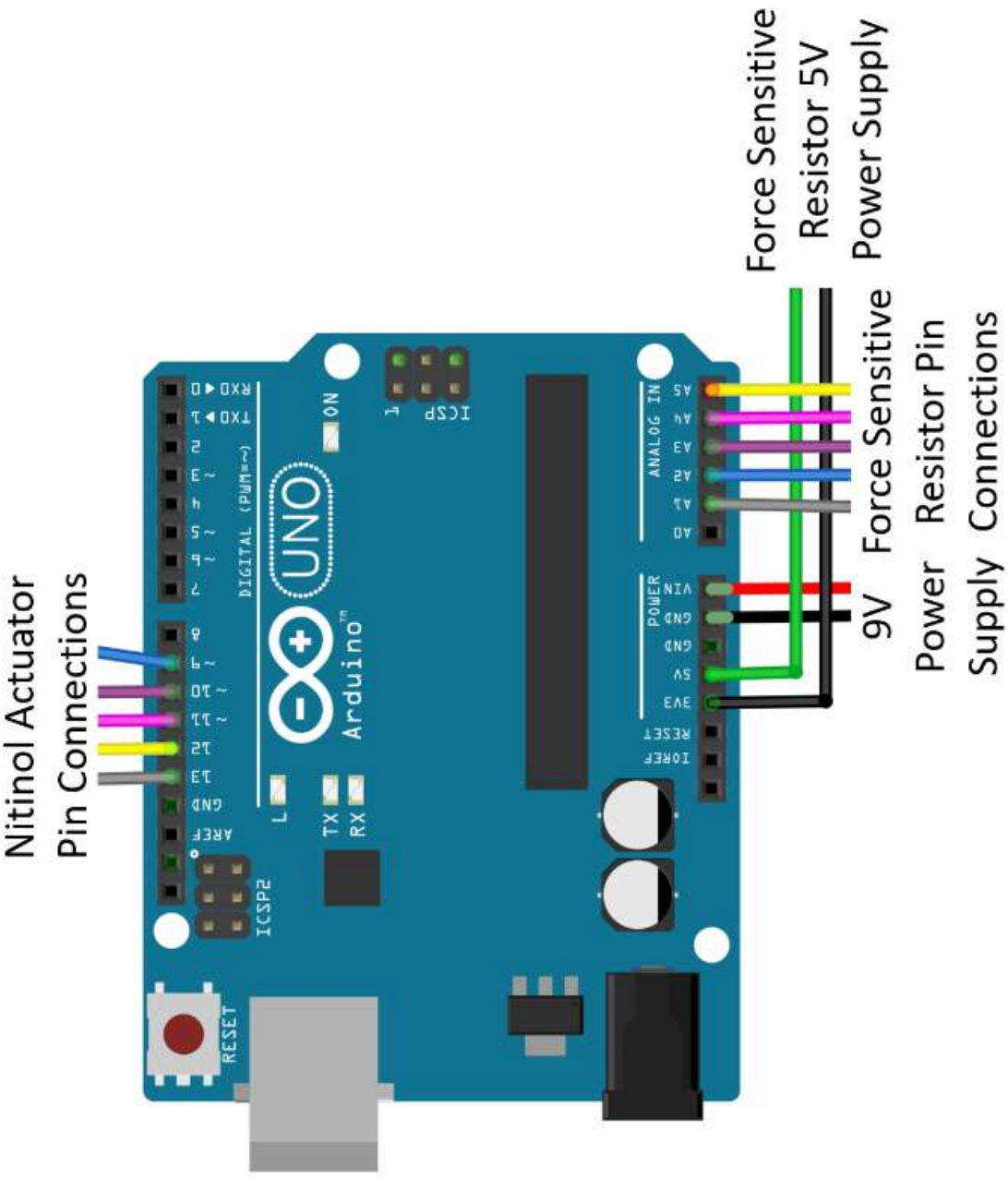


Figure 4.10: Arduino UNO Close Up View from the Prosthetic Hand Circuit

4.4 Cost Estimation

For the Nitinol actuation mechanism to be economically viable, the total cost of the prototype has to be comparable to the manufacturing cost of the past Wits hand (R3 000). The costs of the electronic components, materials and manufacturing processes are consolidated in Table 4.2.

Table 4.2: Cost Estimation

Part	**Components/ Manufacturing**	**Unit Price (R)**	**Price (R)**
Nitinol Actuator	Nitinol Wire (0.381 mm Diameter)	6.50 per 10 cm	32.50
	Actuator Circuit Mounting Board	115.68	578.40
	Labour	100.73	503.65
MOSFET	Miga Analog Driver v5	172.65	863.25
Force Sensing Finger Pad	FSR Sensor Module	112.28	564.40
	RTV Silicone 10 g	0.40	2.00
Hand Housing	ESUN PLA+ Filament	0.24 per g	17.93
	3D Printing	57.80 per hr	462.40
Finger Segments	ESUN PLA+ Filament	0.24 per g	24.51
	3D Printing	57.80 per hr	596.92
Metal Linkages	Galvanised Steel Sheet	172 per 915 x 1830 mm sheet	Negligible
	Metal Punching	University Facilities	University Facilities
Bolts	M3 / 5 mm, 8mm, 15mm long	0.23 per g	38.95
Nuts	M3	0.23 per g	9.02
Micro Controller	Arduino UNO R3	175	175
		Total	3 868.93

The total cost of producing the prototype was R3 868.93, similar to the cost of the previous Wits hand. This is a substantially lower cost than that of commercially available hands, which typically cost upwards of $11 000 [3].

5 Finger Positioning

5.1 Finger Positioning Test

The utility and dexterity of the prosthetic hand are dependent on the positioning performance of the Nitinol actuators for the fingers. The positioning performance was quantified using response time, precision and accuracy. These qualities are vital for smooth transitions between different grasps of the hand during operation. Smoother grasp transitions are better for mimicking anthropomorphic hands and increasing the usability of the prosthetic. Since the prosthetic hand consists of five individual digits, the first phase of experimentation focused on a single finger testbed, as shown in Figure 5.2.

An MPU6050 sensor was used to track the finger angle and angular acceleration. From this, the positioning performance for different voltages was determined by comparing the results to the desired path. The finger responsiveness was analysed by calculating the time constant and angular velocity. The effect of varying the sampling frequency was determined; with the maximum sampling frequency tested being 500 Hz (the same sampling frequency of the EMG sensors used for the prosthetic), as discussed in Section 1.2.2.3.

5.1.1 Apparatus

An MPU6050 sensor was attached to the finger base and used to track the trajectory of the finger. The sensor, illustrated in Figure 5.1, has both a 3-axis accelerometer and a 3-axis gyroscope built into a single chip. The accelerometer measured the rate of change of velocity while the gyroscope measured the orientation and angular velocities.

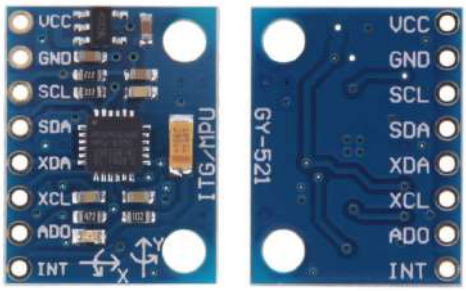


Figure 5.1: MPU6050 Sensor

The MPU6050 provides an I2C interface for communication with the micro-controller. Arduino libraries simplify the communication and return the measurements in a simple format [46]. Library 'MPU6050_tockn.h' was used to convert the raw data of the accelerometer and

gyroscope into angular readings. This was achieved using a complementary filter to combine the accelerometer and gyroscope readings [47].

The accelerometer was suitable to measure orientation in static conditions while the gyroscope was used for measuring tilt in dynamic conditions. The accelerometer and gyroscope signals were passed through a low and high pass filter, respectively, to combine the two readings. This was achieved with Equation 5.1, where α typically equals 0.02 for the MPU6050 sensor [48] The uncertainty analysis of the filtered angle using the MPU6050 sensor is carried out in Appendix C.2. These uncertainties are superimposed onto the finger positioning results in Section 5.2.

$$filtered_angle = (\alpha \times accelerometer_signal) + ((1 - \alpha) \times gyroscope_signal) \quad (5.1)$$

The 3D printed finger mechanism was mounted to the testbed as shown in Figure 5.2. Refer to Figure 2.7 for detailed finger assembly. The Nitinol actuator was attached to the finger link system and then fixed to the testbed. When the Nitinol actuator was activated the finger curled inward while a bias steel leaf spring was used to extend the finger outwards again when the actuator was deactivated.

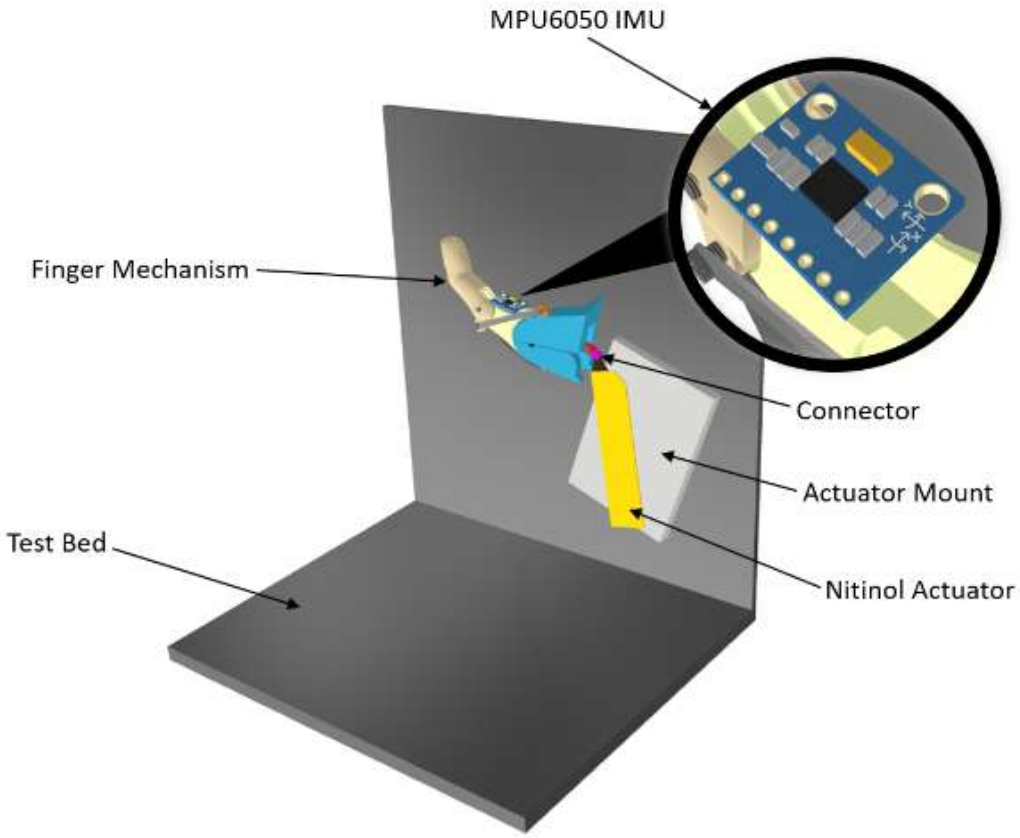


Figure 5.2: Finger Positioning Test Apparatus

The Arduino circuit schematic for the experiment is displayed in Figure 5.3. A computer interfaces with an Arduino UNO to relay the desired finger motion patterns to the testbed. A variable DC power supply was used to power the actuator. The third-party software, Tera Term, was used to record the finger position.

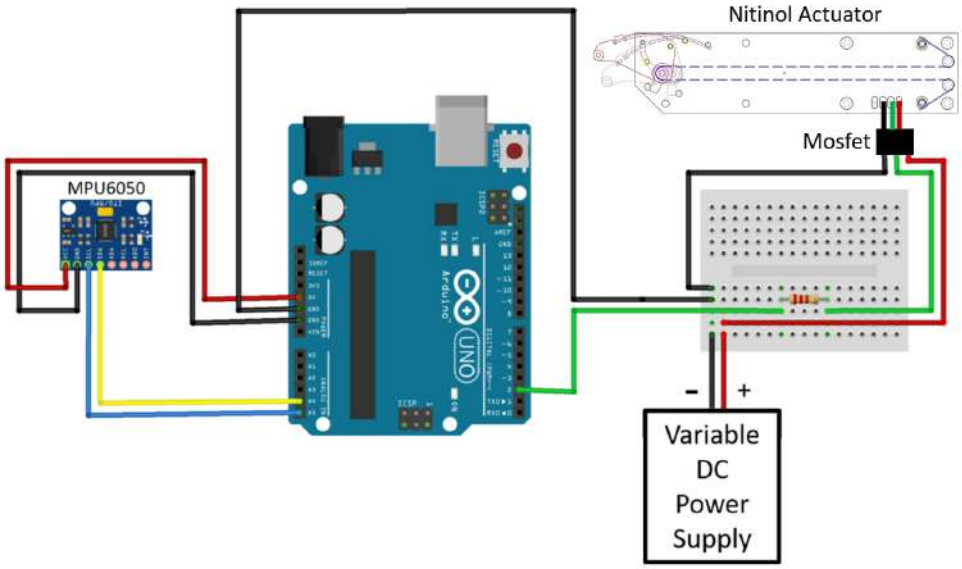


Figure 5.3: Finger Positioning Test Circuit

5.2 Finger Positioning Results and Discussions

5.2.1 Response Time Analysis

A square step signal was used to analyze the system's response to a dynamic setpoint. At 3 s the desired angle jumped from 30° to 50° (linear actuation from 0 mm to 6 mm), held for 1 s before being dropped back to 30°. Time constants and angular velocities for both the step-up and step-down responses were determined from the step function results. This was necessary since the actuation methods were different for the step-up and step-down paths. The step-up response was dependent on the Nitinol-driven actuator and input voltage, while the step-down response was dependent on the bias spring and Nitinol cooling rate. A summary of the step signal results is shown in Table 5.1.

The 7 V results produced the smallest overshoot, with a maximum 0.09° overshoot for both 200 Hz and 500 Hz sampling frequencies. Conversely, the 11 V responses generated the largest overshoot, with the worst case being a 1.89° overshoot for a 20 Hz sampling frequency. This correlates the results obtained using the analytical model developed in Section 3.2.4. This was due to the 11 V input voltage heating the Nitinol quicker compared to smaller input voltages.

A smaller sampling frequency (20 Hz) produced longer heating periods for the Nitinol wire than higher sampling frequencies (200 Hz and 500 Hz), increasing the heating rate of the Nitinol and causing the wire to contract faster and a peak angular velocity of 453.3 °/s. This resulted in the parameters with the worst overshoot performance achieving the smallest heating period time constants (t_h). The t_h for 11 V at 20 Hz was 0.03 s while the t_h for 7 V at 500 Hz was 0.14 s.

From Figure 5.4, it can be seen that the 0.14 s time constant was caused by a sluggish step-up response. This was because the heating periods for a 500 Hz sampling frequency were too small to effectively heat up the Nitinol, resulting in an over-damped system. This result was predicted by the analytical model of the system.

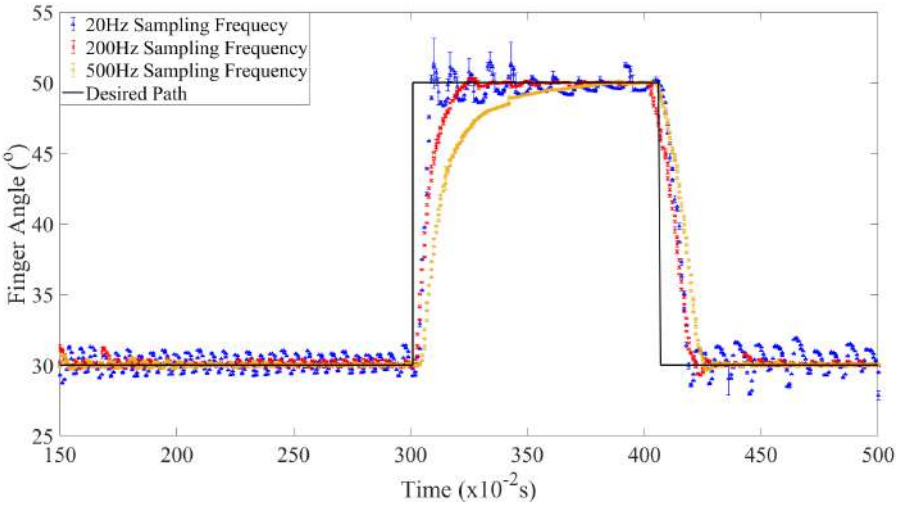


Figure 5.4: 7 V Step Signal

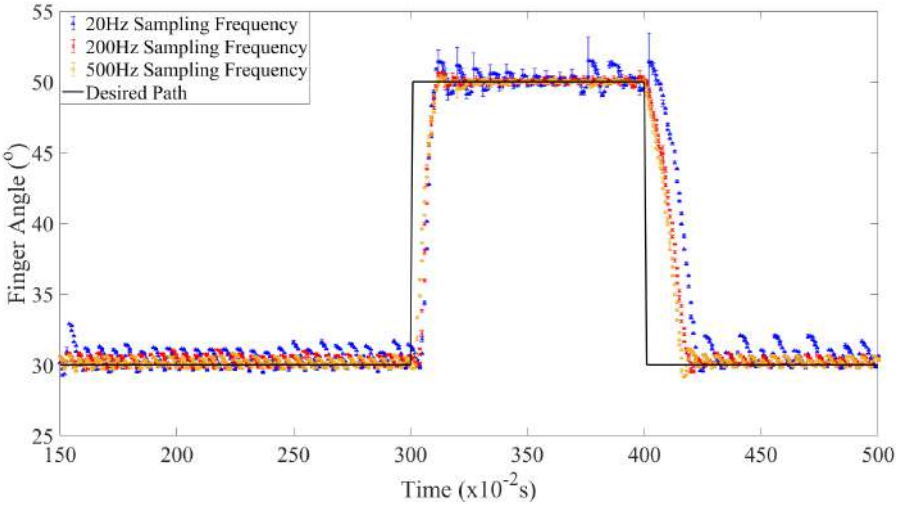


Figure 5.5: 9 V Step Signal

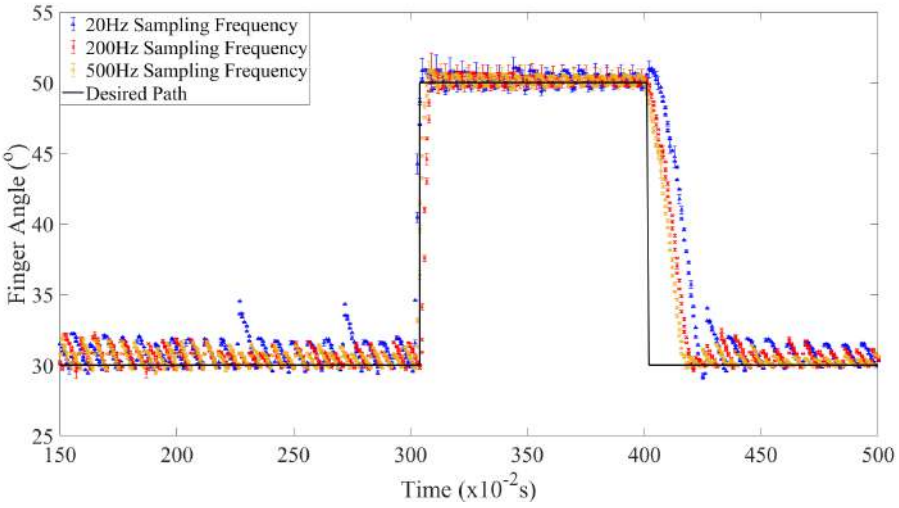


Figure 5.6: 11 V Step Signal

The calculated theoretical t_h was 0.351 s for an 11 V input voltage with a 500 Hz sampling frequency, which is significantly larger than the experimental result. In fact, all theoretical t_h values were larger than the experimental results. This was because of the approximation used for the leaf spring deflection, which was determined using the finger assembly CAD model, as illustrated in Figure 2.6. During the manufacturing of the finger, the fixture of the leaf spring may have differed slightly from the specified position on the CAD model, which could have led to an underestimation of the spring deflection and bias force.

Quicker step-up responses were measured for 200 Hz and 500 Hz sampling frequencies, with input voltages of 9 V and 11 V, as depicted in Figures 5.5 and 5.6. As discussed earlier, larger input voltages reduced the Nitinol activation time by increasing the heating rate of the wire. The faster heating rates negated the small heating period problem experienced for the 7 V input. This resulted in a t_h of 0.06 s for 9 V and a t_h of 0.04 s for 11 V at 500 Hz, which is 57% and 71% quicker than the t_h for 7 V at 500 Hz, respectively.

However, all step-up responses produced faster t_hs than the Waikato SMA finger (1.1 s) and Marmara SMA finger (0.5 s). This was because the mechanical design of the transmission system only required a 8 mm stroke to fully rotate the finger, as opposed to the minimum 18 mm stroke required by a tendon-driven system. This resulted in a peak angular velocity of 453.3 $°/s$ for an input voltage of 11 V with a sampling frequency of 20 Hz. This is shown in Table 5.1, which tabulates the results for the step signal positioning test. This led to an oscillatory response and an overshoot of 1.89° as the actuator overcompensated when the finger angle dropped below the desired value. The overshoot for 11 V was reduced to 0.83° at 200 Hz and 0.34° at 500 Hz. The dampened oscillatory responses are due to the reduced heating rates of the higher sampling frequencies coupled with the increased monitoring rate of finger position relative to the desired angle.

Table 5.1: Results for Step Signal Positioning Test

		Voltage (V)		
Sampling Frequency (Hz)	**Parameters**	**7**	**9**	**11**
20	**Max Overshoot (°)**	1.39	1.44	1.89
	Time Constant (s) Heating	0.06	0.04	0.03
	Max Angular Velocity (°/s) Heating	226.6	340	453.3
	Time Constant (s) Cooling	0.11	0.15	0.13
	Max Angular Velocity (°/s) Cooling	-123.6	-91.2	-104.9
200	**Max Overshoot (°)**	0.09	0.62	0.83
	Time Constant (s) Heating	0.09	0.04	0.04
	Max Angular Velocity (°/s) Heating	151.1	340.2	340
	Time Constant (s) Cooling	0.15	0.12	0.12
	Max Angular Velocity (°/s) Cooling	-90.8	-113.3	-113.2
500	**Max Overshoot (°)**	0.09	0.31	0.34
	Time Constant (s) Heating	0.14	0.06	0.04
	Max Angular Velocity (°/s) Heating	97.1	152	340
	Time Constant (s) Cooling	0.13	0.11	0.11
	Max Angular Velocity (°/s) Cooling	-104.6	-123.6	-123.4

Unlike the step-up response, the step-down response was independent of the voltage and sampling frequency parameters. The Nitinol cooling rate and leaf spring characteristics determined the response time of the step-down response. The finger extended outwards when the Nitinol wire elongated (cooled down) to its original length. The leaf spring assisted with stretching the wire and reduced the frictional effects within the transmission system. As a result, the time constant variation (maximum minus minimum) of all the tested parameters was 0.4 s.

The average cooling phase time constant (t_c) was 0.125 s, significantly longer than the smallest t_h of 0.03 s, but substantially faster than the Waikato finger (3.7 s) and the Marmara finger (1 s). The Nitinol-driven system also outperformed the modified Waikato finger with forced cooling that achieved a t_c of 0.8 s. This was due to the reduced linear actuation length required by the two-linked transmission. The wire requires a shorter cooling period to return the actuator and finger back to the outstretched position. These results are similar to the predicted theoretical t_c values which ranged between 0.13-0.14 s. The slight difference in the t_c values can also be attributed to an underestimation of the bias spring force.

The average maximum angular velocity was 109.8 °/s during the cooling phase; slower than the average angular velocities of commercial hands, such as 175.4 °/s for the Dexterous and 249.8 °/s for the Ada Hand [18]. However, the two-linked transmission enabled the Nitinol-driven hand to outperform past designs such as the Marmara finger which had a peak angular velocity of 25 °/s during the cooling phase.

5.2.2 Path Tracking Performance Analysis

A ramp signal was used to evaluate the tracking performance of the system. The finger angle was ramped up from 30° to 50° at 13.33 °/s, held in position for 1 s, and then ramped down to 30° at 13.33 °/s. The path tracking performance of the ramp responses can be seen in Figures 5.4, 5.9 and 5.11. The tracking performance is based on the path accuracy, which was determined by calculating the RMSe tracking error, which is the deviation between the desired and measured finger angles. The tracking errors of the ramp responses are displayed in Figures 5.8, 5.10 and 5.12. The accuracy of the path tracking was evaluated by examining the average tracking error, presented in Table 5.2.

The 7 V input voltage produced the best tracking performance, while the 11 V input voltage performed the worst. This is shown in the average tracking error values in Figures 5.8 and 5.12. The poor tracking ability of the system with an 11 V input is due to the actuator overcompensating, similar to the overshoot issues encountered for the step function.

Unlike the larger input voltages, 7 V heated the Nitinol slower. This prevented large overshoots of the finger angle and maintained average tracking errors between 0.607° and 0.652° for the ramp response. However, the slower heating rate leads to a sluggish and over-damped response for the step function for the 7 V input with 200 Hz and 500 Hz sampling frequencies. This resulted in average tracking errors of 1.514° and 1.654°, for 200 Hz and 500 Hz, respectively.

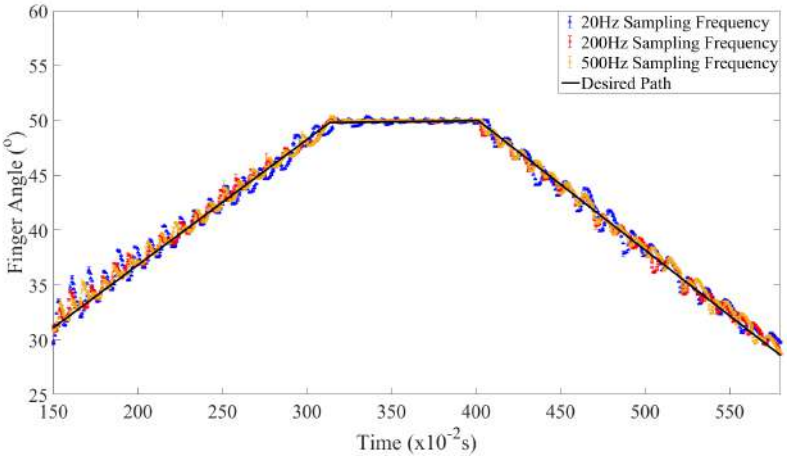


Figure 5.7: 7 V Ramp Signal

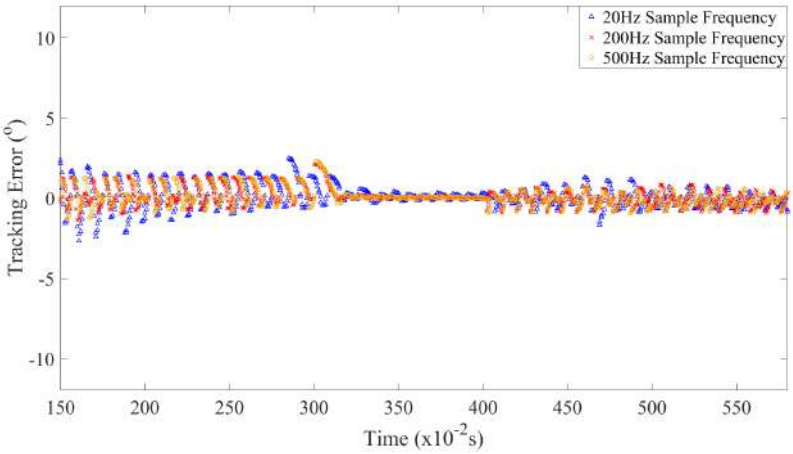


Figure 5.8: 7 V Ramp Signal Error

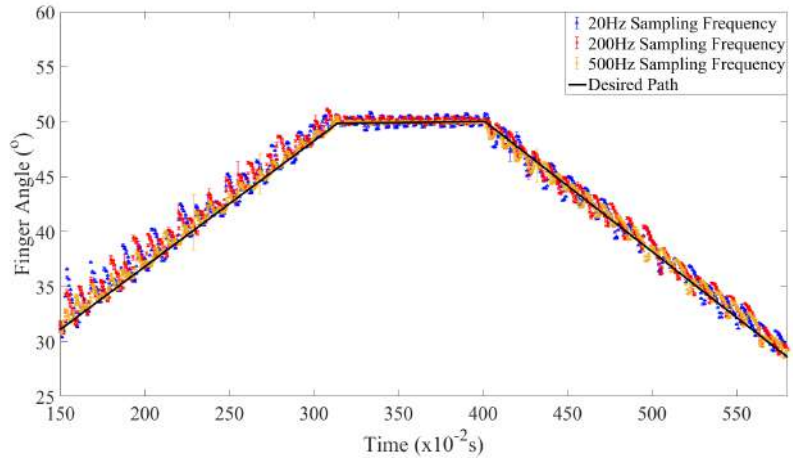


Figure 5.9: 9 V Ramp Signal

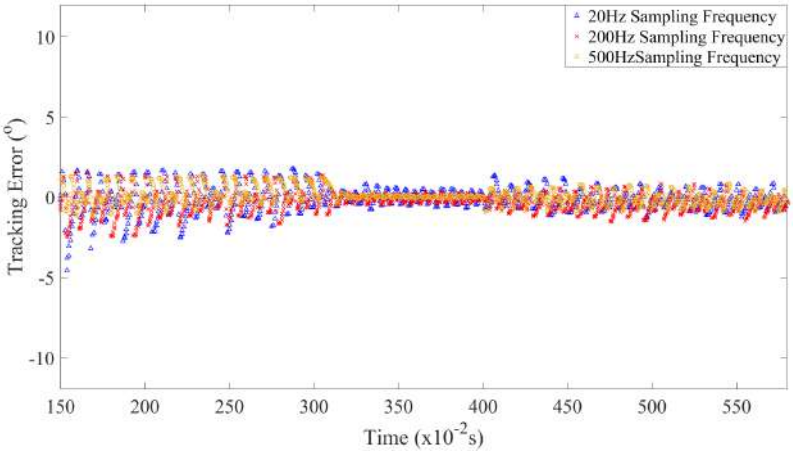


Figure 5.10: 9 V Ramp Signal Error

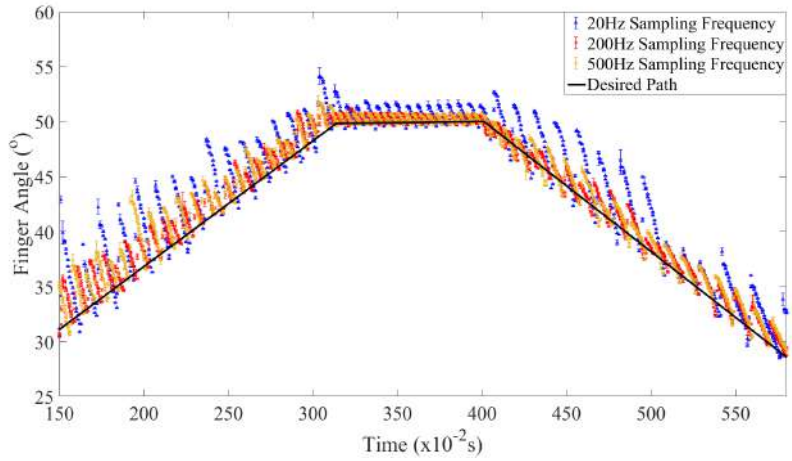


Figure 5.11: 11 V Ramp Signal

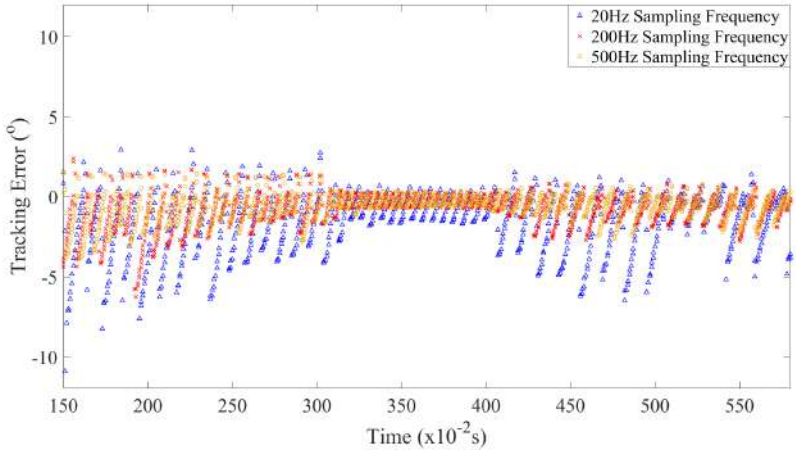


Figure 5.12: 11 V Ramp Signal Error

A balance needs to be found between the Nitinol heating rate (rise-time) and the tracking error and overshoot. It can be seen from Figure 5.9 that a higher sampling frequency curbs the overcompensation issue by reducing the heating period of the Nitinol wire. This is less effective for the 11 V input voltage since the heat rate of the Nitinol wire is still too high for the 200 Hz and 500 Hz sampling frequencies. A 9 V input voltage produced the smallest average step signal error for all cases and the second smallest average ramp signal error for all cases, with a maximum 2.5% deviation from the smallest average ramp signal error achieved. Therefore, a 9 V input voltage is considered the best operating voltage for the actuator since it is the best compromise between rise-time, overshoot and accuracy.

Like the other input voltages, larger sampling frequencies reduced the tracking error for the 9 V input from 1.36° at 20 Hz to 1.13° at 200 Hz and 500 Hz for the step response. While the average tracking error was only reduced by 2.6% by increasing the sampling frequency for the 9 V ramp response. There was only a 0.26% and 0.31% difference between the average tracking errors of the step and ramp signals, respectively, for 200 Hz and 500 Hz sampling frequencies.

This suggests that the effectiveness of dampening the Nitinol heating-rate through increasing the sampling frequency decreases after 200 Hz for the 9 V input.

Table 5.2: Average Path Tracking Error

		Voltage (V)		
Sampling Frequency (Hz)	**RMS Tracking Error**	**7**	**9**	**11**
20	**Average Step Signal Error (°)**	1.654	1.357	1.519
	Average Ramp Signal Error (°)	0.652	0.669	2.006
200	**Average Step Signal Error (°)**	1.514	1.131	1.398
	Average Ramp Signal Error (°)	0.651	0.653	1.003
500	**Average Step Signal Error (°)**	1.181	1.134	1.171
	Average Ramp Signal Error (°)	0.607	0.651	0.927

6 Finger Strength

Finger strength is a kinetic measure of the maximum force the prosthetic finger can impose on its environment. The strength is dependent on the actuator capabilities, mechanical design, and finger-object orientation. This measure relates to the overall grip strength as well as manipulation capabilities.

There are two main reasons for measuring strength on a single finger basis. The first is that there can be inherent variability in finger strength across different fingers even in cases where they are mechanically equivalent. The second is that any number of fingers can be used for grasping and manipulation, making finger strength the most independent measure of strength. Therefore, all five fingers were individually tested. Figure 6.1 illustrates the labels for each finger.

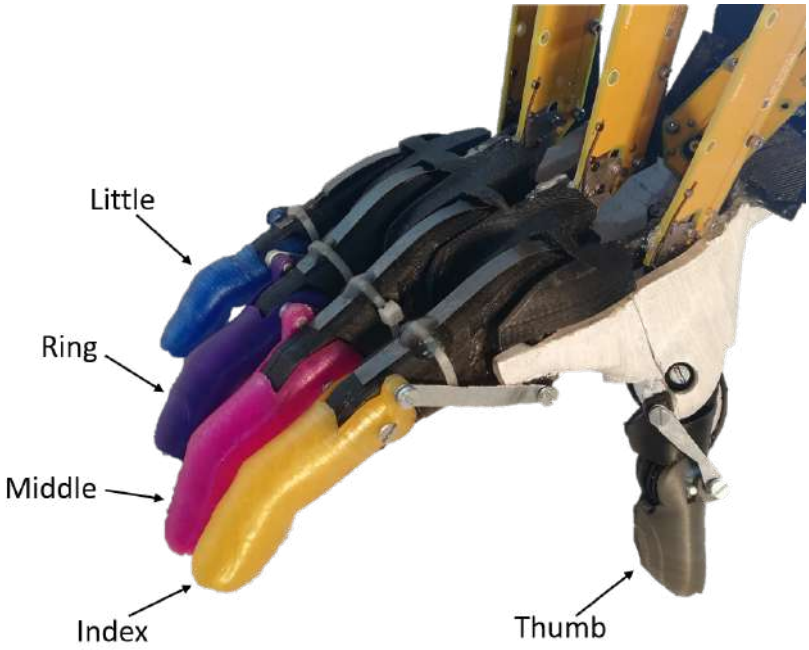


Figure 6.1: Labelled Prosthetic Fingers

Two types of forces were measured: the fingertip contact force and the finger grip strength of the fingers. The fingertip contact force is vital for the tripod pinch and grip as well as handling irregularly shaped objects, and determines the hand's ability to manipulate objects. The grip strength of the finger is important for the power, sphere, cylinder and hook grips, and is an indicator of the hand's ability to hold and carry objects.

6.1 Fingertip Force Test

6.1.1 Apparatus

The hand was fixed to a 12 mm diameter rod with two nuts. The rod was then fixed to a stand which suspended the hand. An HBM C9C load cell measured the fingertip contact force. The HBM C9C is a miniature force transducer designed to measure compression forces. The sensor has an accuracy class of 0.2 (i.e. ±0.2% of the full-scale reading) and can measure forces between 0 N and 50 N. The apparatus is illustrated in Figure 6.2.

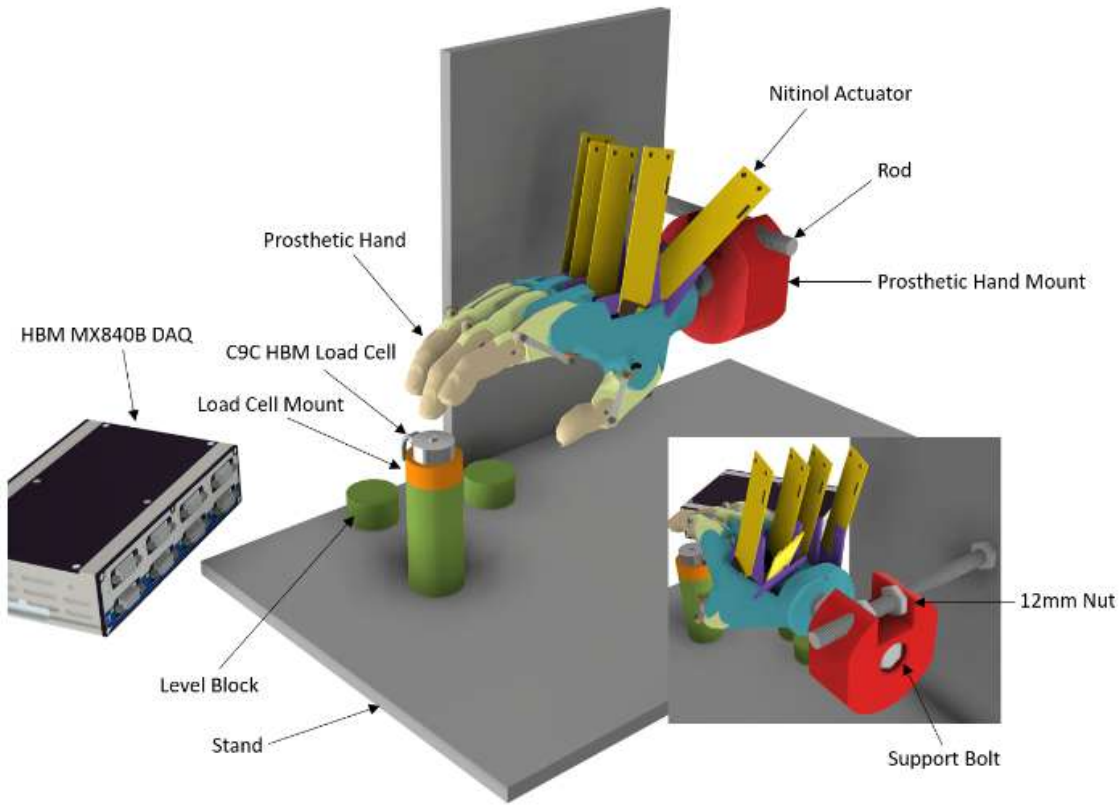


Figure 6.2: Fingertip Strength Test Rig

The fingertip force was measured with the finger in two different orientations. The orientations were defined using the PIP joint. Tests were conducted with PIP angles of 0° and 30°. This is important for examining the effect of the finger's orientation on the fingertip force with the linkage transmission system. A digital inclinometer was used to measure the PIP angle.

When the actuator was activated, the fingertip pressed down on the load cell. An HBM QuantumX MX840B DAQ was used to measure the readings from the HBM C9C load cell. Catman DAQ software was used to calibrate the HBM C9C and process the results.

6.2 Finger Grip Force Test

6.2.1 Apparatus

A digital hand dynamometer for patients with hand impairments was used to measure the finger strength as well as the total grip strength of the prosthetic hand, which is the sum of the finger forces imparted onto an object while griping it. The dynamometer has a range of 0-90 kg and an accuracy of 1% of full scale.

An adjustable mount was used to secure the dynamometer, as shown in Figure 6.3. The mount could be moved vertically along a bolt and fixed with two wing nuts. The bolt could also slide horizontally along a rail and be fastened with a third nut.

The prosthetic hand was mounted to a rod which suspended it above the test-bed, in a similar fashion to the fingertip strength test rig illustrated in Figure 6.2. The hand could be rotated around a bolt and oriented to fit the grip of the dynamometer. Two nuts were used to fasten the hand in place.

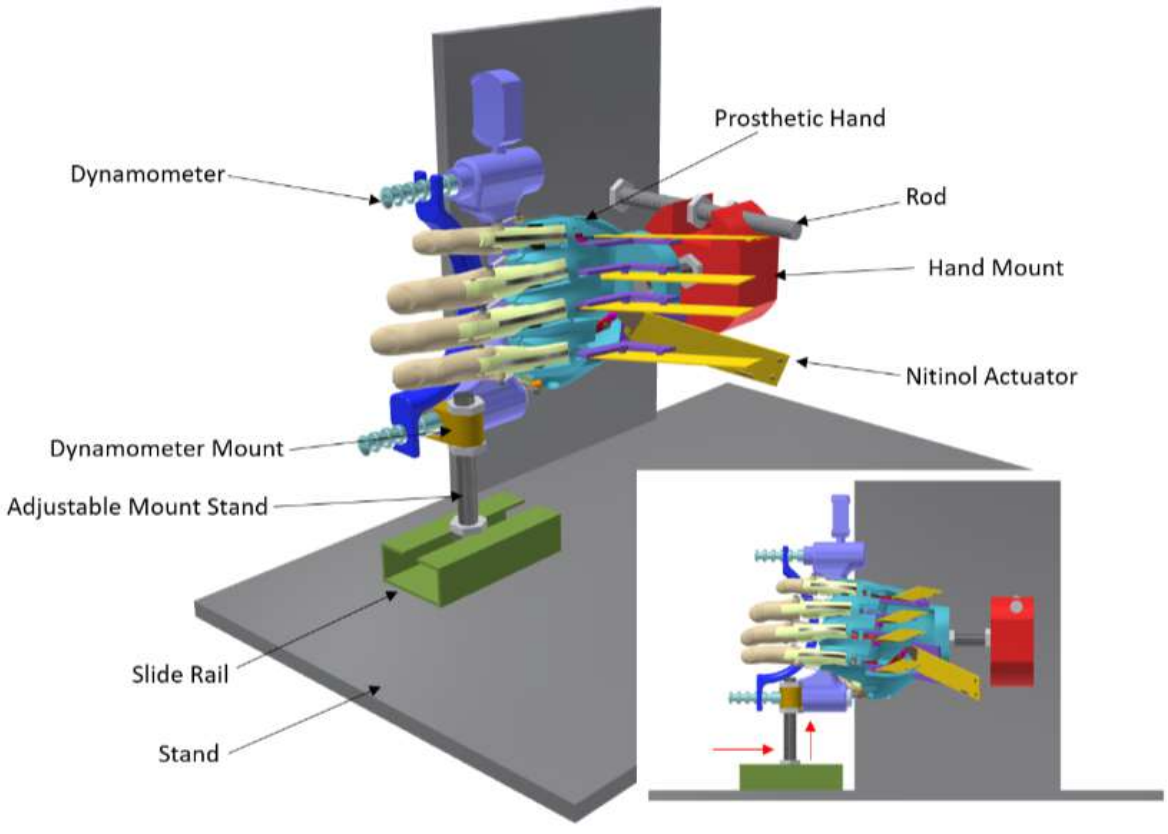


Figure 6.3: Finger Grip Strength Test Rig

6.3 Fingertip and Finger Grip Force Test Results and Discussion

A load cell positioned under the fingertips was used to measure the fingertip force at different PIP angles. The fingertip force indicates the ability of the hand to manipulate objects and perform actions which require fingertip contact, such as typing. Commercially available hands such as the Bebionic and iLimb produced fingertip forces of 12.47 N and 5.39 N, respectively. These are greater than the predicted fingertip force range of 1.27-2.46 N for the middle finger, that was obtained from the analytical model developed in Section 3.1.3. However, past 3D printed prosthetic hands with fingertip force ranges between 1.1-2.8 N were still able to perform complex dexterous tasks such as playing the violin [42]. Therefore, the link-based Nitinol powered design was approved, since the fingertip force range only needs to be large enough to perform the required dexterous tasks.

The fingertip force results for a PIP angle at 0° and 30° are shown in Figures 6.4 and 6.5, respectively. The maximum fingertip force measured was 3.51 N, with the ring finger oriented at a PIP angle of 0°. This maximum measurement was recorded when the finger first made contact with the load cell. The initial impact caused a peak in the force readings and tapered to a stable value in the quasi-static region. The measurement in the quasi-static region is taken as the true fingertip force measurement since the reading is not affected by the finger's inertia.

From Figure 6.4, it can be seen that the thumb, little and ring fingers generated average fingertip forces of 2.85 N, 2.91 N and 2.87 N, respectively, while the middle and index fingers produced smaller average fingertip forces of 2.42 N and 2.03 N, respectively. Since all the fingers tested used the same Nitinol actuators (same input actuation force), the differences in force results are due to mechanical amplification or differences in leverage between the two-link finger mechanisms utilised in the prosthesis. The middle and index two-link mechanisms possess larger moment arms due to the long finger base segments, placing the PIP joints further from the pin joint in the hand housing (fulcrum point) of the finger assembly, as illustrated in Figure 2.7. The force difference was repeated when the prosthetic fingers were oriented at a PIP angle of 30°.

From Figure 6.5, the fingertip force measurements range from 1.38-1.96 N, with a middle fingertip force of 1.42 N. There was a considerable difference between the experimental results and the results obtained from the analytical model in Section 3.1.4. The model predicted a fingertip force reduction of 0.71 N from a PIP angle of 0° to 30°. The experiment, however, recorded a fingertip force reduction of 1 N, which is 26% larger than the analytical prediction. This difference is due to the leaf spring deflection used for the analytical model, which was approximated using the 3D CAD model. However, during the manufacturing of the prosthetic, the placement of the leaf spring fixtures could have slightly differed from the CAD model,

causing inaccuracies in the initial baseline spring deflection approximation. The analytical model's inaccuracy increases from 4% to 14.4% as the spring's deflection increases, generating a larger bias force as the finger curls inwards. The 4% inaccuracy encountered for a 0° PIP angle, with minimum spring deflection, can be attributed to the model excluding the dampening effects of the silicone pads used for tactile feedback by the bang-bang controller.

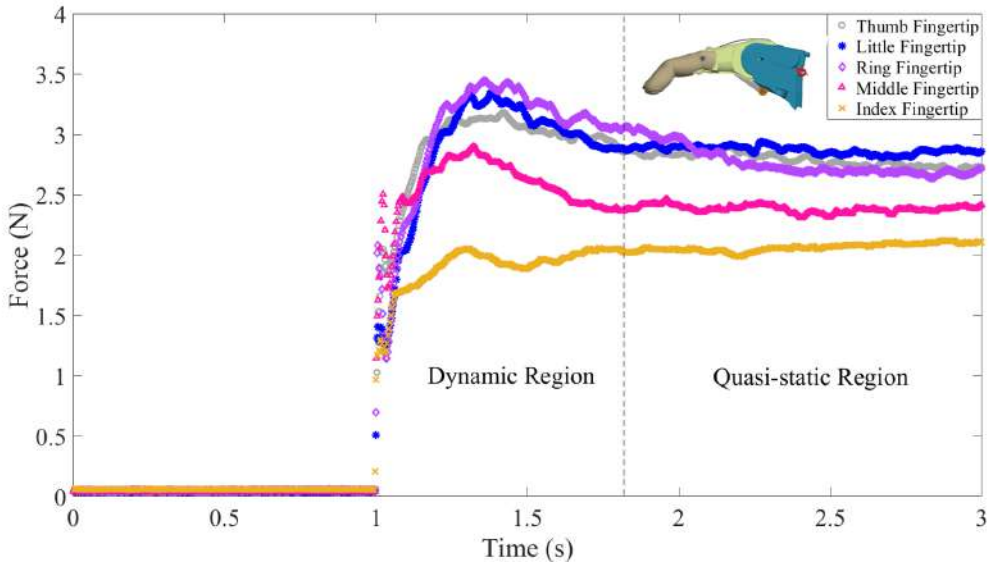


Figure 6.4: Fingertip Contact Force with a PIP Angle of 0°

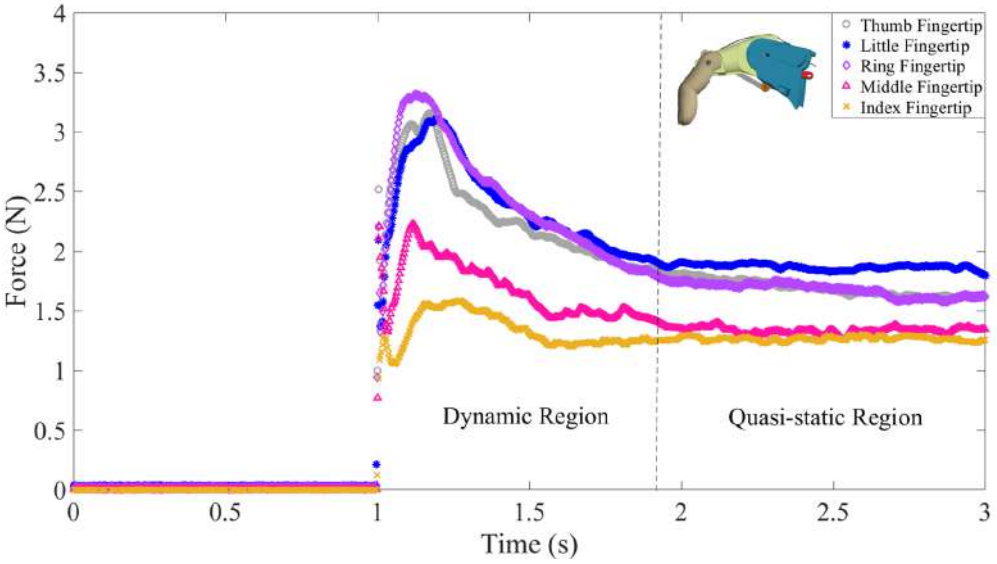


Figure 6.5: Fingertip Contact Force with a PIP Angle of 30°

The fingertip force readings between 2.03 N and 2.42 N for a PIP angle of 30° are smaller than commercial prosthetic hands such as the Bebionic and iLimb, but fall in the range of past 3D printed prosthetic hands, which were able to perform sufficiently. To achieve an adequate grip, the minimum force necessary to prevent slippage needs to be generated. As long as the

Nitinol powered fingers fulfil this requirement, the prosthetic hand will perform precise grasps satisfactorily.

From the fingertip force results, an estimation of the tripod grip and pinch can be made. The two grasps use the thumb, index and ring fingers. The major difference between the grasps is the degree of closure of the fingers, where the fingers are more closed for the pinch grip. PIP angles of 0° and 30° are used to estimate the tripod grip and tripod pinch forces, respectively. By consolidating the force readings of the three fingers, it is approximated that the grip force of the tripod grip is 7.3 N, while the grip force for the tripod pinch is 4.4 N.

For the power, hook and cylinder grips, the finger grip strengths need to be analysed. These grasps rely on the holding strength of the fingers to maintain the grasp under loading conditions. A dynamometer was used to measure the grip strengths of the fingers. The results of the dynamometer are tabulated in Table 6.1.

Table 6.1: Finger Grip Strength Results

Grip	**Grip Strength (N)**			
	Reading 1	**Reading 2**	**Reading 3**	**Average**
Index Finger	5.4	5.4	5.3	5.37
Middle Finger	5.5	5.3	5.5	5.43
Ring Finger	5.5	5.7	5.7	5.63
Little Finger	7.2	7.4	7.4	7.33
Power	16.8	16.7	16.2	16.57

The SMA powered prosthetic hand produced an average power grip force of 16.6 N. This is 2.76 times the strength of the Tact Wits hand. The measured power grip force was smaller than the sum of the individual finger grip forces. This was due to the hand's shape. When the handle of the dynamometer is pulled, not all of the fingers make full contact due to the fingers having different lengths. This leads to an inefficient transfer of the finger grip forces. This was especially noticeable for the little finger, which was unable to fully wrap around the handle during the power grip tests. Therefore, the grip force is a function of the actuation force, transmission method and object size.

It is difficult to predict the necessary grip force required to maintain a particular grasp around an object since it is largely dependent on the friction between the object and the fingers. Therefore, the range of objects that can be held and manipulated by the prosthetic hand can only be determined through physical testing.

7 Mandatory Grips

7.1 Grip Control Test

For a prosthetic hand to be deemed practical, it must be able to perform the five-fingered power, sphere, cylinder and hook grips as well as the three-fingered tripod grip and pinch, as illustrated in Figure 7.1. These hand gestures are the minimum requirements for the user to achieve sufficient dexterity and fine motor skills.

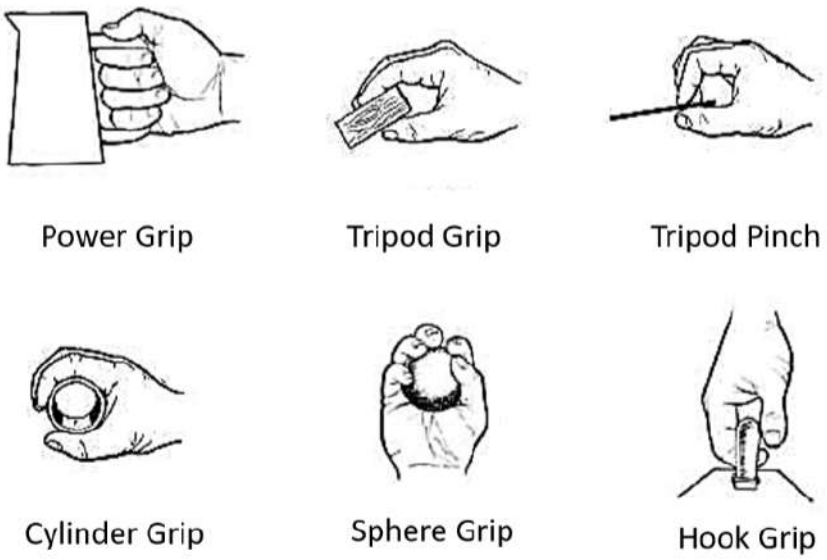


Figure 7.1: Hand gestures [5]

Objects with various shapes, sizes and weights are chosen to test the versatility of the prosthetic hand. These benchmark objects, illustrated in Figure 7.2, offer a wide range of potential targets that the user can encounter in their daily life. The hand is required to adjust its fingers around the contours of the object, without crushing or letting it slip. This dexterity is dependent on the sensor pads' performance and the feedback transmitted to the controller. The finger grip strength, however, is dependent on the Nitinol actuators and the transmission mechanism. It was determined that the fingertip force diminishes as the finger curls inwards. The effect of this phenomenon can only be determined through practical testing.

The six mandatory grips were split into two categories: five-fingered grasps which utilised the whole hand and three-fingered grasps which only used the thumb, index and middle fingers. A two-fingered pinch grip was used to test the hands precision. A five, three or two-fingered grasp is selected based on the object's size and grip being tested.

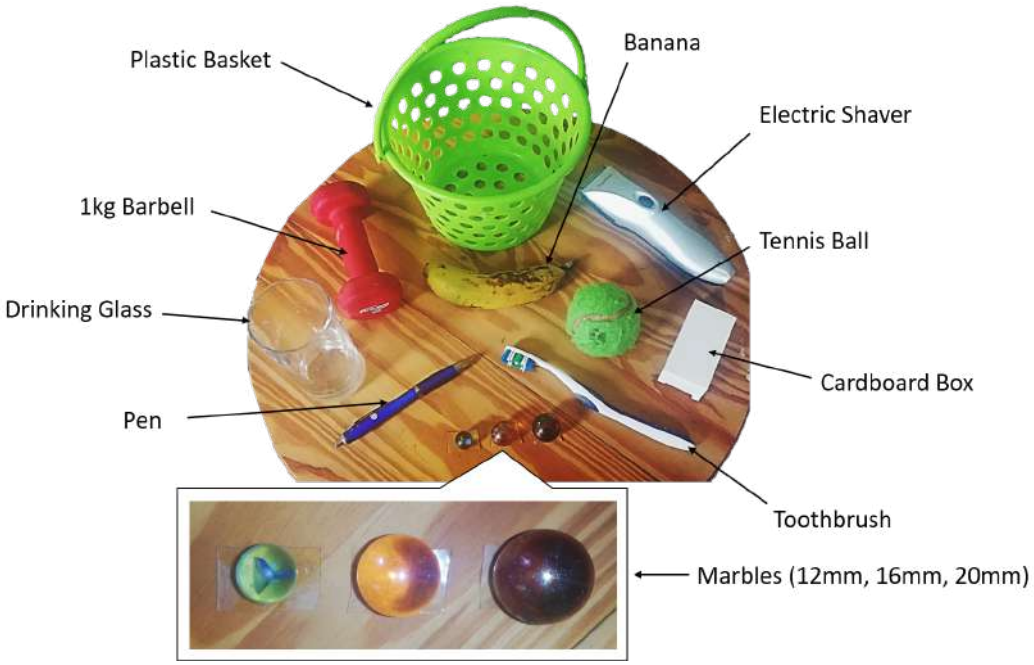


Figure 7.2: Objects to Test Hand Grip Performance

7.2 Grip Control Results and Discussion

The hand successfully completed the power, sphere, cylinder and hook grips, proving that it is capable of holding relatively large objects when using all five fingers. These grips were achievable due to the holding strength of the fingers powered by the Nitinol actuators, the sensor pads on the fingertips prevented the hand gripping the objects too tightly. This was important for the sphere grip where an overly tight grip would have squeezed the ball out of the hand, instead of holding it. Figure 7.3 depicts the hand performing these grips.

The hand was also able to successfully perform both three-fingered grips, as illustrated in Figure 7.4. The major difference between the tripod grip and pinch is the degree that the fingers curl inwards. This could have proved to be problematic since the fingertip force decreases significantly as the finger curls inwards, hindering the grip performance (as discussed in Section 6.3). However, the diminished grip strength of the tripod pinch proved to be sufficient during practical testing. This can be partially attributed to the fingertip sensor pads, which absorbed the initial impact force and deformed around the object, increasing the contact surface area. These two factors produced a secure grip and compensated for the lower grip strength.

The prosthesis' motor skills were sufficient to perform a two-fingered grip which requires higher precision than the three-fingered grips. In Figure 7.5 a, b and c, the hand can be seen performing the precision pinch on marbles with diameters of 12 mm, 16 mm and 20 mm, respectively. The prosthetic successfully held all of the marbles in a secure grip, demonstrating

the hand's ability to perform actions which require a high level of precision. The smooth surface of the marbles was easily gripped by the silicon pads folding around them, enabling the hand to manipulate and handle small objects with smooth gripping surfaces.



Figure 7.3: Five-fingered Grips

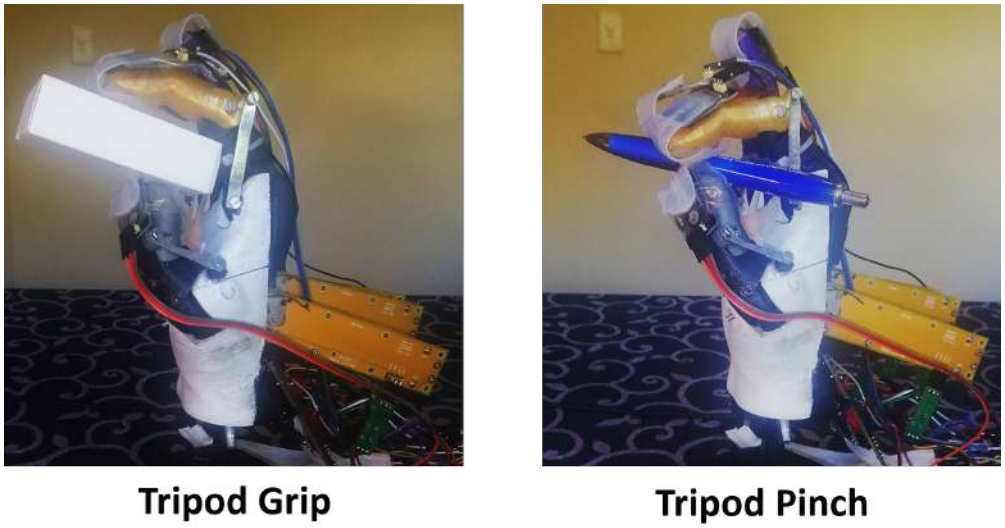


Figure 7.4: Three-fingered Grips

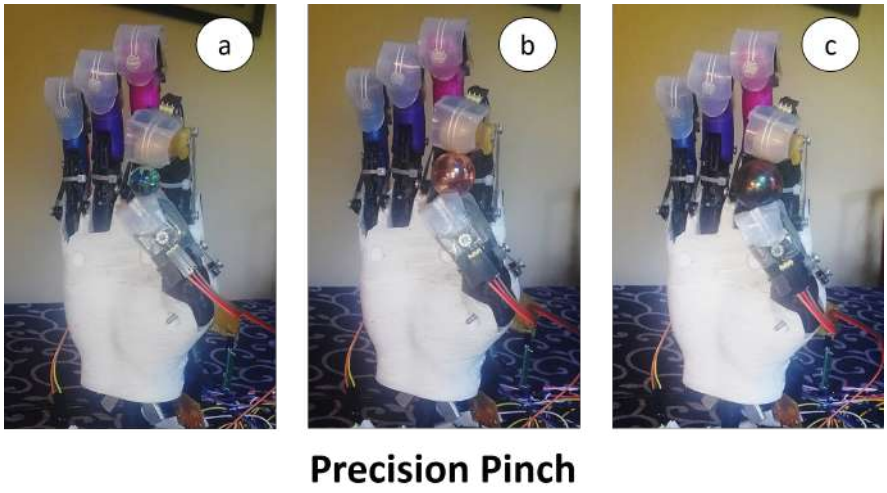


Figure 7.5: Two-fingered Grip

Figure 7.6 depicts the hand holding irregularly shaped objects that a user is likely to encounter. As a result of the sensory feedback sent to the controller from the sensor pads, the fingers were able to adjust their positions to match the contours of the objects, thus creating a secure grip. The ability to hold and manipulate these objects allow the user to perform daily tasks, without which would not be possible. The Nitinol actuators in the prosthetic can act as the means of actuation in a low cost prosthetic hand.



Figure 7.6: Hand Gripping Irregularly Shaped Objects

8 Conclusions

The research evaluated the feasibility and performance of SMA artificial muscles (specifically using Nitinol) for a prosthetic hand. The hand implemented a link based transmission mechanism instead of the traditional tendon-driven system found in most 3D printed hands. This modification improved the overall grip strength. The total cost of the prototype was R3 868.93, which is similar to the cost of the Tact Wits hand (R3 000) [6]. This chapter evaluates the prosthesis with respect to the objectives outlined in Section 1.4:

1. The Nitinol actuators displayed quick response times; especially during the heating cycle of the Nitinol, as was predicted by the analytical model. However, the theoretical heating time constants (0.17-0.39 s) were slower than the experimental results, which yielded time constants between 0.03-0.14 s. This was likely due to inaccuracies in the leaf spring deflection approximation which relied on the 3D model of the system, which increased the effect of the bias force.

   The theoretical inaccuracy is also reflected in the cooling phase response, which yielded quicker theoretical time constants (0.13-0.14 s) due to the overestimation of the bias force. The maximum experimental time constant recorded during the cooling phase was 0.15 s, which is significantly quicker than cooling phase time constants of between 1 s and 3.7 s exhibited by past Nitinol powered hands.

   Various sampling frequencies (20 Hz, 200 Hz and 500 Hz) and voltages (7 V, 9 V and 11 V) were tested to determine the best balance between response time, accuracy and overshoot. A 9 V power supply with a sampling frequency of 500 Hz was found to be the best combination; recording a maximum overshoot of 0.31° with a heating time constant of 0.06 s.

   The accuracy was evaluated using the RMS tracking error. For a 9 V voltage input, a 500 Hz sampling frequency decreased the average step signal tracking error from 1.357° to 1.134° and recorded a 0.651° average ramp signal tracking error.

   Finger speeds of 152 $^\circ/s$ and 123.6 $^\circ/s$ were recorded during the heating and cooling cycles, respectively, for a 9 V power supply with a 500 Hz sampling frequency. Although these speeds are lower than the speeds achieved by commercial prosthetic hands such as Dexterous (175.4 $^\circ/s$) and Ada (249.8 $^\circ/s$), the responsiveness and positioning performance of the Nitinol powered prosthesis was deemed adequate for everyday use.

2. The Tact Wits hand was deemed partially successful due to a low grip strength of 6 N. The Nitinol powered prosthesis produced individual finger grip strengths between 5.3 N and 7.4 N, while achieving an average power grip of 16.6 N. Although the power grip

force was 4.53 times smaller than commercial hands such as the Bebionic, it is 2.76 times larger than the Tact Wits hand; a notable improvement in strength.

The fingertip forces were evaluated to determine the prosthetic hand's ability to interact with objects. An analytical model was developed to track the fingertip force with respect to the PIP angle. The model predicted that as the PIP angle increased (finger curls inwards), the fingertip force decreased. This was supported by the experimental results.

An HBM C9C load cell was used to measure the fingertip forces of each finger. Fingertip forces of 2.03-2.91 N for a 0° PIP angle, and 1.38-1.96 N for a 30° PIP angle were recorded. These values are significantly smaller than the 12.47 N and 5.39 N forces achieved by the Bebionic and iLimb hands, respectively. However, the fingertip force range of the developed Nitinol-powered hand is comparable to past functional 3D printed hands with a fingertip force range of 1.1-2.8 N.

The tripod grip was estimated to be 7.3 N by consolidating the fingertip forces of the thumb, middle and index fingers. The fingertip forces were reduced when the fingers curled inwards to grip an object, resulting in the tripod pinch strength of 4.4 N.

3. For the prosthetic hand to be considered practical, the prosthesis was required to perform the six mandatory grips: power, hook, sphere, cylinder, tripod grip and tripod pinch. The hand successfully performed all six mandatory grips. The prosthesis demonstrated great dexterity during the tripod grasps, negating the problem of weak fingertip forces with silicon finger pads that initiated the adaptive grasp control of the hand. The adaptive grasp control enhanced the hand's ability to grip objects of all shapes and sizes.

   The precision of the prosthetic grip control allowed the hand to execute a seventh grip: a precision pinch using only the tips of the thumb and index finger. Successful execution of this grip allowed the hold marbles as small as 12 mm in diameter. Following the outcomes of the grip experiments the prosthetic was deemed to possess sufficient dexterity and fine motor skills for everyday use.

9 Future Work

9.1 Control Recommendations

The following considerations should be taken into account to enhance the future control performance of the Nitinol powered prosthetic hand:

- Currently, force-sensing finger pads are only used on the fingertips. More sensing pads could be fixed along the fingers to increase the sensing area and improve the adaptive grip control for larger objects.
- A fuzzy logic controller should be designed, which utilises EMG sensor inputs to control the hand.
- A filter could be created to enable EMG pattern recognition, enhancing the grip classification of the fuzzy logic controller.

9.2 Electronic Recommendations

The following changes are recommended to improve the usability and performance of the Nitinol powered prosthetic hand:

- The Arduino UNO should be replaced with a microcontroller with a higher processing speed and more memory to better cope with the EMG sensor data.
- The electronics need to fit within the hand housing to decrease the overall prosthesis size. A printed circuit board could be used to simplify the circuitry and eliminate the need for most wire connections.
- A lithium-ion battery should be considered to replace the current 9 V DC batteries. This would decrease the battery pack size and increase the battery life of the prosthesis.

9.3 Design Recommendations

The following design changes should be considered to potentially improve the performance of the Nitinol actuated hand:

- The use of thicker Nitinol wires could increase the finger holding and tip strengths. However, since thicker wires require longer cooling times, forced convection would need to be implemented to address this issue.

- For this research project, the actuator design was simplified, to allow easy installation of the Nitinol wire. This resulted in an elongated board design; increasing the size of the prosthetic hand. A more compact mounting board could be designed to allow the actuators to fit within the hand housing. A conceptual modification to the design is illustrated in Figure 9.1.

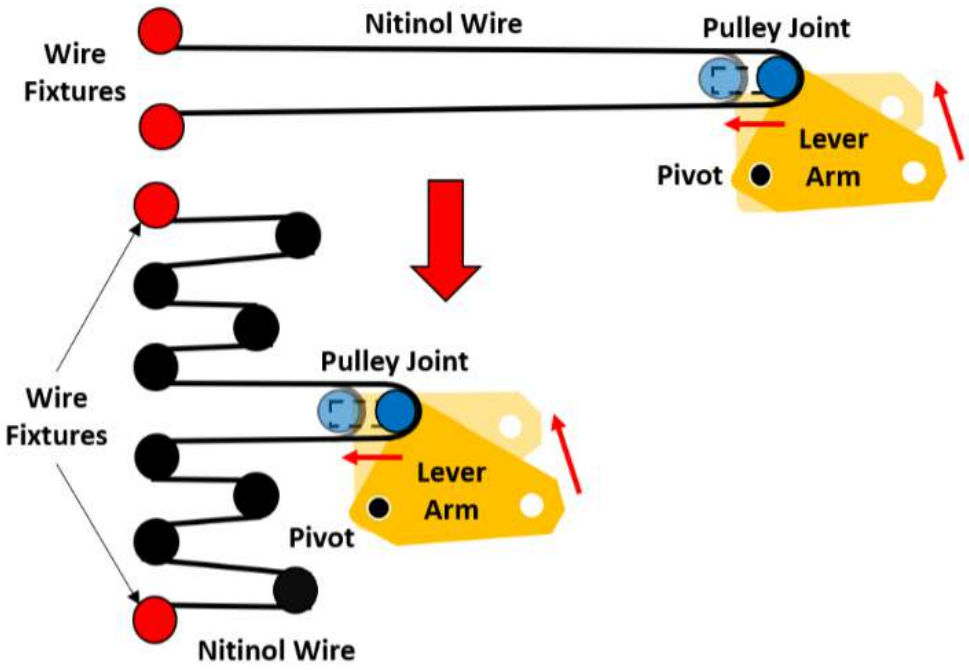


Figure 9.1: Modified Nitinol Actuator Layout

References

[1] R. Diagnosis. *Statistics by country for amputation*. 2015. URL: http://www.rightdiagnosis.com/a/amputation/stats-country.htm.

[2] C. Hughes and D. Ebadat. 'Upper extremity injuries in sub-Saharan Africa'. In: *2017 IST-Africa Week Conference (IST-Africa)*. 2017, pp. 1–8. DOI: 10.23919/ISTAFRICA.2017.8102413.

[3] A. Saenz. *How Much Is the Newest Advanced Artificial Hand? 11,000 USD (Video)*. 2017. URL: goo.gl/GLV3zQ.

[4] L. L. Mduzana, S. Visagie and G. Mji. 'Suitability of guidelines for screening of prosthetic candidates: lower limb for the Eastern Cape, South Africa: A qualitative study'. In: *South African Journal of Physiotherapy* 74.1 (2018), 9–pages.

[5] R. J. Schwarz and C. Taylor. 'The anatomy and mechanics of the human hand'. In: *Artificial limbs* 2.2 (1955), pp. 22–35.

[6] M. Irfaan. 'Grip control of a prosthetic hand using SEMG and haptic feedback'. In: *School of Electrical & Information Engineering, University of the Witwatersrand, Private Bag 3, 2050, Johannesburg, South Africa* (2017).

[7] J. H. University. *Anatomy of the hand | Johns Hopkins medicine*. 2020. URL: tinyurl.com/y4ds6xps (visited on 2020).

[8] G. ElKoura and K. Singh. 'Handrix: animating the human hand'. In: *Proceedings of the 2003 ACM SIGGRAPH/Eurographics symposium on Computer animation*. 2003, pp. 110–119.

[9] Smedley. *Electronic hand dynamometer instructions for use*. Baseline Evaluation Instruments, 2009.

[10] P. J. Kyberd. 'Assessment of functionality of multifunction prosthetic hands'. In: *JPO: Journal of Prosthetics and Orthotics* 29.3 (2017), pp. 103–111.

[11] W. William. *Bionic Hand Price List*. 2020. URL: https://bionicsforeveryone.com/bionic-hand-price-list/ (visited on 2020).

[12] W. William. *Ottobock bebionic Hand*. 2020. URL: https://bionicsforeveryone.com/ottobock-bebionic-hand/.

[13] A. G. Cutti et al. 'A motion analysis protocol for kinematic assessment of poly-articulated prosthetic hands with cosmetic gloves'. In: *Artificial organs* 41.12 (2017), E337–E346.

[14] H. Chen et al. 'Exploring the relation between EMG sampling frequency and hand motion recognition accuracy'. In: 2017, pp. 1139–1144. DOI: 10.1109/SMC.2017.8122765.

[15] A. Dynamics. *Finger and Partial Hand Prosthetic Options*.

[16] T. O. H. Project. *Dextrus*. 2013. URL: http://www.openhandproject.org/dextrus.php (visited on 2020).

[17] M. Molitch-Hou. *Build your own 3D printed robotic hand in less than an hour*. 2016. URL: shorturl.at/lDEY9 (visited on 2020).

[18] P. Slade et al. 'Tact: Design and performance of an open-source, affordable, myoelectric prosthetic hand'. In: *Robotics and Automation (ICRA), 2015 IEEE International Conference on*. IEEE. 2015, pp. 6451–6456.

[19] A. Y. Alhaddad et al. 'Toward 3D printed prosthetic hands that can satisfy psychosocial needs: grasping force comparisons between a prosthetic hand and human hands'. In: *International Conference on Social Robotics*. Springer. 2017, pp. 304–313.

[20] A. Mottard, T. Laliberté and C. Gosselin. 'Underactuated tendon-driven robotic/prosthetic hands: design issues.' In: *Robotics: Science and Systems*. 2017.

[21] A.-K. Mohamed and L. R. John. 'Single-trial EEG Discrimination between five hand movement imagery and execution'. In: *School of Electrical & Information Engineering, University of the Witwatersrand, Johannesburg, South Africa and Department of Human Biology University of Cape Town, South Africa* (2013).

[22] J. T. Belter et al. 'Mechanical design and performance specifications of anthropomorphic prosthetic hands: a review'. In: *J Rehabil Res Dev* 50.5 (2013), pp. 599–618.

[23] G. K. Klute, J. M. Czerniecki and B. Hannaford. 'McKibben artificial muscles: pneumatic actuators with biomechanical intelligence'. In: *1999 IEEE/ASME International Conference on Advanced Intelligent Mechatronics (Cat. No. 99TH8399)*. IEEE. 1999, pp. 221–226.

[24] T. Otieno and K. Abou-El-Hossein. 'Shape memory alloy actuator for the tool end-feed in lathe machining'. In: *Presented at the 4th Robotics and Mechatronics Conference of South Africa (ROBMECH 2011)*. Vol. 23. 2011, p. 25.

[25] K. O. Sanusi, O. L. Ayodele and M. T. Khan. 'A concise review of the applications of NiTi shape-memory alloys in composite materials'. In: *South African Journal of Science* 110.7-8 (2014), pp. 1–5.

[26] S. Ashley. 'Artificial muscles'. In: *Scientific American* 289.4 (2003), pp. 52–59.

[27] B. Hannaford et al. 'The anthroform biorobotic arm: a system for the study of spinal circuits'. In: *Annals of biomedical engineering* 23.4 (1995), pp. 399–408.

[28] B. G. Lau. *An intelligent prosthetic hand using hybrid actuation and myoelectric control*. University of Leeds, 2009.

[29] Dynalloy. *Flexinol actuator wire technical and design data*. 2018. URL: https://www.dynalloy.com/tech_data_wire.php (visited on 2018).

[30] C. A. Wright. 'Thermo-mechanical system identification of a shape memory alloy actuated mechanism'. In: (2016).

[31] H. Yin, Y. He and Q. Sun. 'Effect of deformation frequency on temperature and stress oscillations in cyclic phase transition of NiTi shape memory alloy'. In: *Journal of the Mechanics and Physics of Solids* 67 (2014), pp. 100–128.

[32] W. Huang. 'Shape memory alloys and their application to actuators for deployable structures'. In: (1998).

[33] F. Taylor and C. Au. 'Forced air cooling of shape-memory alloy actuators for a prosthetic hand'. In: *Journal of Computing and Information Science in Engineering* 16.4 (2016), p. 041004.

[34] J. H. Lee, S. Okamoto and S. Matsubara. 'Development of multi-fingered prosthetic hand using shape memory alloy type artificial muscle'. In: *Computer Technology and Application* 3.7 (2012).

[35] F. Simone, A. York and S. Seelecke. 'Design and fabrication of a three-finger prosthetic hand using SMA muscle wires'. In: *Bioinspiration, Biomimetics, and Bioreplication 2015*. Vol. 9429. International Society for Optics and Photonics. 2015, 94290T.

[36] E. Kaplanoglu. 'Design of shape memory alloy-based and tendon-driven actuated fingers towards a hybrid anthropomorphic prosthetic hand'. In: *International Journal of Advanced Robotic Systems* 9.3 (2012), p. 77.

[37] K. J. D. Laurentis and C. Mavroidis. 'Mechanical design of a shape memory alloy actuated prosthetic hand'. In: *Technology and Health Care* 10.2 (2002), pp. 91–106.

[38] H. Taniguchi. 'Flexible artificial muscle actuator using coiled shape memory alloy wires'. In: *APCBEE procedia* 7 (2013), pp. 54–59.

[39] M. M. Company. *Miga analog driver v5 - mosfet switch*. 2019. URL: t.ly/ziSe.

[40] M. C. Hume et al. 'Functional range of motion of the joints of the hand'. In: *The Journal of hand surgery* 15.2 (1990), pp. 240–243.

[41] J. Ratzlaff. *Leaf Spring Stiffness*. 2018. URL: t.ly/ooJj (visited on 2019).

[42] H. Park, B. Lee and D. Kim. 'Development of anthropomorphic robot finger for violin fingering'. In: *ETRI Journal* 38.6 (2016), pp. 1218–1228.

[43] J. Hynek. 'Real-time fuzzy logic control of a smart material actuated, robotic prosthesis hand with grip compensation'. In: *University of the Witwatersrand* (To be submitted).

[44] N. Ma and G. Song. 'Control of shape memory alloy actuator using pulse width modulation'. In: *Smart materials and structures* 12.5 (2003), p. 712.

[45] Arduino. *Compare board specs*. 2019. URL: tinyurl.com/qe3yxtw (visited on 2019).

[46] InvenSense. 'MPU-6000 and MPU-6050 Product Specification'. In: *Revision 3.4* PS-MPU-6000A-00 (2013).

[47] N. Humfrey. *MPU6050_ tockn*. 2019. URL: tinyurl.com/y5pcbjze (visited on 2019).

[48] H. Vathsangam. *My IMU estimation experience: Complementary filter*. 2010. URL: tinyurl.com/yxr8dstv (visited on 2019).

A Matlab Code

A.1 Electro-Thermal-Mechanical Model for Step Input

```
%Step Input Analytical Solution for Two-linked Nitinol Actuated Finger

%Thermal Constants
T_inf = 25;
c = 250;
H = 30000;
T_As = 55;
T_Af = 70;
T_Ms = 50;
T_Mf = 25;
a_A=pi/(T_Af-T_As);
a_M=pi/(T_Ms-T_Mf);
h=625;
S=9.574e-5;

%Stress-Strain-Tempertature Constants
k_h=6.56e6;
k_c=7.09e6;

%Mechanical Properties
E_o=1;
Ea=72e9;
Em=41e9;
E_avg=(E_o*Em-(1-E_o)*Ea)/2;
m=4.706e-5;
p=6450;
A_wire=7.2966e-6;

%%Power Input
t=0;
V=20;                               %voltage
Fc = 490;                           %PWM Frequency
I=(cos(1*pi*Fc*t)+1);

%%Test
for Hz=50:50:450 %Sampling Frequencies

%Initial Conditions
delta_t=1/Hz;
E_o=1;
T0=25;
t=0;
```

```
time_plot=[];
l=0;
time=0;
sigma=1045618.996;
etr=0.03;
W=0;

%Matrix Setup
plotE_o = [];
angle=[];
temp_time=[];
float_temp_time=[];
l_strain=[];

%Finger Linkage Dimensions (mm)
r=12;
l_o=60;
w=48.58;
A=20;
A0=20;
ang=0;

%Bias Spring Propeties
k=24.58;
lambda=0.0195*A-0.39;

%Finger Properties
g=9.81;
m1=0.03*0.6;
m2=0.014*0.6;
A1=180-A
A_vel=(A-A0)/delta_t;
A_vel0=0;
A_acc=(A_vel-A_vel0)/delta_t;
A2=(0.0498*A^2)-(0.1427*A)+3.1472;
A20=32.299;
A2_vel=(0.0996*A*A_vel)-(0.1427*A_vel);
A2_vel0=0;
A2_acc=(0.0996*A_vel^2)+(0.0996*A_vel*A_acc)-(0.1427*A_acc);
l1=0.083;
l2=0.079;

%Uniaxial External Stress
F_s=(k*lambda)*10^-2;
F=((0.25*m1+m2)*((l1^2)*A_acc))+(0.5*m2)*((0.5*A_acc+0.5*A2_acc)...
+(l1*l2*cosd(A2)*(2*A_acc+A2_acc))-(l1*l2*sind(A2)*(2*A_vel+A2_vel)))...
+(0.5*m1+m2)*(g*l1*cosd(A))+m2*(0.5*g*l2*cosd(A+A2));
sigma=(F_s-F*0.02)/A_wire;
```

```
91
%Bang-bang controller is utilized for the path tracking
93 des=30;
for time=0:delta_t:3
95     tspan = [time:0.00001:time+delta_t];
       float_temp_time=[];
97     if A<des
           if T0>55 && T0<70
99             [t,T] = ode23s(@(t,T) (V*(cos(1*pi*Fc*t)+1)+ h*S*(25-T)...
               -(sigma*etr/p))/((m*c)+m*H*(pi*sin((pi*(T-T_As-S_term))...
101            /(T_Af-T_As))/(2*(T_Af-T_As)))), tspan, T0);
               temp_time=[temp_time; [t,T]];
103            float_temp_time=[t,T];
               len=length(float_temp_time);
105            Temp=float_temp_time(len,2);
               time_plot=[time_plot float_temp_time(len, 1)];
107            E_o=0.5*(1+cos(pi*(Temp-T_As-S_term)/15));
               Eavg=(E_o*Em+(1-E_o)*Ea)/2;
109            plotE_o = [plotE_o E_o];

111            strain=round(((278.92+k_h*(Temp-T0))/Eavg)*10^7)/10^7;
               l_strain=[l_strain l+strain*100];
113            l=l+strain*100;
               w=w+strain*100;
115            ang=round(((l_o^2)-(r^2)-(w^2))/(-2*r*w)*10^5)/10^5;
               A=round(acosd(-ang)*10^2)/10^2
117            angle=[angle A];

119            A_vel=(A-A0)/delta_t;
               A_acc=(A_vel-A_vel0)/delta_t;
121            A2=(0.0498*A^2)-(0.1427*A)+3.1472;
               A2_vel=(A2-A20)/delta_t;
123            A2_acc=(A2_vel-A2_vel0)/delta_t;

125           F=((0.25*m1+m2)*((l1^2)*A_acc))+(0.5*m2)...
              *((0.5*A_acc+0.5*A2_acc)...
127           +(l1*l2*cosd(A2)*(2*A_acc+A2_acc))...
              -(l1*l2*sind(A2)*(2*A_vel+A2_vel)))+(0.5*m1+m2)...
129           *(g*l1*cosd(A))...
              +m2*(0.5*g*l2*cosd(A+A2))
131
               lambda=0.0195*A-0.39;
133            F_s=(k*lambda)*10^-2;
               sigma=(F_s-0.01*F)/A_wire;
135
               A0=A;
137            A_vel0=A_vel;
               A20=A2;
```

```
139             A2_vel0=A2_vel;

141         else
                [t,T] = ode45(@(t,T) (V*(cos(1*pi*Fc*t)+1) + h*S*(25-T)...
143             -(sigma*etr/p))/(m*c), tspan, T0);
                temp_time=[temp_time; [t,T]];
145             float_temp_time=[t,T];
                len=length(float_temp_time);
147             Temp=float_temp_time(len,2);
                time_plot=[time_plot float_temp_time(len, 1)];
149             E_o=0.5*(1+cos(pi*(Temp-T_Mf-S_term)/25));
                Eavg=(E_o*Em+(1-E_o)*Ea)/2;
151             plotE_o = [plotE_o E_o];

153             strain=round(((278.92+k_h*(Temp-T0))/Eavg)*10^7)/10^7;
                l_strain=[l_strain l+strain*100];
155             l=l+strain*100;
                w=w+strain*100;
157             ang=round(((l_o^2)-(r^2)-(w^2))/(-2*r*w)*10^5)/10^5;
                A=round(acosd(-ang)*10^2)/10^2;
159             angle=[angle A];

161             A_vel=(A-A0)/delta_t;
                A_acc=(A_vel-A_vel0)/delta_t;
163             A2=(0.0498*A^2)-(0.1427*A)+3.1472;
                A2_vel=(A2-A20)/delta_t;
165             A2_acc=(A2_vel-A2_vel0)/delta_t;


167
               F=((0.25*m1+m2)*((l1^2)*A_acc))+(0.5*m2)...
169             *((0.5*A_acc+0.5*A2_acc)...
                 +(l1*l2*cosd(A2)*(2*A_acc+A2_acc))...
171              -(l1*l2*sind(A2)*(2*A_vel+A2_vel)))...
                 +(0.5*m1+m2)*(g*l1*cosd(A))...
173              +m2*(0.5*g*l2*cosd(A+A2))

175             lambda=0.0195*A-0.39;
                F_s=(k*lambda)*10^-2;
177             sigma=(F_s-0.01*F)/A_wire;

179             A0=A;
                A_vel0=A_vel;
181             A20=A2;
                A2_vel0=A2_vel;
183
        end
185 else
        if T0>25 && T0<50
```

```
            [t,T] = ode45(@(t,T) (h*S*(25-T)-(sigma*etr/p))...
            /((m*c)-m*H*(-pi*sin((pi*(T-T_Mf-S_term))/(T_Ms-T_Mf))...
            /(2*(T_Ms-T_Mf)))), tspan, T0);
            temp_time=[temp_time; [t,T]];
            float_temp_time=[t,T];
            len=length(float_temp_time);
            Temp=float_temp_time(len,2);
            time_plot=[time_plot float_temp_time(len, 1)];
            E_o=0.5*(1+cos(pi*(Temp-T_Mf-S_term)/25));
            Eavg=(E_o*Em+(1-E_o)*Ea)/2;
            plotE_o = [plotE_o E_o];

            strain=round(((123.17+k_c*(Temp-T0))/Eavg)*10^7)/10^7;
            l_strain=[l_strain l+strain*100];
            l=l+strain*100;
            w=w+strain*100;
            ang=round(((l_o^2)-(r^2)-(w^2))/(-2*r*w)*10^5)/10^5;
            A=round(acosd(-ang)*10^2)/10^2;
            angle=[angle A];

            A_vel=(A-A0)/delta_t;
            A_acc=(A_vel-A_vel0)/delta_t;
            A2=(0.0498*A^2)-(0.1427*A)+3.1472;
            A2_vel=(A2-A20)/delta_t;
            A2_acc=(A2_vel-A2_vel0)/delta_t;

        F=((0.25*m1+m2)*((l1^2)*A_acc))+(0.5*m2)...
        *((0.5*A_acc+0.5*A2_acc)...
        +(l1*l2*cosd(A2)*(2*A_acc+A2_acc))...
        -(l1*l2*sind(A2)*(2*A_vel+A2_vel)))...
        +(0.5*m1+m2)*(g*l1*cosd(A))...
        +m2*(0.5*g*l2*cosd(A+A2))

            lambda=0.0195*A-0.39;
            F_s=(k*lambda)*10^-2;
            sigma=(F_s-0.01*F)/A_wire;

            A0=A;
            A_vel0=A_vel;
            A20=A2;
            A2_vel0=A2_vel;

    else
            [t,T] = ode45(@(t,T) ( h*S*(25-T)-(sigma*etr/p))...
            /(m*c), tspan, T0);
            temp_time=[temp_time; [t,T]];
            float_temp_time=[t,T];
            len=length(float_temp_time);
```

```
235                 Temp=float_temp_time(len,2);
                    time_plot=[time_plot float_temp_time(len, 1)];
237                 E_o=0.5*(1+cos(pi*(Temp-T_Mf-S_term)/25));
                    Eavg=(E_o*Em+(1-E_o)*Ea)/2;
239                 plotE_o = [plotE_o E_o];

241                 strain=round(((123.17+k_c*(Temp-T0))/Eavg)*10^7)/10^7;
                    l_strain=[l_strain l+strain*100];
243                 l=l+strain*100;
                    w=w+strain*100;
245                 ang=round(((l_o^2)-(r^2)-(w^2))/(-2*r*w)*10^5)/10^5;
                    A=round(acosd(-ang)*10^2)/10^2;
247                 angle=[angle A];

249                 A_vel=(A-A0)/delta_t;
                    A_acc=(A_vel-A_vel0)/delta_t;
251                 A2=(0.0498*A^2)-(0.1427*A)+3.1472;
                    A2_vel=(A2-A20)/delta_t;
253                 A2_acc=(A2_vel-A2_vel0)/delta_t;

255                F=((0.25*m1+m2)*((l1^2)*A_acc))+(0.5*m2)...
                    *((0.5*A_acc+0.5*A2_acc)...
257                 +(l1*l2*cosd(A2)*(2*A_acc+A2_acc))...
                    -(l1*l2*sind(A2)*(2*A_vel+A2_vel)))...
259                 +(0.5*m1+m2)*(g*l1*cosd(A))...
                    +m2*(0.5*g*l2*cosd(A+A2))
261
                    lambda=0.0195*A-0.39;
263                 F_s=(k*lambda)*10^-2;
                    sigma=(F_s-0.01*F)/A_wire;
265
                    A0=A;
267                 A_vel0=A_vel;
                    A20=A2;
269                 A2_vel0=A2_vel;
            end
271     end
        leng=length(temp_time);
273     T0=temp_time(leng,2);
end
275 %The following for-loops are copies of the one above, only the desired
%finger angle is changed
277 des=50;
for time=3+delta_t:delta_t:4
279 %insert previous for-loop
end
281 des=30;
for time=4+delta_t:delta_t:5
```

```
283 %insert previous for-loop
    end
285 figure(1);
    plot(time_plot, angle, 'LineWidth',1.5);
287 hold on
    end
```

B Arduino Code

B.1 Step Signal Code

```
//Step Signal
#include <MPU6050_tockn.h>
#include <Wire.h>

MPU6050 mpu6050(Wire);
unsigned long time;

int miga = 12;
int analogPin = A3;
int val = 0;
int lim = 30;
int lim2 = 50;
int t=0;
void setup() {

pinMode(miga, OUTPUT);
Serial.begin(9600);
Wire.begin();
mpu6050.begin();
mpu6050.calcGyroOffsets(true);
Serial.println("Angle");
mpu6050.update();
delay(5000);
}

void loop() {

  mpu6050.update();
while (time/100 <300){
 while( mpu6050.getAngleX() < lim){
 digitalWrite(miga, HIGH);
   mpu6050.update();
   Serial.print(mpu6050.getAngleX());
   Serial.print(",");
   Serial.print(mpu6050.getAccX());
   Serial.print(",");
   Serial.print(mpu6050.getAccY());
   Serial.print(",");
   Serial.print(mpu6050.getAccZ());
   Serial.print(",");
   Serial.print(mpu6050.getGyroY());
   Serial.print(",");
```

```
43    Serial.print(lim);
      Serial.print(",");
45    time = millis();
      Serial.println(time/100);
47    delay(2);
}
49 while( mpu6050.getAngleX() > lim){
 digitalWrite(miga, LOW);
51     mpu6050.update();
      Serial.print(mpu6050.getAngleX());
53    Serial.print(",");
      Serial.print(mpu6050.getAccX());
55    Serial.print(",");
      Serial.print(mpu6050.getAccY());
57    Serial.print(",");
      Serial.print(mpu6050.getAccZ());
59    Serial.print(",");
      Serial.print(mpu6050.getGyroY());
61    Serial.print(",");
      Serial.print(lim);
63    Serial.print(",");
     time = millis();
65    Serial.println(time/100);
     delay(2);
67 }
 }
69 while (time/100 <400){
 while( mpu6050.getAngleX() < lim2){
71  digitalWrite(miga, HIGH);
     mpu6050.update();
73    Serial.print(mpu6050.getAngleX());
      Serial.print(",");
75    Serial.print(mpu6050.getAccX());
      Serial.print(",");
77    Serial.print(mpu6050.getAccY());
      Serial.print(",");
79    Serial.print(mpu6050.getAccZ());
      Serial.print(",");
81    Serial.print(mpu6050.getGyroY());
      Serial.print(",");
83    Serial.print(lim2);
      Serial.print(",");
85    time = millis();
      Serial.println(time/100);
87    delay(2);
}
89 while( mpu6050.getAngleX() > lim2){
 digitalWrite(miga, LOW);
```

```
    mpu6050.update();
    Serial.print(mpu6050.getAngleX());
    Serial.print(",");
    Serial.print(mpu6050.getAccX());
    Serial.print(",");
    Serial.print(mpu6050.getAccY());
    Serial.print(",");
    Serial.print(mpu6050.getAccZ());
    Serial.print(",");
    Serial.print(mpu6050.getGyroX());
    Serial.print(",");
    Serial.print(lim2);
    Serial.print(",");
    time = millis();
    Serial.println(time/100);
    delay(2);
}
  }

    while (time/100 <800){
  while( mpu6050.getAngleX() < lim){
  digitalWrite(miga, HIGH);
    mpu6050.update();
    Serial.print(mpu6050.getAngleX());
    Serial.print(",");
    Serial.print(mpu6050.getAccX());
    Serial.print(",");
    Serial.print(mpu6050.getAccY());
    Serial.print(",");
    Serial.print(mpu6050.getAccZ());
    Serial.print(",");
    Serial.print(mpu6050.getGyroY());
    Serial.print(",");
    Serial.print(lim);
    Serial.print(",");
    time = millis();
    Serial.println(time/100);
    delay(2);
}
while( mpu6050.getAngleX() > lim){
  digitalWrite(miga, LOW);
    mpu6050.update();
    Serial.print(mpu6050.getAngleX());
    Serial.print(",");
    Serial.print(mpu6050.getAccX());
    Serial.print(",");
    Serial.print(mpu6050.getAccY());
    Serial.print(",");
```

```
  Serial.print(mpu6050.getAccZ());
  Serial.print(",");
  Serial.print(mpu6050.getGyroY());
  Serial.print(",");
  Serial.print(lim);
  Serial.print(",");
  time = millis();
  Serial.println(time/100);
  delay(2);

}
 }

}
```

B.2 Ramp Signal Code

```
//Ramp Signal
#include <MPU6050_tockn.h>
#include <Wire.h>

MPU6050 mpu6050(Wire);
unsigned long time;

int miga = 12;
int analogPin = A3;
int val = 0;
int lim = 30;
int lim2 = 50;
int lim3 = 20;
int t=0;
int t1=0;
int des=0;
void setup() {
  // put your setup code here, to run once:
 pinMode(miga, OUTPUT);
  Serial.begin(9600);
   Wire.begin();
  mpu6050.begin();
  mpu6050.calcGyroOffsets(true);
  Serial.println("Angle");
  mpu6050.update();
  delay(5000);
}

```

```
void loop() {


  mpu6050.update();
time = millis();

 while (time/100 < 300){
  t1=t/5000;
  lim=(11.6*(time/100))/100+15;
    des=lim;
 while( mpu6050.getAngleX() < lim){
 digitalWrite(miga, HIGH);
   mpu6050.update();
  Serial.print(mpu6050.getAngleX());
  Serial.print(",");
  Serial.print(des);
  Serial.print(",");
  Serial.print(mpu6050.getAccX());
  Serial.print(",");
  Serial.print(mpu6050.getAccY());
  Serial.print(",");
  Serial.print(mpu6050.getAccZ());
  Serial.print(",");
  Serial.print(mpu6050.getGyroY());
  Serial.print(",");
  t=t+100;
  time = millis();
  Serial.println(time/100);
  delay(2);


}

while( mpu6050.getAngleX() > lim){
 digitalWrite(miga, LOW);
   mpu6050.update();
  Serial.print(mpu6050.getAngleX());
  Serial.print(",");
  Serial.print(des);
  Serial.print(",");
  Serial.print(mpu6050.getAccX());
  Serial.print(",");
  Serial.print(mpu6050.getAccY());
  Serial.print(",");
  Serial.print(mpu6050.getAccZ());
  Serial.print(",");
  Serial.print(mpu6050.getGyroY());
  Serial.print(",");
```

```
   t=t+100;
   time = millis();
   Serial.println(time/100);
   delay(2);

}
 }

 while( time/100 < 400){
    des=lim2;
   while( mpu6050.getAngleX() < lim2){
 digitalWrite(miga, HIGH);
    mpu6050.update();
   Serial.print(mpu6050.getAngleX());
   Serial.print(",");
   Serial.print(des);
   Serial.print(",");
   Serial.print(mpu6050.getAccX());
   Serial.print(",");
   Serial.print(mpu6050.getAccY());
   Serial.print(",");
   Serial.print(mpu6050.getAccZ());
   Serial.print(",");
   Serial.print(mpu6050.getGyroY());
   Serial.print(",");
   t=t+100;
   time = millis();
   Serial.println(time/100);
   delay(2);


}
while( mpu6050.getAngleX() > lim2){
 digitalWrite(miga, LOW);
    mpu6050.update();

   Serial.print(mpu6050.getAngleX());
   Serial.print(",");
   Serial.print(des);
   Serial.print(",");
   Serial.print(mpu6050.getAccX());
   Serial.print(",");
   Serial.print(mpu6050.getAccY());
   Serial.print(",");
   Serial.print(mpu6050.getAccZ());
   Serial.print(",");
   Serial.print(mpu6050.getGyroY());
   Serial.print(",");
```

```
  t=t+100;
  time = millis();
  Serial.println(time/100);
  delay(2);

}
 }
while ( time/100 < 600){
  t1=t/5000;
  lim3=50-(0.116*((time/100)-399));
   des=lim3;

 while( mpu6050.getAngleX() < lim3){
 digitalWrite(miga, HIGH);
   mpu6050.update();

  Serial.print(mpu6050.getAngleX());
  Serial.print(",");
  Serial.print(des);
  Serial.print(",");
  Serial.print(mpu6050.getAccX());
  Serial.print(",");
  Serial.print(mpu6050.getAccY());
  Serial.print(",");
  Serial.print(mpu6050.getAccZ());
  Serial.print(",");
   Serial.print(mpu6050.getGyroY());
  Serial.print(",");
  t=t+100;
  time = millis();
  Serial.println(time/100);
  delay(2);


}
while( mpu6050.getAngleX() > lim3){
 digitalWrite(miga, LOW);
   mpu6050.update();

  Serial.print(mpu6050.getAngleX());
  Serial.print(",");
  Serial.print(des);
  Serial.print(",");
  Serial.print(mpu6050.getAccX());
  Serial.print(",");
  Serial.print(mpu6050.getAccY());
  Serial.print(",");
  Serial.print(mpu6050.getAccZ());
```

```
  Serial.print(",");
  Serial.print(mpu6050.getGyroY());
  Serial.print(",");
  t=t+100;
  time = millis();
  Serial.println(time/100);
  delay(2);

}
 }

}
```

B.3 Finger Strength Code

```
  int thumb = 13;
  int index = 12;
  int middle = 11;
  int ring = 10;
  int little = 9;

void setup() {

  pinMode(thumb, OUTPUT);
  pinMode(index, OUTPUT);
  pinMode(middle, OUTPUT);
  pinMode(ring, OUTPUT);
  pinMode(little, OUTPUT);

}

void loop() {
// Comment out the fingers that do not activate
  //thumb finger
//////////////////////////////////////////////////////////////////
  digitalWrite(13, HIGH);
  delayMicroseconds(500); // Approximately 50% duty cycle @ 1KHz
  digitalWrite(13, LOW);
  delayMicroseconds(1000 - 500);
//////////////////////////////////////////////////////////////////
  //index finger
//////////////////////////////////////////////////////////////////
   digitalWrite(12, HIGH);
  delayMicroseconds(500); // Approximately 50% duty cycle @ 1KHz
  digitalWrite(12, LOW);
```

```
  delayMicroseconds(1000 - 500);
////////////////////////////////////////////////////////////////
  //middle finger
////////////////////////////////////////////////////////////////
   digitalWrite(11, HIGH);
  delayMicroseconds(500); // Approximately 50% duty cycle @ 1KHz
  digitalWrite(11, LOW);
  delayMicroseconds(1000 - 500);
////////////////////////////////////////////////////////////////
  //ring finger
////////////////////////////////////////////////////////////////
   digitalWrite(10, HIGH);
  delayMicroseconds(500); // Approximately 50% duty cycle @ 1KHz
  digitalWrite(10, LOW);
  delayMicroseconds(1000 - 500);
////////////////////////////////////////////////////////////////
   //little finger
////////////////////////////////////////////////////////////////
   digitalWrite(9, HIGH);
  delayMicroseconds(500); // Approximately 50% duty cycle @ 1KHz
  digitalWrite(9, LOW);
  delayMicroseconds(1000 - 500);
}
```

B.4 Hand PWM Control Code

```
int thumb = 13;
int index = 12;
int middle = 11;
int ring = 10;
int little = 9;

int FSR_thumb = A1;
int FSR_index = A5;
int FSR_middle = A4;
int FSR_ring = A3;
int FSR_little = A2;

int FSR_lim = 100;

void setup() {

 pinMode ( thumb , OUTPUT) ;
 pinMode ( index , OUTPUT) ;
 pinMode ( middle , OUTPUT) ;
```

```
 pinMode ( ring , OUTPUT) ;
 pinMode ( little , OUTPUT) ;

}

void loop() {

//Comment out the fingers that are not meant to be activated.
int thumb_run = fingeractivate(thumb, FSR_lim, FSR_thumb);
int index_run = fingeractivate(index, FSR_lim, FSR_index);
int middle_run = fingeractivate(middle, FSR_lim, FSR_middle);
int ring_run = fingeractivate(ring, FSR_lim, FSR_ring);
int little_run = fingeractivate(little, FSR_lim, FSR_little);

}

//PWM function for finger
int fingeractivate(int finger, int lim, int FSR){

 int val=analogRead(FSR);
 while (val<lim){
 val=analogRead(FSR);
 digitalWrite(finger, HIGH);
 delayMicroseconds(500); //Approximately 50% duty cycle at 1kHz
 digitalWrite(finger, LOW);
 delayMicroseconds(1000-500);
 }
 while (val>lim){
 val=analogRead(FSR);
 digitalWrite(finger, LOW);
 }
}
```

C Detailed Analytical Derivations

C.1 Kinematic Finger Model

The Lagrangian method is used to derive the dynamic modelling of the system. The finger mechanism can be simplified into a linkage system with 1 degree of freedom, since θ_2 is dependent on θ_1. The finger links are simplified into two rods of lengths l_1 and l_2 which are joined together by a pin, as shown in Figure C.1. An actuation torque, τ_1, generated by a nitinol actuator acts on link 1 in an anticlockwise direction.

The angular displacement θ_2 is dependent on the finger angle defined as θ_1 due to Link 2. An equation that expresses θ_2 in terms of θ_1 was derived using geometric models in Autodesk Inventor.

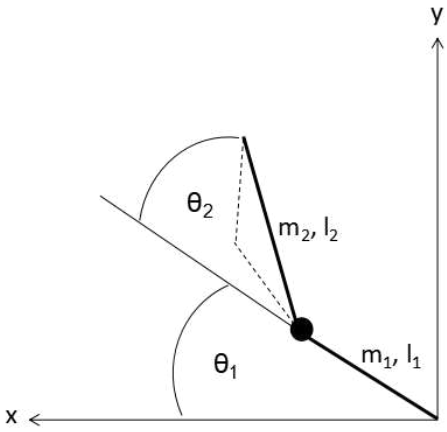


Figure C.1: Simplified Link Diagram of Finger Mechanism

$$\theta_2 = 0.0498\theta_1^2 - 0.1427\theta_1 + 3.1472 \tag{C.1}$$

Therefore:

$$\dot{\theta}_2 = 0.0996\theta_1\dot{\theta}_1 - 0.1427\dot{\theta}_1 \tag{C.2}$$

$$\ddot{\theta}_2 = 0.0996\dot{\theta}_1^2 + 0.0996\theta_1\ddot{\theta}_1 - 0.1427\ddot{\theta}_1 \tag{C.3}$$

By using the trigonometric method:

$$x_1 = \frac{1}{2}l_1\cos\theta_1 \tag{C.4}$$

$$y_1 = \frac{1}{2}l_1\sin\theta_1 \tag{C.5}$$

$$x_2 = l_1 \cos\theta_1 + \frac{1}{2} l_2 \cos(\theta_1 + \theta_2) \tag{C.6}$$

$$y_2 = l_1 \sin\theta_1 + \frac{1}{2} l_2 \sin(\theta_1 + \theta_2) \tag{C.7}$$

The linear velocity of mass center of the finger was found using Euler Lagrange formula:

$$\dot{x_1} = -\frac{1}{2} l_1 \sin\theta_1 \dot{\theta_1} \tag{C.8}$$

$$\dot{y_1} = \frac{1}{2} l_1 \cos\theta_1 \dot{\theta_1} \tag{C.9}$$

$$\dot{x_2} = -l_1 \sin\theta_1 \dot{\theta_1} - \frac{1}{2} l_2 \sin(\theta_1 + \theta_2)(\dot{\theta_1} + \dot{\theta_2}) \tag{C.10}$$

$$\dot{y_2} = l_1 \cos\theta_1 \dot{\theta_1} + \frac{1}{2} l_2 \cos(\theta_1 + \theta_2)(\dot{\theta_1} + \dot{\theta_2}) \tag{C.11}$$

The equations for the linear velocities are the square and sum of the Equations C.8, C.9, C.10 and C.11 to find v_1 and v_2:

$$v^2 = \dot{x}^2 + \dot{y}^2 \tag{C.12}$$

$$v_1^2 = \dot{x}_1^2 + \dot{y}_1^2 \tag{C.13}$$

$$v_1^2 = (\frac{1}{2} l_1 \cos\theta_1 \dot{\theta_1})^2 + (-\frac{1}{2} l_1 \sin\theta_1 \dot{\theta_1})^2 \tag{C.14}$$

$$v_1^2 = \frac{1}{4} l_1^2 \dot{\theta_1}^2 \tag{C.15}$$

$$v_2^2 = \dot{x}_2^2 + \dot{y}_2^2 \tag{C.16}$$

$$\begin{aligned} v_2^2 = \dot{(} l_1 \cos\theta_1 \dot{\theta_1} + \frac{1}{2} l_2 \cos(\theta_1 + \theta_2)(\dot{\theta_1} + \dot{\theta_2}))^2 \\ +(-l_1 \sin\theta_1 \dot{\theta_1} - \frac{1}{2} l_2 \sin(\theta_1 + \theta_2)(\dot{\theta_1} + \dot{\theta_2}))^2 \end{aligned} \tag{C.17}$$

$$v_2^2 = l_1^2 \dot{\theta_1}^2 + \frac{1}{4}(\dot{\theta_1^2} + 2\dot{\theta_1}\dot{\theta_2} + \dot{\theta_2^2}) + l_1 l_2 cos(\theta_2)(\dot{\theta_1^2} + \dot{\theta_1}\dot{\theta_2}) \tag{C.18}$$

The kinetic energy for the system is:

$$T = \frac{1}{2} m_1 v_1^2 + \frac{1}{2} m_2 v_2^2 \tag{C.19}$$

Substituting Equation C.15 and Equation C.18 into Equation C.19:

$$T = \frac{1}{2} m_1 (\frac{1}{4} l_1^2 \dot{\theta_1}^2) + \frac{1}{2} m_2 (l_1^2 \dot{\theta_1}^2 + \frac{1}{4}(\dot{\theta_1^2} + 2\dot{\theta_1}\dot{\theta_2} + \dot{\theta_2^2}) + l_1 l_2 cos(\theta_2)(\dot{\theta_1^2} + \dot{\theta_1}\dot{\theta_2})) \tag{C.20}$$

$$T = \frac{1}{2} (\frac{1}{4} m_1 + m_2)(l_1^2 \dot{\theta_1}^2) + \frac{1}{2} m_2 (\frac{1}{4}(\dot{\theta_1^2} + 2\dot{\theta_1}\dot{\theta_2} + \dot{\theta_2^2}) + l_1 l_2 cos(\theta_2)(\dot{\theta_1^2} + \dot{\theta_1}\dot{\theta_2})) \tag{C.21}$$

The potential energy for the system is:

$$V = m_1 g y_1 + m_2 g y_2 \tag{C.22}$$

Substituting Equation C.4 and Equation C.6 into Equation C.22:

$$V = m_1 g(\frac{1}{2} l_1 \sin\theta_1) + m_2 g(l_1 \sin\theta_1 + \frac{1}{2} l_2 \sin(\theta_1 + \theta_2)) \tag{C.23}$$

$$V = (\frac{1}{2} m_1 + m_2)(g l_1 \sin\theta_1) + m_2(\frac{1}{2} g l_2 \sin(\theta_1 + \theta_2)) \tag{C.24}$$

The lagrangian is calculated as:

$$L = T - V \tag{C.25}$$

Therefore:

$$\begin{aligned} L = \frac{1}{2}(\frac{1}{4} m_1 + m_2)(l_1^2 \dot{\theta_1}^2) + \frac{1}{2} m_2(\frac{1}{4}(\dot{\theta}_1^2 + 2\dot{\theta}_1\dot{\theta}_2 + \dot{\theta}_2^2) + l_1 l_2 cos(\theta_2)(\dot{\theta}_1^2 + \dot{\theta}_1\dot{\theta}_2)) \\ -(\frac{1}{2} m_1 + m_2)(g l_1 \sin\theta_1) - m_2(\frac{1}{2} g l_2 \sin(\theta_1 + \theta_2)) \end{aligned} \tag{C.26}$$

The equations of motion are derived from the lagrangian as follows:

$$\frac{d}{dt}(\frac{\partial L}{\partial \dot{\theta}}) - \frac{\partial L}{\partial \theta} = \tau \tag{C.27}$$

For θ_1,

$$\frac{d}{dt}(\frac{\partial L}{\partial \dot{\theta}_1}) - \frac{\partial L}{\partial \theta_1} = \tau_1 \tag{C.28}$$

$$\frac{\partial L}{\partial \theta_1} = -(\frac{1}{2} m_1 + m_2)(g l_1 \cos(\theta_1)) - m_2(\frac{1}{2} g l_2 \cos(\theta_1 + \theta_2)) \tag{C.29}$$

$$\frac{\partial L}{\partial \dot{\theta}_1} = (\frac{1}{4} m_1 + m_2)(l_1^2 \dot{\theta}) + \frac{1}{2} m_2 \left[\frac{1}{4}(2\dot{\theta}_1 + 2\dot{\theta}_2) + l_1 l_2 \cos(\theta_2)(2\dot{\theta}_1 + \dot{\theta}_2)\right] \tag{C.30}$$

$$\frac{d}{dt}(\frac{\partial L}{\partial \dot{\theta}_1}) = (\frac{1}{4} m_1 + m_2)(l_1^2 \ddot{\theta}) + \frac{1}{2} m_2 \left[\frac{1}{4}(2\ddot{\theta}_1 + 2\ddot{\theta}_2) + l_1 l_2 \cos(\theta_2)(2\ddot{\theta}_1 + \ddot{\theta}_2) - l_1 l_2 \sin(\theta_2)(2\dot{\theta}_1 + \dot{\theta}_2)\right] \tag{C.31}$$

Therefore:

$$\begin{aligned} (\frac{1}{4} m_1 + m_2)(l_1^2 \ddot{\theta}) + \frac{1}{2} m_2 \left[\frac{1}{4}(2\ddot{\theta}_1 + 2\ddot{\theta}_2) + l_1 l_2 \cos(\theta_2)(2\ddot{\theta}_1 + \ddot{\theta}_2) - l_1 l_2 \sin(\theta_2)(2\dot{\theta}_1 + \dot{\theta}_2)\right] \\ +(\frac{1}{2} m_1 + m_2)(g l_1 \cos(\theta_1)) + m_2(\frac{1}{2} g l_2 \cos(\theta_1 + \theta_2)) = \tau_1 \end{aligned} \tag{C.32}$$

For θ_2:

$$\frac{d}{dt}(\frac{\partial L}{\partial \dot{\theta}_2}) - \frac{\partial L}{\partial \theta_2} = \tau_2 \tag{C.33}$$

$$\frac{\partial L}{\partial \theta_2} = -\frac{1}{2} m_2 l_1 l_2 \sin(\theta_2)(\dot{\theta}_1^2 + \dot{\theta}_1\dot{\theta}_2) - \frac{1}{2} m_2 g l_2 \cos(\theta_1 + \theta_2) \tag{C.34}$$

$$\frac{\partial L}{\partial \dot{\theta}_2} = \frac{1}{2} m_2 \left[\frac{1}{4}(2\dot{\theta}_1 + 2\dot{\theta}_2) + l_1 l_2 \cos(\theta_2)\dot{\theta}_1\right] \tag{C.35}$$

$$\frac{d}{dt}(\frac{\partial L}{\partial \dot{\theta}_2}) = \frac{1}{2} m_2 \left[\frac{1}{4}(2\ddot{\theta}_1 + 2\ddot{\theta}_2) + l_1 l_2 \cos(\theta_2)\ddot{\theta}_1 - l_1 l_2 \sin(\theta_2)\dot{\theta}_1\right] \tag{C.36}$$

Therefore:

$$\begin{aligned} \frac{1}{2} m_2 \left[\frac{1}{4}(2\ddot{\theta}_1 + 2\ddot{\theta}_2) + l_1 l_2 \cos(\theta_2)\ddot{\theta}_1 - l_1 l_2 \sin(\theta_2)\dot{\theta}_1\right] + \frac{1}{2} m_2 l_1 l_2 \sin(\theta_2)(\dot{\theta}_1^2 + \dot{\theta}_1\dot{\theta}_2) \\ +\frac{1}{2} m_2 g l_2 \cos(\theta_1 + \theta_2) = \tau_2 \end{aligned} \tag{C.37}$$

C.2 MPU6050 Sensor Uncertainty Analysis

The MPU6050 is a 3-axis gyroscope and accelerometer used to measure the finger angle during finger positioning testing. The finger angle is calculated using Equation C.38, where α typically equals 0.02 for the MPU6050 sensor [48]:

$$filtered_angle = \theta_{finger} = (\alpha \times accelerometer_signal) + ((1-\alpha) \times gyroscope_signal) \tag{C.38}$$

The equation combines the accelerometer and gyroscope readings to formulate the finger angle. The accelerometer signal is made up of a_x, a_y and a_z readings as follows:

$$accelerometer_signal = arctan\left(\frac{a_x}{\sqrt{a_y^2 + a_z^2}}\right) \tag{C.39}$$

The gyroscope signal is calculated using Equation C.40:

$$gyroscope_signal = (gyro_reading - gyro_offset)(gyro_scale)(sampling_time) \tag{C.40}$$

Where the standard sensitivity is 131 and gyro scale is 0.02 by default for the MPU6050 sensor. The sampling time is 50 ms [46]. Therefore the equation becomes:

$$gyroscope_signal = (G - gyro_offset)(0.02)(0.05) \tag{C.41}$$

The uncertainty of the accelerometor and gyroscopic readings are tabulated in Table C.1.

Table C.1: MPU6050 Sensor Uncertainties [46]

Parameter	Uncertainty Tolerance
Gyroscope Signal σ_G	0.05
X Acceleration σ_{ax}	0.03
Y Acceleration σ_{ay}	0.03
Z Acceleration σ_{az}	0.03

The uncertainty analysis is as follows:

$$\sigma_\theta = f(\sigma_{ax}, \sigma_{ay}, \sigma_{az}, \sigma_G) \tag{C.42}$$

$$\sigma_\theta = \sqrt{\left(\frac{\delta\theta_{finger}}{\delta a_x}\sigma_{ax}\right)^2 + \left(\frac{\delta\theta_{finger}}{\delta a_y}\sigma_{ay}\right)^2 + \left(\frac{\delta\theta_{finger}}{\delta a_z}\sigma_{az}\right)^2 + \left(\frac{\delta\theta_{finger}}{\delta G}\sigma_G\right)^2} \tag{C.43}$$

Where,

$$\frac{\delta\theta_{finger}}{\delta a_y}\sigma_{ay} = \frac{0.0006 a_y a_x}{(a_y^2 + a_z^2)^{3/2}\left(\frac{a_x^2}{a_y^2+a_z^2} + 1\right)} \tag{C.44}$$

$$\frac{\delta\theta_{finger}}{\delta a_z}\sigma_{az} = \frac{0.0006 a_y a_z}{(a_x^2 + a_z^2)^{3/2}\left(\frac{a_y^2}{a_x^2+a_z^2} + 1\right)} \tag{C.45}$$

$$\frac{\delta\theta_{finger}}{\delta a_x}\sigma_{ax} = \frac{0.0006}{(a_y^2 + a_z^2)\left(\frac{a_x^2}{(a_y^2+a_z^2)^2} + 1\right)} \tag{C.46}$$

$$\frac{\delta\theta_{finger}}{\delta G}\sigma_G = (0.001)(0.049) \tag{C.47}$$

D Prosthetic Hand Circuit Connections

Table D.1: Prosthetic Hand Circuit Connections

	Connection Path →				
Component	**Actuator**	**MOSFET**	**Voltage Sensor**	**Arduino UNO**	**9V DC Battery**
nitinol Actuator 1	ESW→	SW→Gate		→Pin 12	
	Vin→	Vout→Vin			→ + terminal
	GND→	GND→GND			→ - terminal
nitinol Actuator 2	ESW→	SW→Gate		→Pin 11	
	Vin→	Vout→Vin			→ + terminal
	GND→	GND→GND			→ - terminal
nitinol Actuator 3	ESW→	SW→Gate		→Pin 10	
	Vin→	Vout→Vin			→ + terminal
	GND→	GND→GND			→ - terminal
nitinol Actuator 4	ESW→	SW→Gate		→Pin 9	
	Vin→	Vout→Vin			→ + terminal
	GND→	GND→GND			→ - terminal
nitinol Actuator 5	ESW→	SW→Gate		→Pin 13	
	Vin→	Vout→Vin			→ + terminal
	GND→	GND→GND			→ - terminal
Finger Sensor Pad 1			S →	A5	
			+ →	5V	
			- →	GND	
Finger Sensor Pad 2			S →	A4	
			+ →	5V	
			- →	GND	
Finger Sensor Pad 3			S →	A3	
			+ →	5V	
			- →	GND	
Finger Sensor Pad 4			S →	A2	
			+ →	5V	
			- →	GND	
Finger Sensor Pad 5			S →	A1	
			+ →	5V	
			- →	GND	